AN ABSTRACT OF THE THESIS OF

Georg Weidlich for the degree of Master of Science in

Physics presented on October 27, 1989.

Title: Structural Properties of Indium Doped $YBa_2Cu_3O_{7-x}$ High T_c Superconductors

Abstract approved: _____
John A. Gardner

$YBa_2Cu_3O_{7-x}$ was doped with In by a stoichiometrically exact substitution of Y by In, doping levels ranging from 0% to 20%. Room temperature X-ray diffraction measurements, Perturbed Angular Correlation spectroscopy using ^{111}Cd as nuclear tracer at a variety of temperatures ranging from room temperature to 950°C and magnetic flux exclusion measurements were performed on samples with different In concentrations.

X-ray spectroscopy, as the least sensitive, global probe measurement, was used to characterize major and minor phases in the bulk and to investigate the dependence of Bragg spacings and structure factors at doping sites on the doping level. Intensities of Bragg peaks were integrated and normalized by appropriate methods. All phases in the bulk were identified. The major phase was orthorhombic $YBa_2Cu_3O_{7-x}$, secondary phases were identified to be $BaCuO_2$, CuO and Y_2BaCuO_5 in concentrations between 2 and 3 at% of the sample, independent of the doping level of In. Furthermore, the recently discovered compound $InBa_2Cu_3O_x$ was detected at In concentrations above the solubility limit. A linear, positive intensity change for the Bragg peak with Miller indices 003 of the $YBa_2Cu_3O_{7-x}$ up to 3.0% and for the strongest peak of the $InBa_2Cu_3O_x$ spetcrum above 3.0% determined the solubility limit of In in the bulk to be 3.0%.

A computer simulation was used to calculate X-ray diffraction spectra, assuming a unique and total substitution of the In atoms either at the Y, the Ba, the Cu(1) or the Cu(2) site. The simulation used a point ion model and simply replaced the corresponding site with In atoms in the different concentrations. Integrated, normalized intensities of the Bragg peaks of the simulation were compared with experimental results.

PAC spectroscopy as a local probe measurement is very sensitive to distortions of the electric field gradient at the tracer site. PAC spectra for samples which are not In-saturated, show a clear spectrum with three major peaks at 55, 100 and 155 Mrad/sec. This indicates a substitution of the radio-active tracer at a unique site in the lattice and corresponds to preceeding measurements. Saturated samples with In concentrations above 3.0% display a superposition of the regular spectrum with a spectrum generated probably by In substitution at sites in secondary phases.

Magnetic flux exclusion measurements show a critical temperature of 92.7°C, indicating a high sample quality. A rather small change of this measure for saturated samples was found and supports the hypothesis of In substitution at the Y site along with PAC and X-ray spectroscopy results.

Structural Properties of Indium Doped $YBa_2Cu_3O_{7-x}$ High T_c Superconductors

by

Georg A. Weidlich

A THESIS

submitted to

Oregon State University

in partial fullfillment of
the requirements for the
degree of

Master of Science

Completed October 27, 1989

Commencement June 1990

APPROVED:

Redacted for Privacy

Professor of physics in charge of major

Redacted for Privacy

Chairman of the Department of Physics

Redacted for Privacy

Dean of Graduate School

Date thesis is presented October 27, 1989

Typed by Georg Weidlich for Georg Weidlich

Acknowledgement

The completion of this work means to me one of the greatest and most challenging accomplishments in my life. However, it was only possible with the academic, financial and emotional support of several valuable persons to whom I would like to express my deepest gratefulness at this point.

Without the steady and reliable guidance, counsel and support of my thesis advisor, Dr. John A. Gardner, this work would have been practically impossible. Therefore, I would like to express my thankfulness first of all to him. His constant patience and confidence encouraged me more than once to continue the work with motivation in difficult situations. With his receptivity, understanding and help in academic matters he enabled me to accomplish my work. I wish him an early recovery from his ophthalmic illness.

Furthermore, special thanks are due to Dr. James A. Sommers for inspiring discussions about chemical aspects of the work and providing me with most of the samples used during the work.

Many thanks also to Dr. Shaw-Shya Lin Kao and Dr. Han Tzong Su who served as a valuable source of information concerning a variety of laboratory specific matters, to Dr. Robert Smith and Ms. Kathy Schaffers from the Chemistry Department of OSU for their assistance in performing the X-ray diffraction measurements, to Dr. Douglas Keszler for knowledgeable advise in crystallographic matters, to Dr. Douglas Finnemore from Ames Laboratories in Ames, Iowa, for performing the magnetic flux exclusion measurements and to Mr. Tyson Storch for his review of my thesis during an early draft stage and his corrections of many grammatical mistakes.

For her helpful cooperation with PAC measurements and review of my thesis, thanks to Mrs. Ruiping Wang.

For their review of my thesis and valuable comments on it I thank Dr. Jeffrey R. Barnes, Dr. Janet Tate, Dr. Douglas Keszler, Dr. William Evenson, and Mrs. Ruiping Wang.

Financial support from the Office of International Education of OSU via the Baden-Württemberg-Oregon Exchange program during the first year of this work, from the National Science foundation and from my family in West Germany are thankfully acknowledged.

This work is dedicated to my parents. They were the closest and most important persons in my life and helped me to accomplish this work.

Table of Contents

Table of Contents

Table of Contents

Table of Contents

List of Figures

List of Figures

List of Figures

List of Tables

STRUCTURAL PROPERTIES OF INDIUM DOPED $YBa_2Cu_3O_{7-X}$ HIGH T_C SUPERCONDUCTORS

1. INTRODUCTION

1.1 OUTLINE OF THESIS RESEARCH

The subject of the research for this thesis was the superconducting material $YBa_2Cu_3O_{7-x}$ which was investigated by X-ray diffraction, Perturbed Angular Correlation spectroscopy (PAC) and magnetic flux exclusion measurements by Meissner Effect. PAC is a local probe method that uses radioactive tracers. The tracer ^{111}In is introduced into the lattice of the superconducting material $YBa_2Cu_3O_{7-x}$ (1-2-3 compound).

Of special interest are the substitutional site location and the solubility limit of the nuclear tracer. In order to determine these, the superconducting material was doped with non-radioactive In.

Samples with doping levels of In in the concentrations of 0, 1, 2, 4, 5, 6, 8, 10, 12, 15 and 20 at% of Y were made by the nitrate evaporation method from stoichiometrically exact mixtures of nitrates with the cation ratio 1 (Y+In) : 2 Ba : 3 Cu. The stoichiometrical removal of Y for additional In was done initially because it was believed that In would substitute for Y as had been reported by other investigators.

X-ray diffraction measurements from the superconductor in bulk form were performed, applying the Debye-Scherrer method. All generated phases were identified and the Bragg spacings d and integrated intensities of Bragg peaks generated at planes containing In were investigated from the major 1-2-3 phase and the secondary phases.

A computer simulation using a point ion model was used to determine the structure factors and its intensities associated with a complete set of Bragg peaks. The computer simulations were compared with experimental results in an attempt to determine the location of the In substitution.

PAC measurements of the superconductor were made for samples with doping levels 0%, 1%, 2% and 5%. Magnetic susceptibility measurements were undertaken to obtain information about the sample quality and the solubility limit.

1.2 SUMMARY OF RESULTS

By X-ray spectrometry, PAC spectroscopy as well as magnetic susceptibility measurements, it was established that $YBa_2Cu_3O_{7-x}$ with $x \approx 0.05$ is the major phase in the bulk sample. Four secondary phases were identified to be $BaCuO_2$, CuO, Y_2BaCuO_5 and $InBa_2Cu_3O_x$. The latter compound occured only for samples containing concentrations of In above the solubility limit and featured a linear increase of the Bragg intensities in In saturated samples.

The critical temperature was $T_c = 92.7$ K for pure $YBa_2Cu_3O_{7-x}$, measured by magnetic flux exclusion. The onset of superconductivity is sharp, and the flux expulsion strong. This indicates a high sample quality.

X-ray diffractographs showed a minor shift of the Bragg spacing measured by diffraction angle 2θ. The shifts of these peaks, however, were too small to be measured within experimental uncertainty. Investigations of the integrated, normalized intensities of the 003 peak in the 1-2-3 spectrum and of the strongest peak in the $InBa_2Cu_3O_x$ spectrum showed a linear shift with In concentration in the sample.

The intensity of 003 increased linearly with respect to the In concentration up to 3.0%. For higher concentration the lattice was In-saturated and the intensity of 003 remained constant .

The $InBa_2Cu_3O_x$ Bragg peaks were undetectable for concentrations up to 3.0% because all In could be dissolved in the major phase of the bulk. For In concentrations above the solubility limit of 3.0%, the intensity for the strongest peak in this spectrum increased linearly with respect to the added In.

A computer simulation of this experiment showed an increase between the samples containing 0 % and 3 % In of 0.9 % in intensity for a substitution at the Y site. The experimental intensity change was 30.1 % for the same samples. The difference of a factor of 33 is not well understood. It may be caused by a significant morphology change occuring in samples with higher In concentration.

Several strong arguments give indication for substitution at the Y site:

- a constant but small amount of $BaCuO_2$, CuO and Y_2BaCuO_5 indicate that all In either dissolves in the 1-2-3 phase or precipitates out in the $InBa_2Cu_3O_x$ phase (considering the sample preparation)
- the only minor change (1.5%) of the critical temperature in the magnetic flux exclusion measurements suggests a substitution site other than the Cu(1) site which is involved directly in superconductivity
- only negligible amounts of substitution sites other than the major 1-2-3 site in the PAC measurements for samples with doping levels below the solubility limit.

1.3 INTRODUCTION TO HIGH TEMPERATURE SUPERCONDUCTORS $YBa_2Cu_3O_{7-x}$

Nb3Ge with a critical temperature of 23.2 K was discovered in 1973.[1] Although strong efforts have been made, the attempts to find compounds showing higher critical temperatures remained unsuccessful for more than one decade.

1.3.1 HISTORICAL OUTLINE

A new generation of superconductors was introduced by Georg Bednorz and Alexander Müller working at the IBM Laboratories in Rüschlikon near Zürich in Switzerland. Müller regarded the possibility, that the ground state of systems with very strong electron-phonon interactions may undergo a phase transition between superconducting and bipolaronic-insulating states.

Thus, Müller and his collaborator Bednorz started studying oxides that were likely to have strong electron-phonon interactions. In April 1986 they discovered Superconductivity at 35 K in the La-Ba-Cu-O system with a K_2NiF_4-type tetragonal structure.[2] They focused the center of interest among the Solid State Physics Community onto a group of cuprate compounds, called high T_c Superconductors.

Before the end of 1986 three groups at the University of Tokyo, the AT&T Bell Laboratories and the Institute of Physics in Beijing reported that by substitution of Sr for Ba in the system found by Bednorz and Müller, T_c could be raised to 40 K. Chu et al. found a transition temperature of 52 K in the La-Ba-Cu-O system under a pressure of 12 kbar.[3]

In February 1987 Wu et al. from the University of Alabama and Chu et al. from the University of Houston announced that they had seen the onset of superconductivity at 93 K in a Y-Ba-Cu-O system.[4] The Carnegie Institution's Geophysical Laboratory reported that superconductivity can be observed above 90 K for several cuprates with the formula $RBa_2Cu_3O_{9-x}$, where R stands for a rare earth ion. The following rare earth ions could be substituted successfully: scandium, lanthanum, neodymium, samarium, europium, gadolinium, dysprosium, holmium, erbium, ytterbium and lutetium.

The structure of $YBa_2Cu_3O_{7-x}$ was determined by several groups to be orthorhombic. This oxygen-deficient perovskite was the major subject during the research for this work and several physical properties will be discussed explicitly.

Although numerous attempts to find compounds with higher transition temperatures to superconductivity have been undertaken, most of them could not be reproduced and none of these compounds were single-phased.

Tarascon et al., however, found a transition to superconductivity at 110 K for the Bi-Sr-Ca-Cu-O system.[5] A T_c of 125 K was reported and confirmed in Bi-Tl-systems of the same type. Higher T_c were reported often but none were confirmed.[6]

Recent studies of High T_c systems focus mainly on the Y-Ba-Cu-O system, because it can be synthesized easily to a single-phased compound and reproducibility of the sample preparation is not a major problem.

1.3.2 CRYSTAL STRUCTURE

The two new classes of High T_c Superconductors, i.e. the La-Ba-Cu-O and the Y-Ba-Cu-O system (called 1-2-3), can both structurally be derived from the Mineral Perovskite $BaTiO_3$.[7]

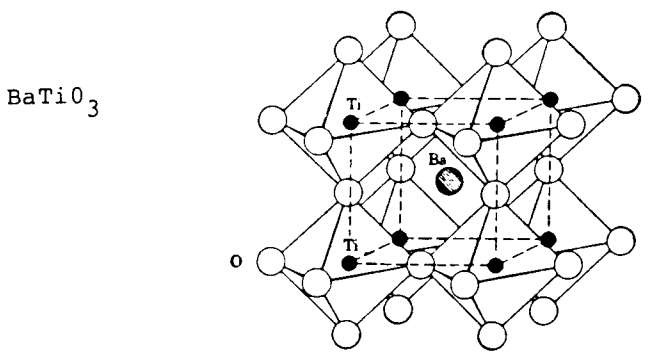

Fig 1.1 Lattice structure of $BaTiO_3$ [Ref. 8]

The figure shows the well-known structure of $BaTiO_3$. Significant are the CuO_6-octahedrals with their centers at the Ti atoms. The Ba atom is located in the center of the cube generated by Ti atoms.

In the La-Ba-Cu-O system the CuO_6-octahedrals are two-dimensional planar connected, because the following layer of CuO_6-octahedrals is shifted by (a/2,a/2) in the (a,b) plane. This tetragonal High T_c phase changes to orthorhombic structure at lower temperatures and the CuO_6-octahedrals are tilted around the b-axis. Such structural

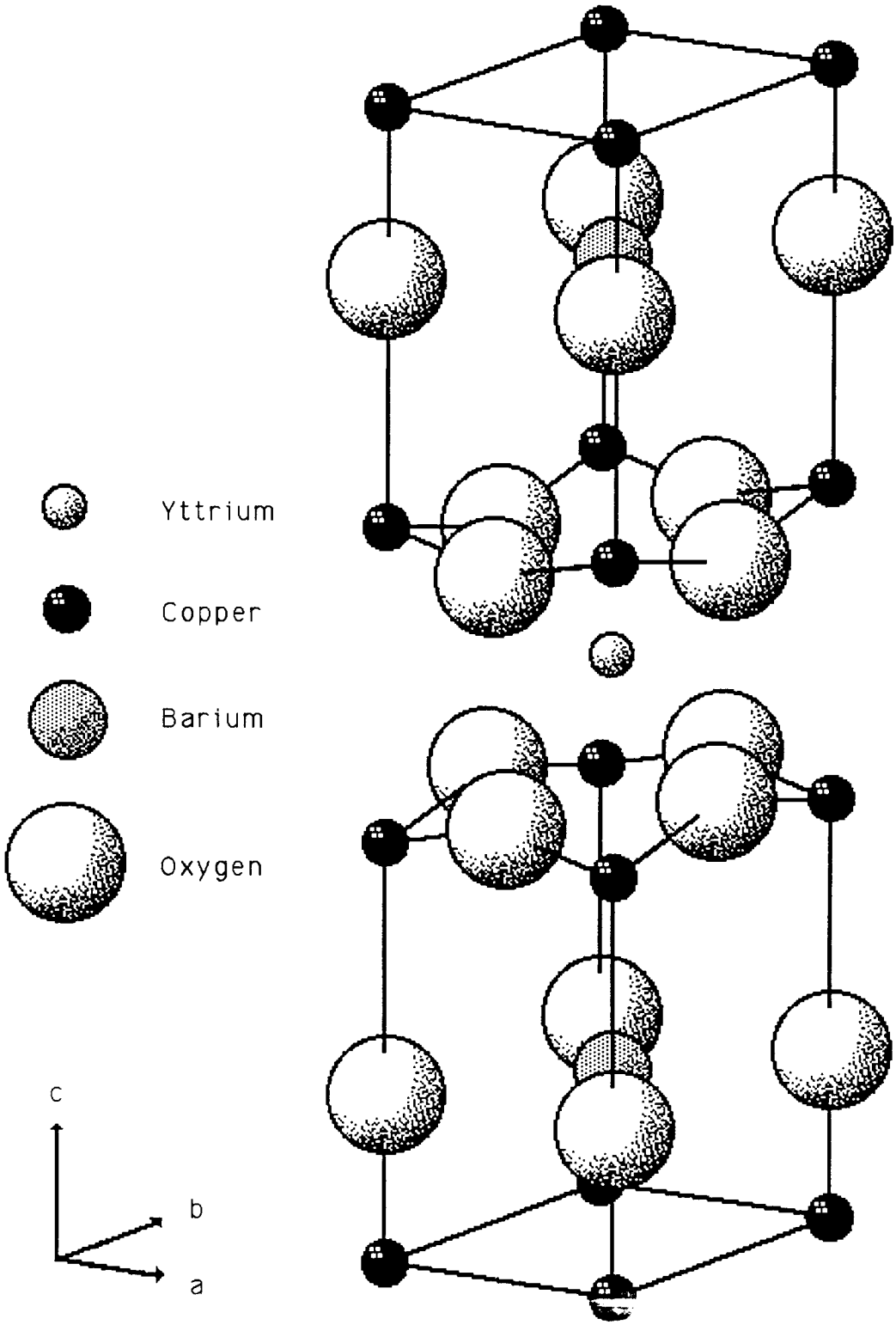

Fig. 1.2 Unit cell of tetragonal $YBa_2Cu_3O_6$

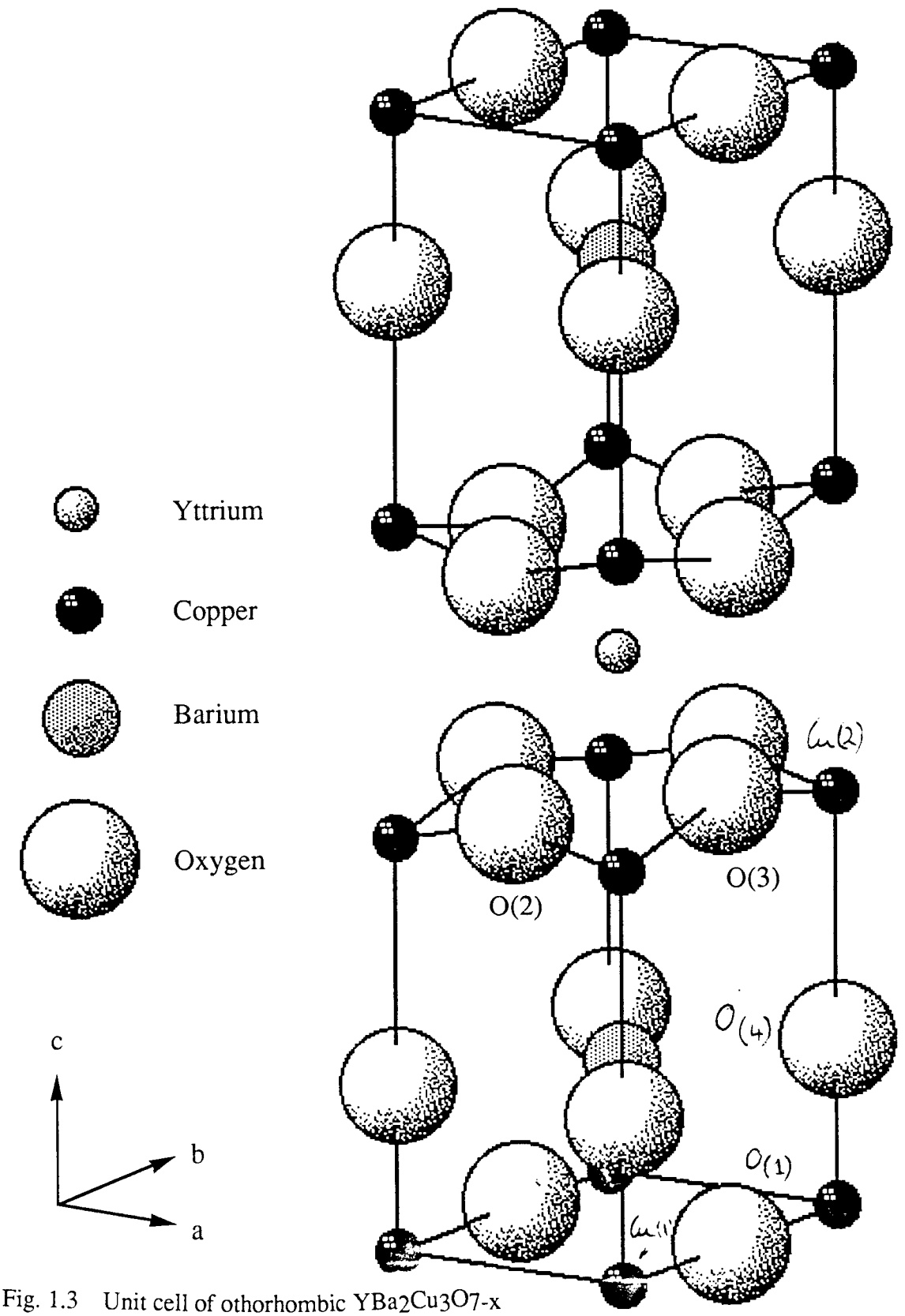

Fig. 1.3 Unit cell of othorhombic $YBa_2Cu_3O_{7-x}$

instabilities are typical for the class of perovskites. These instabilities may play a major role in superconductivity.

The structure of the $YBa_2Cu_3O_{7-x}$ superconductor is orthorhombic [9,10,11] at lower and pseudo-tetragonal at higher temperatures for a given oxygen concentration. The superconducting, orthorhombic structure can directly be derived from the perovskite structure by removing two oxygen atoms and replacing the cations appropriately.

As a consequence of the oxygen deficiency, the CuO_6-octahedrals degenerate to a fence-like formation of CuO_3 units in the (b, c) plane. The oxygen vacancies build a row along the a-axis. Because no oxygen is found in the Y plane, the copper ions are placed in a five-fold coordinated square pyramidal site. CuO_5 pyramidals are built along the c-axis.

The oxygen vacancies are found in the center of the unit cell coplanar with the Y atom in the (a,b) plane in between two neighboring Cu atoms. Taking all possible available oxygen sites into account, including vacancies, would result in a O_9 stoichiometry.

The oxygen concentration depends strongly on the processing conditions used to make the material. The total oxygen concentration in the sample is directly proportional to the oxygen concentration in the furnace atmosphere and the cooling rate of the sample.

Rietveld refinements of neutron diffraction data taken from oxygen deficient materials show that oxygen is lost primarily from the O(1) site in the chains.[12,13,14,15,16,17] In reduced material with six oxygen atoms per unit cell, the chain site is completely empty, which reduces the coordination of the Cu(1) atom to two and the structure of the unit cell is tetragonal.

A more simple explanation of this lattice structure is given by the image of a stack of CuO - BaO - CuO_2 - Y - CuO_2 - BaO - CuO layers, perpendicular to the c-axis

with CuO-chains running along the b-axis. Cu in the layer site is in a mixed valence state.

The following tables[18] show lattice parameters, atom coordinates, site occupancies, bond lengths and other properties of the tetragonal and the orthorhombic lattice:

	Space Group $P4/mmm$, $a = b = 3.8570(1)$ Å, $c = 11.8194(3)$ Å				
Atom	x	y	z	B_{iso} (Å^2)	Occupancy
Y	$\frac{1}{2}$	$\frac{1}{2}$	$\frac{1}{2}$	0.73(4)	1
Ba	$\frac{1}{2}$	$\frac{1}{2}$	0.1952(2)	0.50(4)	1
Cu(1)	0	0	0	1.00(4)	1
Cu(2)	0	0	0.3607(1)	0.49(3)	1
O(1)	0	$\frac{1}{2}$	0	0.9	0.028(4)
O(2)	0	$\frac{1}{2}$	0.3791(1)	0.73(4)	1
O(4)	0	0	0.1518(2)	1.25(6)	0.990(6)

Table 1.1 Atomic Positions and Occupancies for tetragonal $YBa_2Cu_3O_{6.06}$ [Ref.18]

Y–O(2)	8 × 2.4004(8)
Ba–O(2)	4 × 2.905(1)
Ba–O(4)	4 × 2.7751(5)
Cu(1)–O(4)	2 × 1.795(2)
Cu(2)–O(2)	4 × 1.9406(3)
Cu(2)–O(4)	2.469(2)

Table 1.2 Selected Bond lengths for tetragonal $YBa_2Cu_3O_{6.06}$ [Ref. 18]

Atom	Space Group x	y	$Pmmm$, z	a = 3.82030(8) Å, U_{11}(Å^2)	b = 3.88548(10) Å, U_{22}(Å^2)	c = 11.68349(23) Å U_{33}(Å^2)	Occup
Y	$\frac{1}{2}$	$\frac{1}{2}$	$\frac{1}{2}$	0.0085(8)	0.0106(8)	0.0085(6)	1
Ba	$\frac{1}{2}$	$\frac{1}{2}$	0.18393(6)	0.0078(6)	0.0096(7)	0.0198(5)	1
Cu(1)	0	0	0	0.0080(9)	0.0115(9)	0.0150(7)	1
Cu(2)	0	0	0.35501(8)	0.0033(5)	0.0036(5)	0.0207(5)	1
O(1)	0	$\frac{1}{2}$	0	0.0161(16)	0.0104(11)	0.0080(14)	0.910
O(2)	$\frac{1}{2}$	0	0.37819(15)	0.0039(6)	0.0068(7)	0.0203(11)	1
O(3)	0	$\frac{1}{2}$	0.37693(16)	0.0109(8)	0.0084(7)	0.0056(11)	1
O(4)	0	0	0.15840(13)	0.0162(11)	0.0123(9)	0.0097(7)	1

Table 1.3 Structural parameters of orthorhombic $YBa_2Cu_3O_{6.91}$ at room temperature [Ref. 18]

Y–O(2)	4 × 2.418(15)	Cu(1)–O(1)	2 × 1.947(5)
Y–O(3)	4 × 2.399(15)	Cu(1)–O(4)	2 × 1.834(27)
Ba–O(1)	2 × 2.891(2)	Cu(2)–O(2)	2 × 1.929(3)
Ba–O(2)	2 × 2.980(19)	Cu(2)–O(3)	2 × 1.961(3)
Ba–O(3)	2 × 2.948(19)	Cu(2)–O(4)	2.341(28)
Ba–O(4)	4 × 2.750(3)		
O(1)–Cu(1)–O(4)		90.0(5)	
O(4)–Cu(1)–O(4)		180.0(7)	
O(1)–Cu(1)–O(1)		180.0(0)	
O(3)–Cu(2)–O(3)		166.3(1)	
O(2)–Cu(2)–O(2)		165.3(7)	
O(2)–Cu(2)–O(3)		89.1(0)	
O(4)–Cu(2)–O(3)		96.9(6)	
O(4)–Cu(2)–O(2)		97.4(6)	

Table 1.4 Selected bond lengths and angles in orthorhombic $YBa_2Cu_3O_7$ [Ref. 18]

High temperature X-ray and neutron diffraction data[19] can be fitted to a tetragonal $YBa_2Cu_3O_6$ unit cell[20] with excess oxygen atoms distributed randomly in the CuO layer between the Ba planes. $YBa_2Cu_3O_6$ is not superconducting.

Investigations from several groups have been interpreted to show the orthorhombic-to-tetragonal-phase-transition occurs near x~0.6. The transition is also observed near 700° C for samples held in air or oxygen. When fitted to a variable strain orthorhombic cell model, X-ray and neutron diffraction data indicate that the strain (b-a) decreases continuously with increasing temperature and goes to zero at the transition.[21]

This effect, however, is not confirmed by local probe measurements such as PAC. PAC spectra on samples with x=0.05 show no substantial difference between measurements at room temperature and 950° C.

During the pseudo-phase transition, a micro-twinned structure[22,23,24,25] is formed, showing coherent twin planes parallel to the (110) direction. The structure occurs in domains and is repetitive with consecutive (110) planes. The CuO chains running along the b-axis stick through the domain boundaries, which affects currents transported along them.

The detected phase transition is an artifact of the global probe measurements because only an average over the Bragg spacings in a- and b-directions is taken into account. The micro-twinned structure of the crystal above 700° C provides an isotropical distribution of the Cu-O chains along the a-and the b-axis.

The CuO chains which are macroscopically destroyed during the phase transition provide the fact that only by global probe investigations like X-ray measurements, the pseudo-tetragonal phase can be seen at temperatures higher than 700° C in O_7.

The graph below indicates the temperature dependence of the lattice parameters.

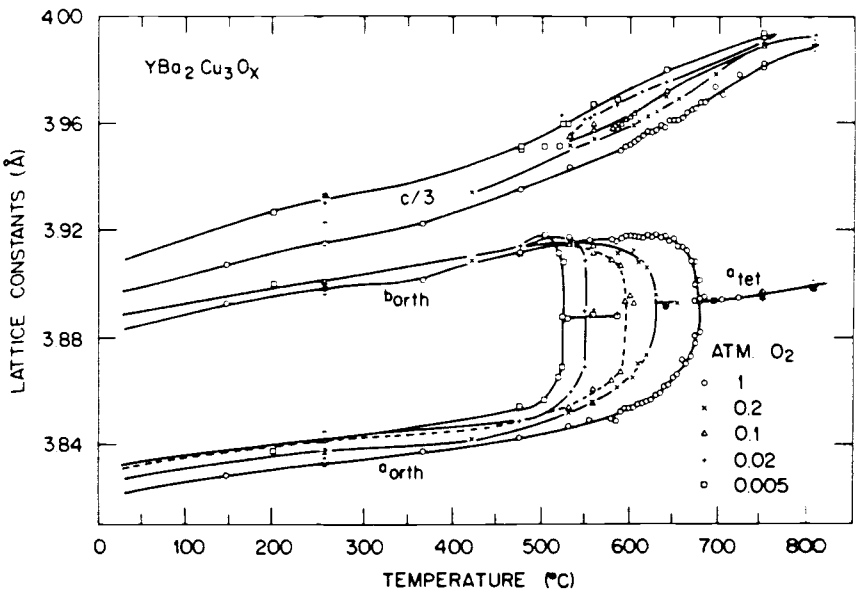

Fig.1.4 Lattice constants versus temperature for various oxygen partial pressures [Ref. 26]

1.3.3 SUPERCONDUCTIVITY IN $YBa_2Cu_3O_{7-X}$

Superconductivity is exclusively observed in the orthorhombic structured $YBa_2Cu_3O_{7-x}$. Experiments have shown that total replacement of Y by rare earth elements such as Gd has only little effect on T_c[27,28,29,30]. Therefore, the magnetic moment on the rare earth atoms can have only little interaction with superconducting electrons and the superconductivity is assumed to take place in the CuO_2 planes. The CuO chains, however, play a major role in the mechanism leading to superconductivity in the 1-2-3 compound and disorder of those chains tends to decrease T_c.

Experimental methods of investigating superconductivity properties include resistance vs. temperature measurements, Meissner-flux exclusion, and nuclear quadrupole

resonance measurements. Most of these measurements are performed near the transition from the non-superconducting to superconducting state in order to determine the onset of superconductivity exactly. The critical temperature T_C is defined to be at the sharp upper change of resistance, magnetization, etc..

The following table shows some rather important properties of superconductivity for the 1-2-3 compound[31].

Measured parameters	
Transition temperature midpoint	$T_c = 92.5$ K
Resistivity in the normal state	$\rho_{300} = 600-700\ \mu\Omega$ cm
	$\rho_{95} = 200-250\ \mu\Omega$ cm
Lower critical field slope	$dH_{c1}/dT = -7$ Oe K^{-1}
Upper critical field slope[a]	$dH_{c2}/dT = -13$ kOe K^{-1}
Critical current density (77 K, $H = 0$)	$j_c > 1100$ A cm^{-2}
Dominant carrier type (300 K)	p type
Derived parameters	
Sommerfeld parameter	$\gamma = 3-5$ mJ (mole Cu)$^{-1}$ K^{-2}
GL coherence length	$\xi(0) \sim 22$ Å
GL penetration depth	$\lambda(0) \sim 1400$ Å
GL κ	$\kappa \sim 62$
Thermodynamic critical field	$H_c(0) = 10 \pm 2$ kOe

Table 1.5 Material parameters for orthorhombic $YBa_2Cu_3O_{6.9}$ [Ref. 31]

$YBa_2Cu_3O_{7-x}$ is a type II superconductor, meaning that the transition to superconductivity is not abrupt. For the Meissner-flux exclusion experiment, rather than displaying a sharp transition, the compound undergoes a gradual change in magnetization, in which the magnetic field penetrates into the sample a finite distance, but not thoroughly. This state is called the Meissner or Schubnikov phase.

The following two figures display the magnetic susceptibility[21] and the ohmic resistance as a function of temperature.[32]

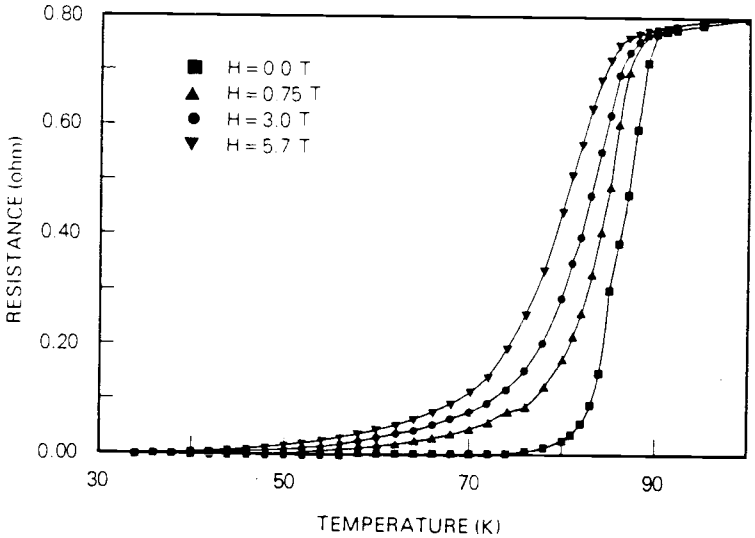

Fig. 1.5 Temperature dependence of resistance [Ref. 32]

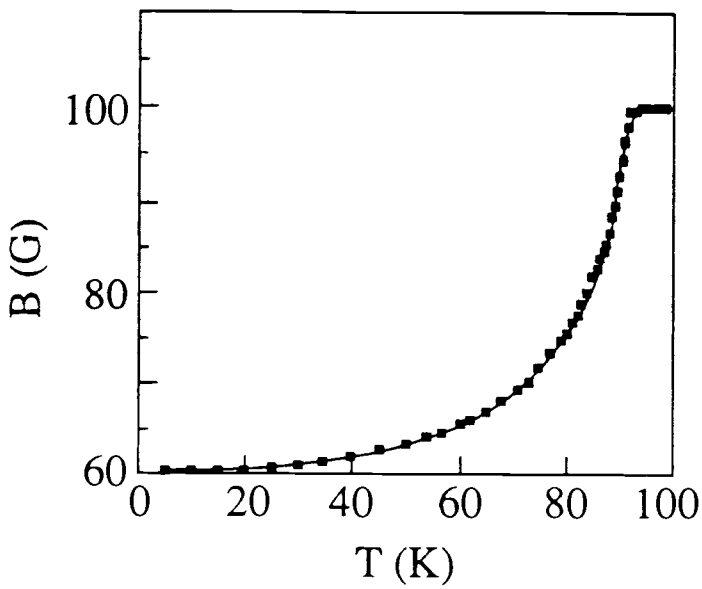

Fig. 1.6 Temperature dependence of magnetic susceptibility [Ref. 32]

In the first figure, the magnetic susceptibility undergoes an abrupt decrease at T_C and asymptotically approaches a constant value for decreasing temperatures. The decrease from $\chi_m = 0$ to the constant value at very low temperatures (of order 10 K) as well as the critical temperature itself depend mainly on the oxygen vacancy concentration and their motion, i.e. their relaxation time of the modified electric field gradient. The stoichiometry of oxygen O_{7-x} can vary between x=0 for the perfectly orthorhombic, superconducting structure and x=1 for tetragonal structure.

Fig.1.7 shows the total oxygen content vs. temperature for different oxygen partial pressures.[14] In order to obtain oxygen rich samples with optimal superconducting properties, corresponding to 7 oxygen atoms in the unit cell, it is crucial to cool the sample slowly. The oxygen atoms, which are not contained in the initial solution of nitrates accumulate in the bulk sample by diffusion.

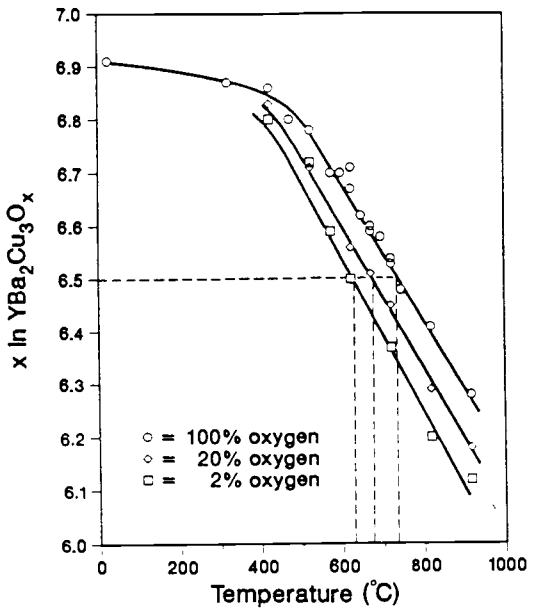

Fig 1.7 Total oxygen concentration as a function of temperature

The critical temperature depends in a rather complex way on the oxygen stoichiometry. The figure shows a step-like function T_c vs. x with a sharp plateau around 60 K between x≈0.3 and x≈0.4.

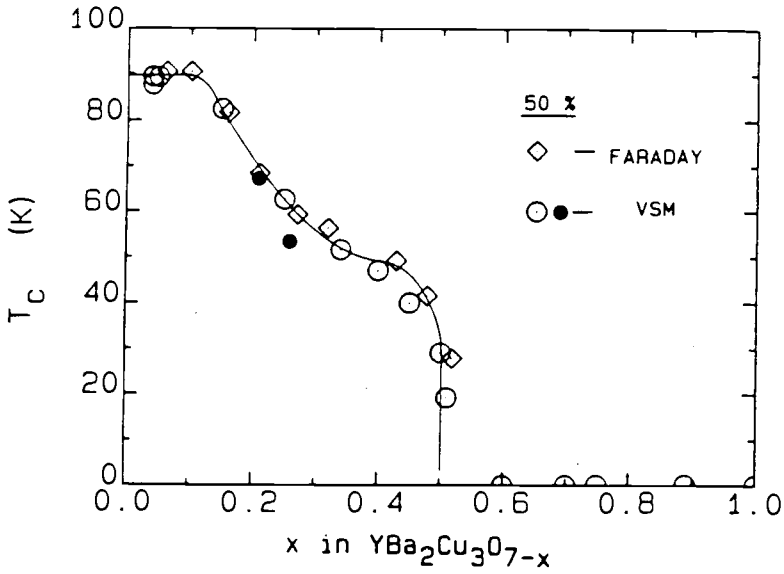

Fig. 1.8 Transition temperature T_c as a function of oxygen content x

As mentioned above, the transition width depends on the oxygen stoichiometry as well as the transition temperature.

1.3.4 TECHNICAL APPLICATIONS OF $YBa_2Cu_3O_{7-x}$

The critical temperature of the $YBa_2Cu_3O_{7-x}$ compound is 92.7 K, which increases the number of technical applications for this compound compared to low temperature superconductors, because inexpensive N_2 in liquid phase can be used as cooling material. N_2 has its boiling point at 75.5 K which is well below the critical temperature of the superconductor. Hence, the expensive use of liquid helium can be avoided.

Possible applications of the superconducting material are found in superconducting magnets for industrial and medical purposes, in power transmission lines, computer interconnections, Josephson devices, microwave cavities, and infrared radiation detectors.

2.THEORY OF X-RAY DIFFRACTION AND PERTURBED ANGULAR CORRELATION SPECTROSCOPY

2.1 X-RAY DIFFRACTION BY CRYSTALS

Diffraction of photons, neutrons, and electrons is used to study the structure of crystals. The global probe, represented by an electromagnetic wave, is scattered by a rigid array of ions. The resulting diffraction pattern, intensity vs. diffraction angle 2θ, is a unique signature of the crystal structure that reveals the location and character of the ions within a structure.

The two major factors determining the diffraction are the crystal structure and the wavelength of the incident wave. For wavelengths in the range of visible light, the elastic scattering by individual atoms results in ordinary optical diffraction. The wavelength of the incoming radiation has to be comparable with or smaller than the interatomic distances in order to obtain diffracted outgoing beams different from the incident direction. In a solid, typical interatomic distances are of the order Ångström ($1\text{Å}=10^{-10}$ m). The electromagnetic probe of the microscopic structure must therefore have a wavelength not exceeding this value. The corresponding energy is of the order of

$$\hbar\omega = \frac{hc}{\lambda} = \frac{hc}{10^{-8}\text{cm}} \approx 12.3 \times 10^{3}\text{eV} \qquad (2.1.1)$$

These energies are characteristic X-ray energies. Figure (1) shown below displays the wavelength vs. energy for X-ray photons, neutrons, and electrons[33].

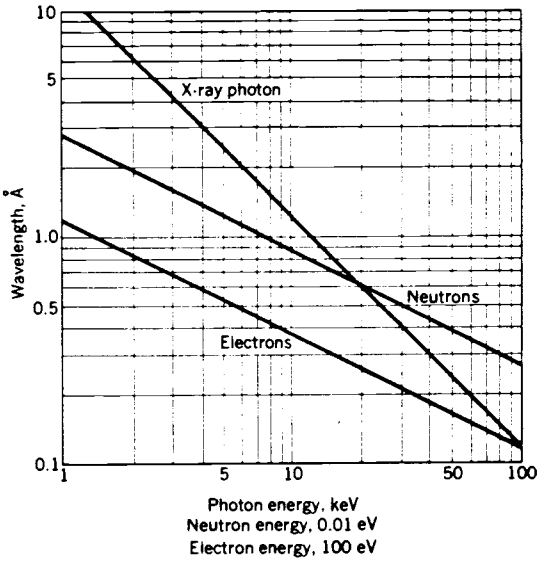

Fig. 2.1 Wave length vs. particle energy of photons, neutrons, and electrons

Two equivalent ways to view the scattering of X-rays by a perfect, periodic structure have been developed by W.L. Bragg and von Laue. Although both approaches are still in wide use, von Laue's theory exploits the reciprocal lattice and is overall closer to modern solid state physics. X-ray crystallography, on the other hand, still prefers Bragg's approach, being closer to practice of X-ray crystallography.

2.1.1 BRAGG FORMULATION

In 1913 W.H. and W.L.Bragg found that substances with macroscopic crystalline form gave remarkable characteristic patterns of reflected X-radiation. This led W.L.Bragg to the hypothesis of a crystal being made out of parallel planes of ions, spaced a distance d apart. He claimed two conditions which are necessary to detect a sharp peak in the intensity of the scattered radiation:

(1) The X-rays should be specularly reflected by the ions in any one plane

(2) The reflected rays from successive planes should interfere constructively.

Assuming a specular reflection from adjoining planes, the path difference of the two rays reflected from those planes is $2d\sin\theta$, where θ is the angle of incidence measured from the plane. Constructive interference of the radiation from successive planes occurs when the path difference is an integral number n of wavelengths λ, leading to the well-known Bragg condition:

$$n\lambda = 2d \sin \Theta, \qquad (2.1.2)$$

where n is known as the order of the corresponding reflection. As discussed above, this condition only holds for $\lambda \leq 2d$. Since λ determines the direction of reflection, θ is different for X-rays with different energies. It is obvious that there is an infinite number of possibilities of sectioning the crystal into Bragg planes. Each of those produces a separate set of reflections (see figures 2.2a and 2.3 below)[34].

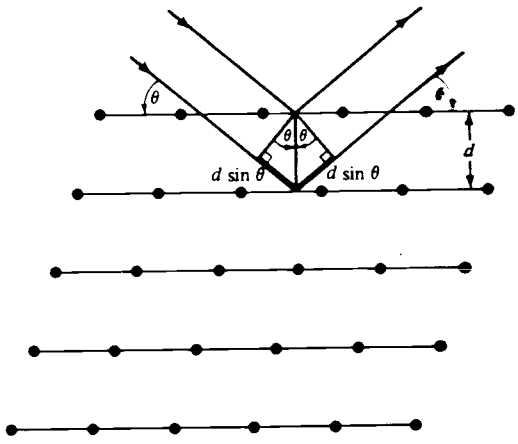

Fig. 2.2a Bragg reflection from a particular family of lattice planes

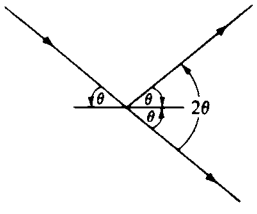

Fig. 2.2b Bragg angle θ in relation to the angle of deflection

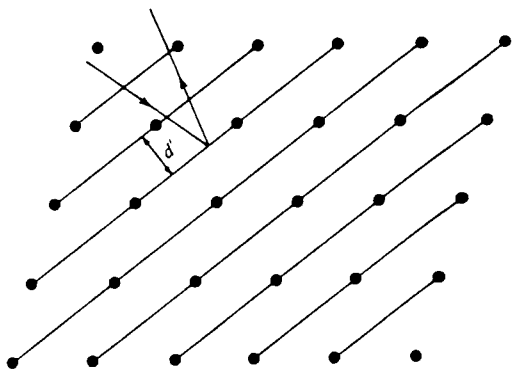

Fig. 2.3 Reflection of X-ray beam at different Bragg planes

Since each plane has a reflection coefficient of 10^{-3} to 10^{-5} of the incident radiation, 10^{3} to 10^{5} planes may contribute to the formation of the Bragg reflected beams in a perfect crystal.

The Bragg law does not refer to the composition of the basis of atoms associated with the lattice point in the Bragg plane. This composition, however, determines the relative intensity of the various orders of diffraction from a given set of parallel planes.

The following three subchapters will give a more rigid development of the theoretical considerations leading to diffraction of X-rays on a lattice. A brief introduction to a quantum-mechanical approach to scattering theory, Fourier analysis of the electron density and general, non-restricted diffraction conditions will be given as well as derivations leading to the geometric structure factor and the atomic form factor.

2.1.2 THE SCATTERED WAVE

The scattering process of X-rays is accomplished by electrons. Thus, the spatial distribution of electrons within each unit cell is the major factor determining the scattering characteristics. The scattering is caused by an interaction between the X-rays and the potential of the electrons.

A quantum-mechanical approach[35] to the theory of scattering starts from the solutions of Schrödinger's equation describing the evolution of a particle in the potential V(**r**). The solutions are stationary states and associated with well-defined energies E:

$$\Psi(\mathbf{r},t) = \varphi(\mathbf{r})e^{-i\frac{Et}{\hbar}}, \tag{2.1.3}$$

The Schrödinger equation:

$$\left[-\frac{\hbar^2}{2\mu}\Delta + V(\mathbf{r})\right]\varphi(\mathbf{r}) = E\varphi(\mathbf{r}), \tag{2.1.4}$$

where V(r) is the physical potential and $\varphi(r)$ is a solution of the eigenvalue equation.

Assuming a solution with a positive energy E, equal to the kinetic energy of the incident particle before it experiences the influence of the potential, the energy levels are defined to be:

$$E = \frac{\hbar^2 k^2}{2\mu} \quad . \tag{2.1.5}$$

Defining the potential as:

$$V(\mathbf{r}) = \frac{\hbar^2}{2\mu} U(\mathbf{r}) \quad , \tag{2.1.6}$$

enables to rewrite equation (2.1.4) to:

$$\left[\Delta + k^2 - U(\mathbf{r})\right]\varphi(\mathbf{r}) = 0 \quad . \tag{2.1.7}$$

For each value of k, equation (2.1.7) can be satisfied by an infinite number of solutions, i.e. the positive eigenvalues of the Hamiltonian H are infinitely degenerate. Not all the solutions, however, make physical sense. Only those solutions are taken into account that correspond to the physical problem being studied.

The eigenstates of the Hamiltonian satisfying the condition given by this problem are called stationary scattering states. The wave function will be designated to be $v_k^{(diff)}(r)$. After interaction with the potential, the scattered wave is now split into a transmitted wave packet travelling along the incident direction (having the form $e^{ikz)}$ and a scattered wave packet. Therefore, the wave function representing the stationary scattering state associated with a given energy $\hbar^2k^2/2\mu$, will be obtained from superposition of the plane wave e^{ikz} and a scattered wave.

The potential V(**r**), obviously, determines the structure of the scattered wave. For large **r** the wave must present the following characteristics:

(1) The radial dependence has to be of the form e^{ikz}/r for a given direction

(2) Since scattering is not isotropic, the amplitude of the outgoing wave depends on the direction.

Suppose that there exists a function G(**r**) such that equation (2.1.7) can be rewritten:

$$\left(\Delta + k^2\right)G(\mathbf{r}) = \delta(\mathbf{r}), \tag{2.1.8}$$

where G(**r**) is the "Green's function" of the operator $(\Delta + k^2)$. Any function $\varphi(\mathbf{r})$ satisfying

$$\varphi(\mathbf{r}) = \varphi_0(\mathbf{r}) + \int d^3r' G(\mathbf{r} - \mathbf{r}')U(\mathbf{r}')\varphi(\mathbf{r}'), \tag{2.1.9}$$

where $\varphi_0(r)$ is a solution of the homogeneous equation:

$$\left(\Delta + k^2\right)\varphi_0(\mathbf{r}) = 0 \tag{2.1.10}$$

and obeys the differential equation (2.1.7). Apply the operator $(\Delta + k^2)$ to both sides of equation (2.1.9) and taking the equation for φ_0 into account (2.1.10), leads to

$$(\Delta + k^2)\varphi(\mathbf{r}) = (\Delta + k^2)\int d^3r' G(\mathbf{r} - \mathbf{r}')U(\mathbf{r}')\varphi(\mathbf{r}'). \qquad (2.1.11)$$

Assuming that the operator can be moved inside the integral, it will act only on the variable r and equation (2.1.11) is transformed to:

$$(\Delta + k^2)\varphi(\mathbf{r}) = \int d^3r' \delta(\mathbf{r} - \mathbf{r}')U(\mathbf{r}')\varphi(\mathbf{r}') = U(\mathbf{r})\varphi(\mathbf{r}). \qquad (2.1.12)$$

Since every solution of (2.1.7) satisfies (2.1.9), the differential equation (2.1.7) can be replaced by (2.1.9). This integral scattering equation contains the information about the differential equation (2.1.7) and the asymptotic behavior required from the wave function.

To find the scattering equation, solve equation (2.1.8). $(\Delta + k^2)G(\mathbf{r})$ must be identical to zero in any region that does not include the origin. Furthermore, for small **r**, $G(\mathbf{r})$ must behave like $\frac{1}{4\pi r}$. Now the "Green's function" can be found to be:

$$G_{\pm}(\mathbf{r}) = -\frac{1}{4\pi}\frac{e^{\pm ikr}}{r}. \qquad (2.1.13)$$

Now one can write:

$$\Delta G_{\pm}(\mathbf{r}) = e^{\pm ikr}\Delta\left(-\frac{1}{4\pi r}\right) - \frac{1}{4\pi r}\Delta\left(e^{\pm ikr}\right) + 2\left[\nabla\left(-\frac{1}{4\pi r}\right)\right]\cdot\left[\nabla e^{\pm ikr}\right], \qquad (2.1.14)$$

which can be rewritten as

$$\Delta G_{\pm}(\mathbf{r}) = -k^2 G_{\pm}(\mathbf{r}) + \delta(\mathbf{r}). \qquad (2.1.15)$$

G_+ and G_- are called, respectively, the "outgoing and incoming Green's function". The form of the required asymptotic behavior suggests the choice of the incident plane wave e^{ikz} for $\varphi_0(r)$ and the choice for the outgoing "Green's function" $G_+(\mathbf{r})$ for $G(\mathbf{r})$. As we will see later, the integral scattering equation can be written as:

$$v_k^{(diff)}(\mathbf{r}) = e^{ikz} + \int d^3r' G_+(\mathbf{r} - \mathbf{r}')U(\mathbf{r}')v_k^{(diff)}(\mathbf{r}'). \qquad (2.1.16)$$

Introduce $\mathbf{r}$: the vector from the origin to the location of the particle and $\mathbf{r}'$: the vector from the origin to the point of the zone of influence of the potential.

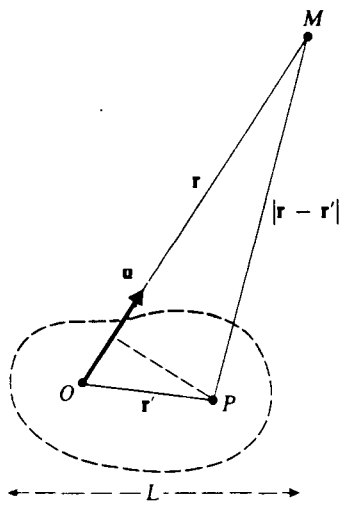

Fig. 2.4 Approximate calculation of the distance | **r** - **r'** |

u is the unit vector in the direction of **r**. Within a good approximation,

$$|\mathbf{r}-\mathbf{r}'| \approx r - \mathbf{u}\cdot\mathbf{r}'. \tag{2.1.17}$$

For large **r**, $G_+(\mathbf{r}-\mathbf{r}')$ becomes

$$G_+(\mathbf{r}-\mathbf{r}') = -\frac{1}{4\pi}\frac{e^{ik|\mathbf{r}-\mathbf{r}'|}}{|\mathbf{r}-\mathbf{r}'|} \underset{r\to\infty}{\approx} -\frac{1}{4\pi}\frac{e^{ikr}}{r}e^{-ik\mathbf{u}\cdot\mathbf{r}'}. \tag{2.1.18}$$

If the expression above is substituted into equation (2.1.16), the asymptotic behavior of $v_k^{(diff)}(\mathbf{r})$ is obtained by

$$v_k^{(diff)}(\mathbf{r}) \underset{r\to\infty}{\approx} e^{ikz} - \frac{1}{4\pi}\frac{e^{ikr}}{r}\int d^3r' e^{-ik\mathbf{u}\cdot\mathbf{r}'}U(\mathbf{r}')v_k^{(diff)}(\mathbf{r}'). \tag{2.1.19}$$

This is no longer a function of **r** but only of the angles ϑ and φ. If the scattering factor $f_k(\vartheta,\varphi)$ is taken to be

$$f_k(\vartheta,\varphi) = -\frac{1}{4\pi}\int d^3r' e^{-ik\mathbf{u}\cdot\mathbf{r}'}U(\mathbf{r}')v_k^{(diff)}(\mathbf{r}'), \tag{2.1.20}$$

we obtain the final form of $v_k^{(diff)}(\mathbf{r})$:

$$v_k^{(diff)}(\mathbf{r}) \underset{r\to\infty}{\approx} e^{ikz} + f_k(\vartheta,\varphi)\frac{e^{ikr}}{r}. \tag{2.1.21}$$

This shows that the solution of the integral scattering equation (2.1.16) are the stationary scattering states. Equation (2.1.21) is also the solution to the eigenvalue equation (2.1.7) satisfying the condition required from the integral scattering equation.

The differential cross section $\sigma(\theta,\varphi)$ which is the physical magnitude commonly used in scattering experiments, can be calculated directly from the scattering factor $f_k(\theta,\varphi)$:

$$\sigma(\vartheta,\varphi) = \left|f_k(\vartheta,\varphi)\right|^2. \qquad (2.1.22)$$

2.1.3 FOURIER ANALYSIS OF ELECTRON DENSITY

In X-ray diffraction experiments, the scattering potentials are generated by electrons in the outermost shell of the lattice atoms. Since those lattice atoms are arranged in a periodic manner, the number density of the scattering electrons obeys a periodic distribution with respect to the crystal axes directions.

2.1.3.1 ONE-DIMENSIONAL CASE

The above mentioned periodicity of the scattering electrons is the reason to apply Fourier analysis to the electron number density $n(\mathbf{r})$. Assume the ideal case of an infinite, perfect crystal. In this case, the crystal is invariant under any translation of the form $T = u_1\mathbf{a}_1 + u_2\mathbf{a}_2 + u_3\mathbf{a}_3$, where u_1, u_2, u_3 are integers and $\mathbf{a}_1$, $\mathbf{a}_2$, $\mathbf{a}_3$ are the crystal axes.

Hence,

$$n(\mathbf{r} + \mathbf{T}) = n(\mathbf{r}). \tag{2.1.23}$$

The Fourier components of the electron number density contain the most interesting properties of the crystal. Consider first a one-dimensional function n(x) with a periodic dependence on x. Now n(x) can be expanded in a Fourier series consisting of a sum of sine and cosine functions:

$$n(x) = n_0 + \sum_{p>0}\left[C_p \cos\left(\frac{2\pi px}{a}\right) + S_p \sin\left(\frac{2\pi px}{a}\right)\right]. \tag{2.1.24}$$

The p's are positive integers and C_p and S_p are real constants, called the Fourier coefficients of the series. The factor $\frac{2\pi}{a}$ indicates that the series has the period a. The values $\frac{2\pi}{a}$ refer to distances in the Fourier space of the crystal.

These reciprocal lattice points indicate the allowed terms in the Fourier series obeying the periodicity of the lattice.

When the sum is taken over all integers p, the Fourier series (2.1.24) can be rewritten:

$$n(x) = \sum_{p} n_p e^{i2\pi px/a}. \tag{2.1.25}$$

Set $\varphi = \frac{2\pi px}{a}$; if $n^*_{-p} = n_p$, the sum in equation (2.1.25) can be written as

$$n_p(\cos\varphi + i\sin\varphi) + n_{-p}(\cos\varphi - i\sin\varphi) = (n_p + n_{-p})\cos\varphi + i(n_p - n_{-p})\sin\varphi \tag{2.1.26}$$

This is equal to the real function

$$2\,\mathrm{Re}\{n_p\}\cos\varphi + 2\,\mathrm{Im}\{n_p\}\sin\varphi . \tag{2.1.27}$$

The number density n(x) is therefore a real function.

2.1.3.2 THREE-DIMENSIONAL CASE

To apply Fourier analysis for a three-dimensional function n(**r**), a set of reciprocal lattice vectors has to be found to satisfy the following equation:

$$n(\mathbf{r}) = \sum_{\mathbf{G}} n_{\mathbf{G}}(e^{i\mathbf{G}\cdot\mathbf{r}}) , \tag{2.1.28}$$

where n(**r**) still has to remain invariant under all crystal translations **T** which leave the crystal invariant. The set of Fourier coefficients $n_{\mathbf{G}}$ determines the X-ray scattering amplitude.

The Fourier series (2.1.25) can be inverted and the calculation of n_G results in

$$n_G = V_c^{-1} \int_{cell} dV n(\mathbf{r}) e^{-i\mathbf{G}\cdot\mathbf{r}}, \qquad (2.1.29)$$

where V_c is the volume of the unit cell of the crystal.

2.1.4 DIFFRACTION CONDITION

Let's assume the most general case about the outgoing wave where no direction is preferred. Let two volume elements dV be a distance **r** apart. Wave vectors of the incident and outgoing waves are **k** and **k'**. For the most general case of non-determined direction of outgoing radiation, the difference in phase of two parallel incident waves is exp (i[**k** - **k'**] **r**).

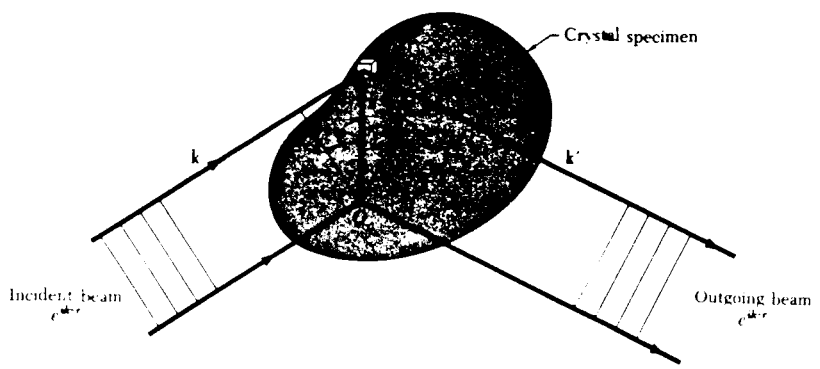

Fig. 2.5 Difference in path length of the incident wave **k** after diffraction

The amplitude of the wave is determined by the local electron concentration n(**r**). The total amplitude of the wave at point **r** in real space is proportional to

$$F = \int dV n(\mathbf{r}) e^{i(\mathbf{k}-\mathbf{k}')\cdot\mathbf{r}} = \int dV n(\mathbf{r}) e^{-i\Delta\mathbf{k}\cdot\mathbf{r}}, \qquad (2.1.30)$$

where F is called the scattering amplitude. $\Delta\mathbf{k}$ is defined as $\mathbf{k} + \Delta\mathbf{k} = \mathbf{k}'$. In other words, $\Delta\mathbf{k}$ measures the difference in wave vector and is called the scattering vector.

Introduce the Fourier components into (2.1.30) to obtain a different form for the scattering amplitude:

$$F = \sum_{\mathbf{G}} \int dV n_{\mathbf{G}} \{ e^{i(\mathbf{G}-\Delta\mathbf{k})\cdot\mathbf{r}} \}. \qquad (2.1.31)$$

Only for the case of $\Delta\mathbf{k} = \mathbf{G}$, the argument of the exponential vanishes and the remaining expression for F is $Vn_{\mathbf{G}}$. For X-ray diffraction, the photons are scattered elastically and the frequency of the outgoing wave is equal to the frequency of the incident wave, i.e. $k^2 = k'^2$. This result is also valid for electron and neutron scattering.

With the assumption $\Delta\mathbf{k} = \mathbf{G}$, or $\mathbf{k}' = \mathbf{G} + \mathbf{k}$, the diffraction condition

$$(\mathbf{k} + \mathbf{G})^2 = k^2$$
$$\Rightarrow 2\mathbf{k}\cdot\mathbf{G} + G^2 = 0 \qquad \text{follows.} \qquad (2.1.32)$$

Because **G** is a reciprocal lattice vector, so is (-**G**) and equation (3.1.32) becomes

$$2\mathbf{k}\cdot\mathbf{G} = G^2. \qquad (2.1.33)$$

The spacing between parallel lattice planes being normal to the direction **G** is

$$d(hkl) = \frac{2\pi}{|\mathbf{G}|} \tag{2.1.34}$$

and

$$|\mathbf{k}| = \frac{2\pi}{\lambda}\,. \tag{2.1.35}$$

Now equation (2.1.33):

$$2\left(\frac{2\pi}{\lambda}\right)|\mathbf{G}|\sin\theta = \frac{2\pi|\mathbf{G}|}{d(hkl)}, \tag{2.1.36}$$

or

$$2d(hkl)\sin\theta = \lambda, \tag{2.1.37}$$

which is a reformulation of the Bragg condition. θ is the angle between the incident plane with vector **k** and the crystal plane perpendicular to **G**. The reciprocal lattice vector **G**, however, is not defined exactly by its Miller indices h,k,l. A common factor, n, is not determined. Equation (2.1.37) can be written in a more general form:

$$2d(hkl)\sin\theta = n\lambda. \tag{2.1.38}$$

This is the same form as in equation (2.1.2).

2.1.5 VON LAUE FORMULATION

Von Laue used another way of expressing the diffraction condition $\Delta\mathbf{k} = \mathbf{G}$. His approach captivates by its simple geometrical explanation.

Von Laue considered the two scattering points in figure (2.5) to be a vector **r** apart. From this figure it is obvious that for constructive interference, the following condition has to be true:

$$\mathbf{r}\,(\,\mathbf{n} - \mathbf{n}'\,) = m\,\lambda, \tag{2.1.39}$$

where m is an integral number and **n**, **n'** are the unit vectors along **k**, **k'**.

Multiply both sides by $\frac{2\pi}{\lambda}$ and the relation for the incident and emergent wave vectors is represented by:

$$\mathbf{r}\,(\,\mathbf{k} - \mathbf{k}'\,) = 2\pi m. \tag{2.1.40}$$

If **r** is expressed by its components with respect to the basic lattice vectors of the real lattice, equation (2.1.40) can be expressed :

$$\begin{aligned} \mathbf{a}_1 \cdot \Delta\mathbf{k} &= 2\pi v_1; \\ \mathbf{a}_2 \cdot \Delta\mathbf{k} &= 2\pi v_2; \\ \mathbf{a}_3 \cdot \Delta\mathbf{k} &= 2\pi v_3, \end{aligned} \tag{2.1.41}$$

where v_1, v_2, and v_3 are the components with respect to the lattice vectors of the reciprocal lattice.

The above set of equations has an astonishingly simple geometrical explanation : The first equation requires that $\Delta\mathbf{k}$ lies on a cone around the direction of $\mathbf{a_1}$; to obey the second equation, $\Delta\mathbf{k}$ must be on a cone about $\mathbf{a_2}$; finally, corresponding to the third equation, the vector $\Delta\mathbf{k}$ is found on a cone about $\mathbf{a_3}$. To obtain constructive interference, all the conditions have to be satisfied and $\Delta\mathbf{k}$ is required to be along the common line of intersection of the three cones.

2.1.6 GEOMETRICAL STRUCTURE FACTOR AND ATOMIC FORM FACTOR

a) Monatomic lattice with a basis

In a monatomic lattice with an n-atomic basis, the members of the basis are designated by the basis vectors $\mathbf{d_1}, \mathbf{d_2}, \ldots, \mathbf{d_n}$. The intensity of radiation into a specific direction depends certainly on the interference of the scattering centers at the basis sites with each other. Since constructive interference is usually related to interference of two waves which have a difference in phase vector $\Delta\mathbf{k}$ (meaning that they are scattered beams emerging from different scatterers), the path difference of the two waves is given as :

$$\Delta\mathbf{k} \; (\mathbf{d_i} - \mathbf{d_j}), \tag{2.1.42}$$

where the indices i,j indicate the members of the basis.

The diffraction condition requires $\Delta \mathbf{k} = \mathbf{G}$, the difference in phase vector will be

$$e^{iG(\mathbf{d_i} - \mathbf{d_j})}. \tag{2.1.43}$$

The total intensity of the wave scattered by atoms within the primitive cell will be proportional to the sum of the phase vectors caused by the members of the primitive cell. This sum is called the geometrical structure factor:

$$S_{\mathbf{G}} = \sum_{j=1}^{n} e^{i\mathbf{G}\mathbf{d}_j} \tag{2.1.44}$$

Instead of considering the lattice points to be point scatterers, the more physical approach, again, is to start from the electron density $n(\mathbf{r})$ which causes the scattering potential. Within the basis of the unit cell, the electron density can be written as:

$$n(\mathbf{r}) = \sum_{j=1}^{S} n_j\left(\mathbf{r} - \mathbf{r_j}\right) \tag{2.1.45}$$

Now, the geometrical structure factor has the form:

$$S_{\mathbf{G}} = \sum_j \int dV n_j(\mathbf{r} - \mathbf{r_j}) e^{-i\mathbf{G}\cdot\mathbf{r}} = \sum_j e^{-i\mathbf{G}\mathbf{r}_j} \int dV n_j(\bar{\rho}) e^{-i\mathbf{G}\bar{\rho}}, \tag{2.1.46}$$

where the integral includes one whole unit cell.

The intensity of the Bragg peak is proportional to the square of the absolute value of the amplitude and will, therefore, contain the factor $|S_{\mathbf{G}}|^2$.

The structure factor, however, is not the only factor determining the magnitude of the intensity of a Bragg peak. Rather, the ordinary angular dependence of an electromagnetic wave during a scattering process and the structure of the electron distribution for different types of ions within the unit cell have also to be taken into account. The latter aspect will be discussed in the following subchapter.

b) Polyatomic lattice with a basis

In the more general case of a lattice with a basis which contains different ions, the structure factor appears modified, because the different electron densities and structures contribute differently. The structure factor assumes the form

$$S_{\mathbf{G}} = \sum_{j=1}^{n} f_j(\mathbf{G}) e^{i\mathbf{G}\cdot\mathbf{d}_j} \qquad (2.1.47)$$

The factors f_j are the atomic form factors which are determined by the number and distribution of the atomic electrons of the jth ion at $\mathbf{d}_j$. They also depend on the wave length λ and the scattering angle.

The atomic form factor is a measure of the scattering power caused by the jth ion in the unit cell. It is defined as the ratio of the radiation amplitude scattered by the actual electron distribution in an atom over the radiation amplitude scattered by one electron at

the same location. For the monatomic lattice, the above expression reduces back to the geometrical structure factor in equation (2.1.44).

The atomic form factor associated with a given reciprocal lattice vector **G** is proportional to the Fourier transform of the electron density of the ion of interest:

$$f_j = \int dV n_j(\vec{\rho}) e^{-iG \cdot \vec{\rho}} \qquad (2.1.48)$$

To show the relation between the above atomic form factor and the atomic electrons, it is worth mentioning that for $\Delta \mathbf{k} = \mathbf{G} = \mathbf{0}$ or $(\mathbf{r} - \mathbf{r_j}) = \mathbf{0}$, f_j reduces to

$$f_j = \int dV n_j(\mathbf{0}) = Z \ , \qquad (2.1.49)$$

where Z is the atomic number of the atom.

In general, the structure factor is not real. The intensity, however, is proportional to $| S_G |^2$ and hence will always be a real and physically meaningful magnitude. Because of the **G** dependence for different form factors, it is possible to distinguish between various possible crystal structures on the basis of the variation of the Bragg intensities with **G**.

2.2 PERTURBED ANGULAR CORRELATION SPECTROSCOPY

2.2.1 INTRODUCTION AND APPLICATION OF PAC STUDIES IN $YBa_2Cu_3O_{7-x}$

Perturbed angular correlation of γ rays (PAC) is a nuclear technique that allows sampling of the hyperfine fields at the site of the probe nucleus.[36,37] Probe nuclei are radio-active ^{111}In atoms substituted at specific sites in the lattice. Similar to the global probe X-ray diffraction spectroscopy, PAC is used for lattice structure investigations. However, PAC is much more sensitive to short-range structural details of the lattice, such as impurity introduction and positional distortions of the atoms or ions forming the lattice. Gamma ray penetration depths of order centimeters make PAC a bulk probe that is easy to use at high temperatures.

A major problem during the PAC experiment is the introduction of the probe nuclei. In the case of the Y-Ba-Cu-O system, the original sample is prepared from a mixture of nitrate solutions. The In probe, which is dissolved in hydrochloric acid, is added to the mixture .

Since $YBa_2Cu_3O_{7-x}$ is a nonmagnetic compound and the ^{111}In probe is a closed electronic shell ion, only the interaction between the electric field gradient (EFG), influenced by the ionic environment of the probe site, and the electric quadrupole moment of the probe is significant. The EFG spectrum depends on the short-range order of every probe site. For a pure, high quality sample of the Hi T_c superconducting oxide with 7 oxygen atoms per unit cell, a discrete spectrum is expected, because all probe nuclei experience the same EFG.

For lower quality samples which contain migrating impurities, a distribution of EFG's is obtained. PAC is sensitive to these impurities and can therefore be used for

studies of sample purity, which depends on the preparation of the sample and its thermal history.

As characteristics of the migration of oxygen vacancies in the 1-2-3 system, the vacancy diffusion rate and concentration are obvious objects of investigation.

2.2.2 ANGULAR CORRELATION OF GAMMA RADIATION EMITTED BY FREE NUCLEI

Radiation emitted by atoms or nuclei during an electronic or nuclear transition displays an angular distribution with respect to a given axis of quantization. In a macroscopic sample the nuclei are randomly oriented, which results in an isotropic distribution of the emitted radiation.

The PAC experiment is based on this fact and selects from a group with random nuclear orientations only those that are oriented along a given direction. This idea requires a nuclear decay that consists of two successive emissions of radiations, where the first radiation is used to establish a quantization axis against which the second radiation is correlated. This process selects nuclei preferentially radiating in the direction of the first detector without the need of orienting the entire system.

In a nuclear cascade $I_i \rightarrow I \rightarrow I_f$, consisting of two successive transitions, two γ rays, γ_1 and γ_2, are emitted. The probability for emission of γ_1 and γ_2 in directions $\mathbf{k_1}$, $\mathbf{k_2}$ into the solid angles $d\Omega_1$, $d\Omega_2$ is denoted as $W(\mathbf{k_1},\mathbf{k_2},t)d\Omega_1 d\Omega_2$, where $W(\mathbf{k_1},\mathbf{k_2},t)$ is called the angular correlation function. The angular correlation function depends on the time separation of the two successive radiations.

In density matrix formalism, the angular correlation function has the form

$$W(\mathbf{k_1},\mathbf{k_2}) = \mathrm{Tr}\,[\,\rho(\mathbf{k_1})\rho(\mathbf{k_2})\,]\ , \tag{2.2.1}$$

where $\rho(\mathbf{k_1})$ and $\rho(\mathbf{k_2})$ are the density operators describing the states of the system after emission of γ_1 and γ_2. In the case of a free nucleus, no external fields are taken into account and therefore, neither ρ depends on time. The matrix element of the density operator can be written as

$$<a|\rho(\mathbf{k_1})|a'> = \sum_{k_1 N_1} (-1)^{2I - I_i + a} (2k_1+1)^{\frac{1}{2}} A_{k_1} \begin{pmatrix} I & I & k_1 \\ a' & -a & N_1 \end{pmatrix} D^{k_1}_{N_1 0}(\mathbf{z} \rightarrow \mathbf{k_1}) \tag{2.2.2}$$

and analogously for $\rho(\mathbf{k_2})$. Using the orthonormality of the Wigner 3-j symbols, the angular correlation function (2.2.1) becomes

$$W(\mathbf{k_1},\mathbf{k_2}) = \sum_{kN} (-1)^k A_k(1) A_k(2) D^k_{N0}(\mathbf{z} \rightarrow \mathbf{k_1}) D^k_{0N}(\mathbf{k_2} \rightarrow \mathbf{z}) \tag{2.2.3}$$

Introduction of $A_{kk} = A_k(1)A_k(2)$, averaging over the directions of $\mathbf{k_1}$ with angle θ between $\mathbf{k_1}$ and $\mathbf{k_2}$ and summation over N leads to

$$W(\vartheta) = \sum_{\substack{k=0 \\ \text{even}}}^{k_{max}} A_{kk} P_k(\cos\vartheta) \tag{2.2.4}$$

2.2.3 EXTRANUCLEAR PERTURBATIONS

A time-dependent perturbation applied to the system during the cascade $I_i \rightarrow I \rightarrow I_f$ can possibly change the m state population of the intermediate state I. For this case, the time evolution of the density matrices has to be taken into account. The time evolution operator is a function of the time-dependent interaction containing the Hamiltonian K:

$$\Lambda(t) = \exp\left\{-\frac{1}{\hbar}\int_0^t K(t')dt'\right\}. \tag{2.2.5}$$

With a, a' being the sublevels of the intermediate state I, the time-dependent correlation function can be written:

$$W(\mathbf{k_1},\mathbf{k_2},t) = \sum_{aa'} <a|\rho(\mathbf{k_1},t)|a'><a'|\rho(\mathbf{k_2},0)|a> = \mathrm{Tr}[\rho(\mathbf{k_1},t)\rho(\mathbf{k_2},0)], \tag{2.2.6}$$

where the first matrix element is

$$<a|\rho(\mathbf{k_1},t)|a'> = \sum_{bb'k_1N_1}\sum (-1)^{2I-I_i+b}(2k_1+1)^{\frac{1}{2}}A_{k_1}(1)\begin{pmatrix} I & I & k_1 \\ b' & -b & N_1 \end{pmatrix} \times D^{k_1}_{N_1 0}(\mathbf{z}\rightarrow\mathbf{k_1}) \times <a|\Lambda(t)|b><a'|\Lambda(t)|b'>^* \tag{2.2.7}$$

and the second one is

$$<a'|\rho(\mathbf{k_2},0)|a>=\sum_{k_2N_2}(-1)^{k_2-I_f-a}(2k_2+1)^{\frac{1}{2}}A_{k_2}(2)\begin{pmatrix} I & I & k_2 \\ a' & -a & N_2 \end{pmatrix}D^{k_2}_{N_2 0}(\mathbf{z}\rightarrow\mathbf{k_1}) \tag{2.2.8}$$

The angular correlation function (2.2.6) becomes

$$W(\mathbf{k_1},\mathbf{k_2},t)=\sum_{k_1k_2}\sum_{N_1N_2}(-1)^{N_1+N_2}\frac{1}{4\pi}A_{k_1}(1)A_{k_2}(2)G^{N_1N_2}_{k_1k_2}(t)$$

$$\times D^{k_1}_{N_1 0}(\mathbf{k_1}\rightarrow\mathbf{z})D^{k_2}_{N_2 0}(\mathbf{k_2}\rightarrow\mathbf{z}). \tag{2.2.9}$$

$$G^{N_1N_2}_{k_1k_2}(t)=\sum_{\substack{aa'\\bb'}}(-1)^{2I+a+b}\left\{(2k_1+1)(2k_2+1)\right\}^{\frac{1}{2}}\begin{pmatrix} I & I & k_1 \\ a' & -a & N_1 \end{pmatrix}\begin{pmatrix} I & I & k_2 \\ b' & -b & N_2 \end{pmatrix}$$

$$\times <a|\Lambda(t)|b><a'|\Lambda(t)|b'>^*. \tag{2.2.10}$$

$G^{N_1N_2}_{k_1k_2}(t)$ is defined to be the perturbation function and contains all physical information about the interaction of the nuclei with the perturbation.

2.2.3.1 STATIC PERTURBATIONS

If the perturbation originates from an extra-nuclear field that is constant in direction and magnitude, the m-levels associated with the intermediate state I are stationary. In the ideal case of a perfect lattice with the nuclei on equivalent sites, the perturbation K does not depend on time and equation (2.2.5) can be rewritten as:

$$\Lambda(t) = e^{-\frac{i}{\hbar}Kt}. \tag{2.2.11}$$

U is the unitary operator which diagonalizes the time-independent interaction Hamiltonian K :

$$UKU^{-1} = E. \tag{2.2.12}$$

E represents the diagonalized Hamiltonian, the energy eigenvalues E_n to be found on its diagonal. The time evolution operator in (2.2.11) can be written as a function of the diagonalized Hamiltonian :

$$\Lambda(t) = U^{-1} e^{-\frac{i}{\hbar}Et} U. \tag{2.2.13}$$

The elements of the matrix $\Lambda(t)$ have the following form :

$$< a|\Lambda(t)|b >= \sum_{n} < a|n >< b|n >^{*} e^{-int} \quad , \tag{2.2.14}$$

where $|n>$ are the eigenstates of K and e^{-int} is used as abbreviation for $e^{-iE_n t/\hbar}$.

Now the perturbation factor is modified to be :

$$G_{k_1 k_2}^{N_1 N_2}(t) = \sum_{\substack{aa' \\ bb'}} \sum_{nn'} (-1)^{2I+a+b} \left[(2k_1+1)(2k_2+1)\right]^{\frac{1}{2}} \begin{pmatrix} I & I & k_1 \\ a' & -a & N_1 \end{pmatrix} \begin{pmatrix} I & I & k_2 \\ b' & -b & N_2 \end{pmatrix}$$

$$\times e^{-i(n-n')t} < a|n >< a'|n'>^{*} < b|n >^{*} < b'|n'>. \tag{2.2.15}$$

This is the most general expression for the perturbation factor which determines directly the angular correlation.

For axial symmetry of the interaction, the symmetry axis is normally chosen to be the quantization axis. In the case of radiation being parallel to the symmetry axis of the perturbing field, the angular correlation function is equal to its unperturbed form.

In angular correlation experiments, the sample is used in powder form. The powder consists of an ensemble of microcrystals with random orientation. To obtain the angular correlation function for bulk samples, the interaction Hamiltonian K has to be transformed from the lab system to the principal axis system of the individual microcrystal. Using this transformed interaction Hamiltonian and equation (2.2.12), the time evolution operator for a microcrystal system can be found. The next step is to

derive the perturbation factor $G_{k_1k_2}^{N_1N_2}$. This expression has to be averaged over all orientations of the randomly oriented microcrystals. Now the perturbation factor is the average of the perturbation factors of the single crystals $G_{kk}^{pp}(t)$:

$$G_{kk}(t) = \frac{1}{2k+1} \sum_{p=-k}^{k} G_{kk}^{pp}(t) \qquad (2.2.16)$$

The final expression for the perturbation factor for a powder source becomes

$$G_{kk}(t) = \sum_{n} S_{nn}^{kk} + \sum_{n \neq n'} S_{nn'}^{kk} \cos\left[\frac{(E_n - E_{n'})t}{\hbar}\right], \qquad (2.2.17)$$

where

$$S_{nn'}^{k_1k_2} = \sum_{\substack{m_1m_1' \\ m_2m_2'}} (-1)^{2I+m_1+m_2} \begin{pmatrix} I & I & k_1 \\ m_1' & -m_1 & p \end{pmatrix} \begin{pmatrix} I & I & k_2 \\ m_2' & -m_2 & p \end{pmatrix}$$
$$\times < m_1 | n >< m_1' | n' >^* < m_2 | n >^* < m_2' | n' >. \qquad (2.2.18)$$

When $G_{kk}(t)$ is inserted for the expression for angular correlation function, the sum over N_1 and N_2 can be performed since the perturbation factor is independent of N_1 and N_2. After applying the addition theorem for the spherical harmonics, the angular correlation function simplifies to

$$W(\vartheta, t) = \sum_{\substack{k=0 \\ \text{even}}}^{k_{max}} A_{kk} G_{kk}(t) P_k(\cos\vartheta) \qquad (2.2.19)$$

Very often perturbation factors are referred to as attenuation factors. The time independent term in the perturbation factor of a polycrystalline source, $\sum_n S_{NN}^{kk}$, is called the hard core because it provides a non-vanishing time-independent angular correlation of a powder source. In the important case where the perturbation is axially symmetric, the non-vanishing angular correlation is caused by nuclei emitting γ-rays along the symmetry axis. Those nuclei are not affected by the perturbation.

2.2.4 THE STATIC ELECTRIC QUADRUPOLE INTERACTION

The perturbation of the angular correlation is caused by an electric field gradient (EFG) at the probe site. The quadrupole moment of the nucleus interacts with the EFG. All other interactions of different electric moments with the electric fields are negligible. The interaction Hamiltonian is of the form :

$$H_{QI} = \frac{4\pi}{5} \sum_{\mu=-2}^{2} (-1)^{\mu} q_{\mu}^{(2)} V_{-\mu}^{(2)} , \qquad (2.2.20)$$

where $q^{(2)}$ is the second-rank tensor operator of the nuclear quadrupole moment and $V^{(2)}$ the classical electric field gradient operator. In the above equation $V^{(2)}$ is written in spherical components. These can be expressed in terms of η and V_{zz}.

η is called the asymmetry parameter and is defined:

$$\eta = \frac{V_{xx} - V_{yy}}{V_{zz}} . \qquad (2.2.21)$$

V_{xx}, V_{yy}, V_{zz} are the components of the electric field gradient along the principal axis. η will be $0 \leq \eta \leq 1$ when we choose axes so that $|V_{xx}| < |V_{yy}| < |V_{zz}|$. $\eta = 0$ represents the axially symmetric case.

In the axially symmetric case, the Hamiltonian is diagonal and the energy eigenvalues are given as :

$$E_m = \hbar\omega_Q\left[3m^2 - I(I+1)\right]. \tag{2.2.22}$$

The m-states are doubly degenerate, which results in (2I+1)/2 different values for the energy. The perturbation factor becomes now

$$G_{kk}(t) = S_{k0} + \sum_{n>0} S_{kn}\cos(n\omega_0 t), \tag{2.2.23}$$

where

$$\omega_0 = 6\omega_Q = \frac{3eQV_{zz}}{2I(2I-1)\hbar}. \tag{2.2.24}$$

In the general non-axially-symmetric case, the interaction Hamiltonian has to be diagonalized. The perturbation factor is of the same form as (2.2.23) with S_{kn} as a function of η and $\eta\ \omega_0$ replaced by $\omega\ n(\eta)$. The transition frequencies obey the relation $\omega_1 + \omega_2 = \omega_3$.

The asymmetry parameter A_2, which will be multiplied by G_2 to present the experimental data A_2G_2, is determined by the symmetry of the lattice.

2.2.5 THE TIME-DEPENDENT PERTURBATION

The charge distribution causing the EFG might change during the lifetime τ of the intermediate state. This means a time dependent perturbation is acting on the system and will affect the intermediate state. The density operator depends now on time. The equation of motion for the density operator can be expressed as :

$$\dot{\rho}(t) = -\frac{i}{\hbar}[H(t), \rho(t)], \tag{2.2.25}$$

The Hamiltonian has a time-dependent and a time-independent part

$$H(t) = K_0 + K(t), \tag{2.2.26}$$

where K_0 is the time-independent part of the Hamiltonian.

The theory for the time-dependent perturbation is complicated. The results of this theory delivers for rapid fluctuations a relaxation of the terms in $G_{kk}(t)$. The S_{kn} terms contain a factor $e^{-\lambda t}$.

3. EXPERIMENTAL ARRANGEMENT

3.1 X-RAY DIFFRACTION MEASUREMENTS

3.1.1 THE X-RAY DIFFRACTOMETER

(GENERAL FEATURES)

The X-ray diffractometer detects X-rays which are reflected from the Bragg planes of a lattice. Under certain circumstances, the reflected X-rays that are scattered by ions located at identical sites in the unit cells of the lattice interfere constructively.

Results of interest of this measurement are the intensity of the detected beam and the diffraction angle 2θ at which the beam is detected. As discussed in the preceeding chapter about theory of X-ray diffraction, a peak in the diffraction pattern occurs whenever the Bragg condition $2d \sin \theta = n\lambda$ is valid.

The X-ray diffractometer is a Philips automated powder diffractometer and consists of an X-ray source, an X-ray monochromator, a slit in the beam path to provide an unidirectional beam, a lead-shielded chamber to house the sample during X-ray exposure and a circularly movable arm which carries the photomultiplier detector.

The whole configuration is mounted coplanar with the swinging arm in the same plane. Figure 3.1 illustrates the schematic arrangement of the spectrometer. The diffractometer is optimized to investigate bulk samples in powder form at room temperature. The applied principle of the measurement is the Debye-Scherrer method.

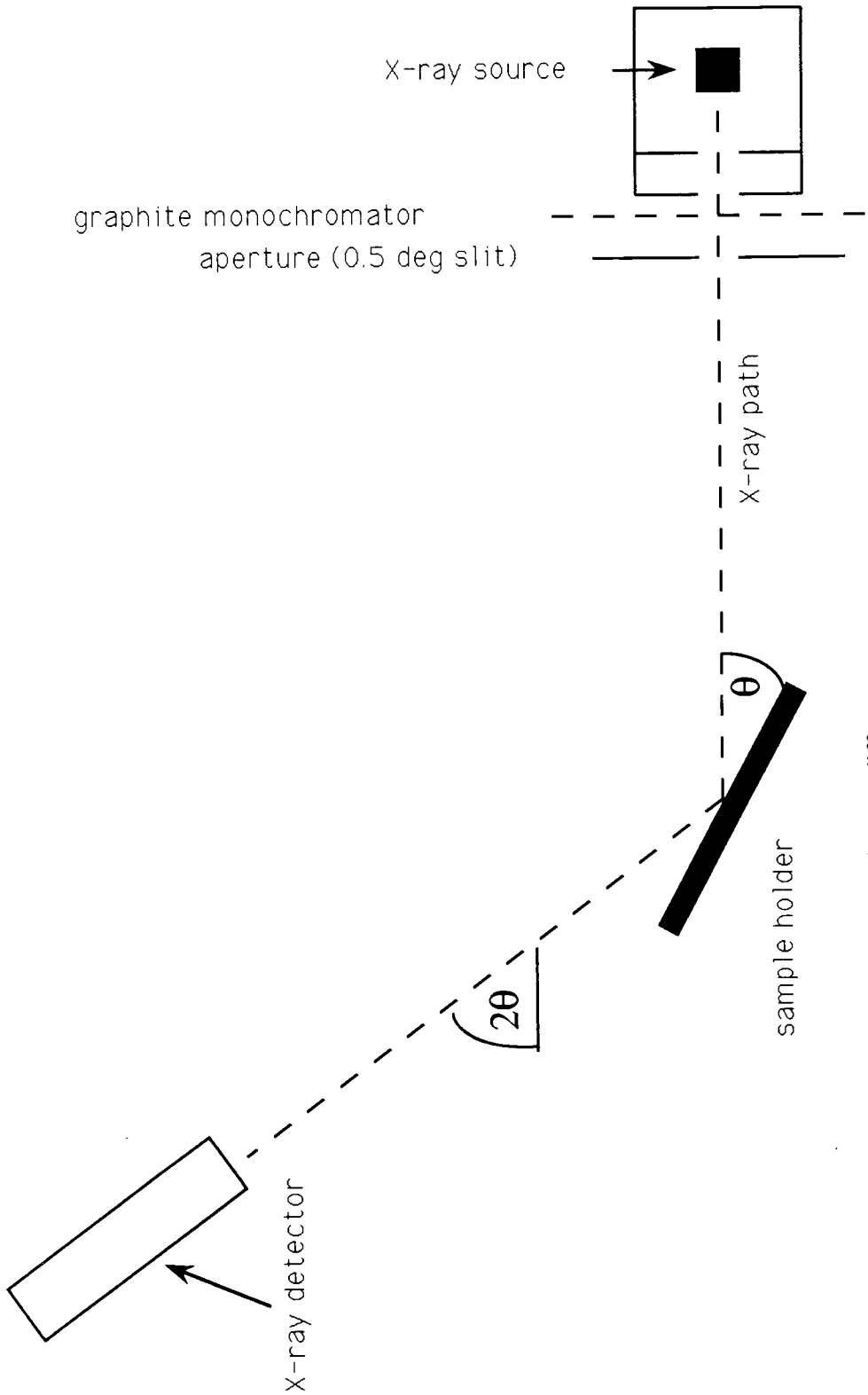

Fig. 3.1 Schematic configuration of X-ray diffractometer

Generally, this configuration produces rings of equal intensity around the emerging beam direction. From each ring, corresponding to an angle with constructive interference, only two points contribute because the detector system is restricted to two dimensions. One of the points, however, has negative angle 2θ and is not physical.

The X-ray source is a Cu Kα source which produces highly monochromatic X-rays with a wavelength of λ = 1.5418 Å. The intensity of the X-ray source is rather strong with about 2000 emission/second in beam direction. The source is operated by 30 kV voltage and 20 mA current. The monochromator from Union Carbide is made out of graphite foil and is mounted in the beam path directly in front of the X-ray source. A slit between the graphite-monochromator and the sample chamber, consisting of two metal plates which are movable with respect to each other, ensures a small cross-section of the beam and its unidirectionality. The slit allows an aperture of $\approx 0.5°$ for the beam.

The sample chamber houses the sample and is the turning point of the swinging arm carrying the photo detector. During a turning process, the arm is moved around an angle 2θ, while the sample holder is turned an angle θ. A piece of lead glass, tightly fitted onto the housing of the sample, allows safe observation of the sample during measurements. The sample is placed into a depression of an aluminum square-shaped sample holder with an edge length of 1". The depression is 1/16" deep and allows X-ray penetration even for very small angles into the bulk sample.

Limits of the swinging arm supporting the X-ray detector are $0° \leq 2\theta \leq 140°$. The detector position can be adjusted to different kinds of X-ray sources, i.e. Co, Ni, etc.. The photomultiplier detects the incident X-rays and amplifies the initial signal.

3.1.2 AUTOMATED DATA PROCESSING

The output of the photomultiplier is transferred to the computer interface where it is read in through the input port into the computer's random access memory (RAM). The data are stored on a 5.25" floppy disc. The software which counts the events stores the intensity and the corresponding value for 2θ in an array of value pairs. These data sets are simultaneously displayed on a monitor as a graph, intensity vs. angle, as the diffraction angle 2θ progresses.

The range of the angles 2θ for measurements of $YBa_2Cu_3O_{7-x}$ was $20° \leq 2\theta \leq 70°$, the d-spacing for Bragg planes ranged from $1.027\ Å \leq d \leq 11.69\ Å$. The upper limit for detection of intensities is 7×10^4 counts.

The software program of the Philips diffractometer system allows the user to choose the scanning limits for the angle 2θ, the scanning step width, the scanning speed and the full scale counts for monitoring the spectrum. After the X-ray scan is finished the spectrum intensity vs. angle can be plotted from the data file.

Another software program enables the user to find the main peaks of the spectrum. The user indicates the minimum limit for the peaks to be found and the estimated background for the spectrum, generated by background radiation and stray radiation scattered from the housing of the device and the aluminum sample holder.

3.2 PERTURBED ANGULAR CORRELATION SPECTROSCOPY

3.2.1 ^{111}Cd AS A PAC TRACER NUCLEUS

^{111}In decays to the excited state of its daughter isotope ^{111}Cd with a half-life of 2.83 d by electron-capture process. This state decays by a cascade of two γ-rays to the ground state of ^{111}Cd. The energies of the two transitions of the cascade are 171 keV and 245 keV. The nuclear spin sequence is $7/2^+ \rightarrow 5/2^+ \rightarrow 1/2^+$. The half-life of the intermediate state is 85 ns. Figure 3.2 illustrates the decay scheme of ^{111}In to ^{111}Cd.

The electron hole in the K shell of the ^{111}Cd decays through X-ray emission and Auger processes. The Auger events will result in a highly ionized probe atom. The recovery time of those highly excited ionic states will critically depend on the availability of free electrons in the surrounding environment of the probe atom.

In semiconductors and insulators, the electronic holes in the outermost shell can persist long enough to introduce an additional perturbation on the angular correlation pattern due to after effects.[38,39] Since this work is concerned with a metal oxide,the after effects will not be considered.

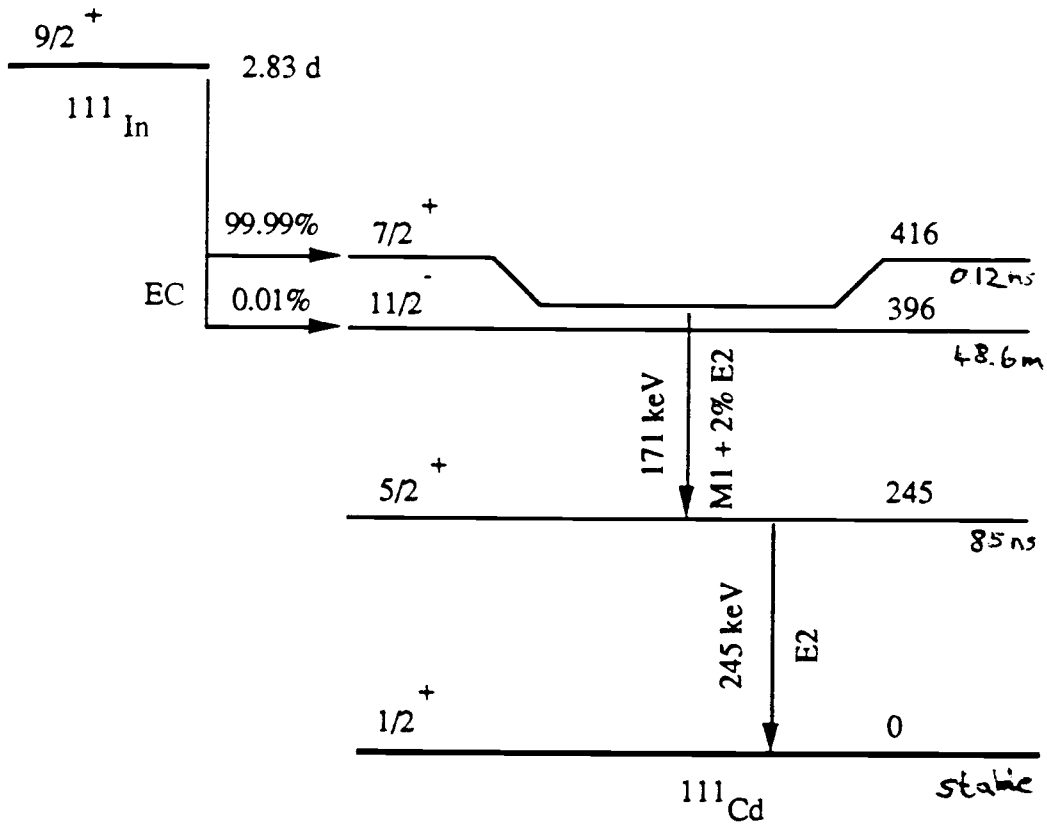

Fig 3.2 Decay scheme of ^{111}Cd as the PAC tracer nucleus

3.2.2 THE PAC SPECTROMETER (GENERAL FEATURES)

The PAC spectrometer detects two γ rays emitted by the tracer nucleus. Interesting characteristics of the γ - γ-cascade are the angular correlation of and the time separation between the two γ-rays.

For these measurements, a time-differential PAC spectrometer with 4 detectors was used with coplanar detector tubes positioned at 90° angles to each other. The spectrometer records the time-dependent number of events in which γ_1 and γ_2 enter two different detectors a time t apart. The time between the two emissions corresponds to the lifetime of the intermediate state of the tracer nucleus. A block diagram of the spectrometer system is displayed in figure 3.3. Each of the detectors provides two output signals for each absorbed photon, which are the time signal of the life-time of the intermediate state from the anode and the energy signal of the γ-ray from the dynode of the photomultiplier.

Immediately after detection of a valid event, a Radio Shack Color Computer, used instead of the popular multi-channel-analyzer (MCA), is interrupted and the digitized time separation of the two γ rays and their routing information is recorded by the interrupt service routine of the operating software and is stored in the memory of the computer. To prevent interrupts of the computer by invalid ADC conversions, a valid-gate in the energy signal processing circuit is inserted. This additional feature reduces the dead time of the spectrometer. The remaining time between interrupts is used to display the raw data on an oscilloscope, and to calculate $A_2G_2(t)$ or its Fourier spectrum. This way, the progress of the experiment is monitored and numerous possible faults in the spectrometer system can be detected during an early stage and can be corrected with a small time loss for the experiment. The data are stored in frequent, regular time intervals on a 5.25" floppy disc to prevent data loss.

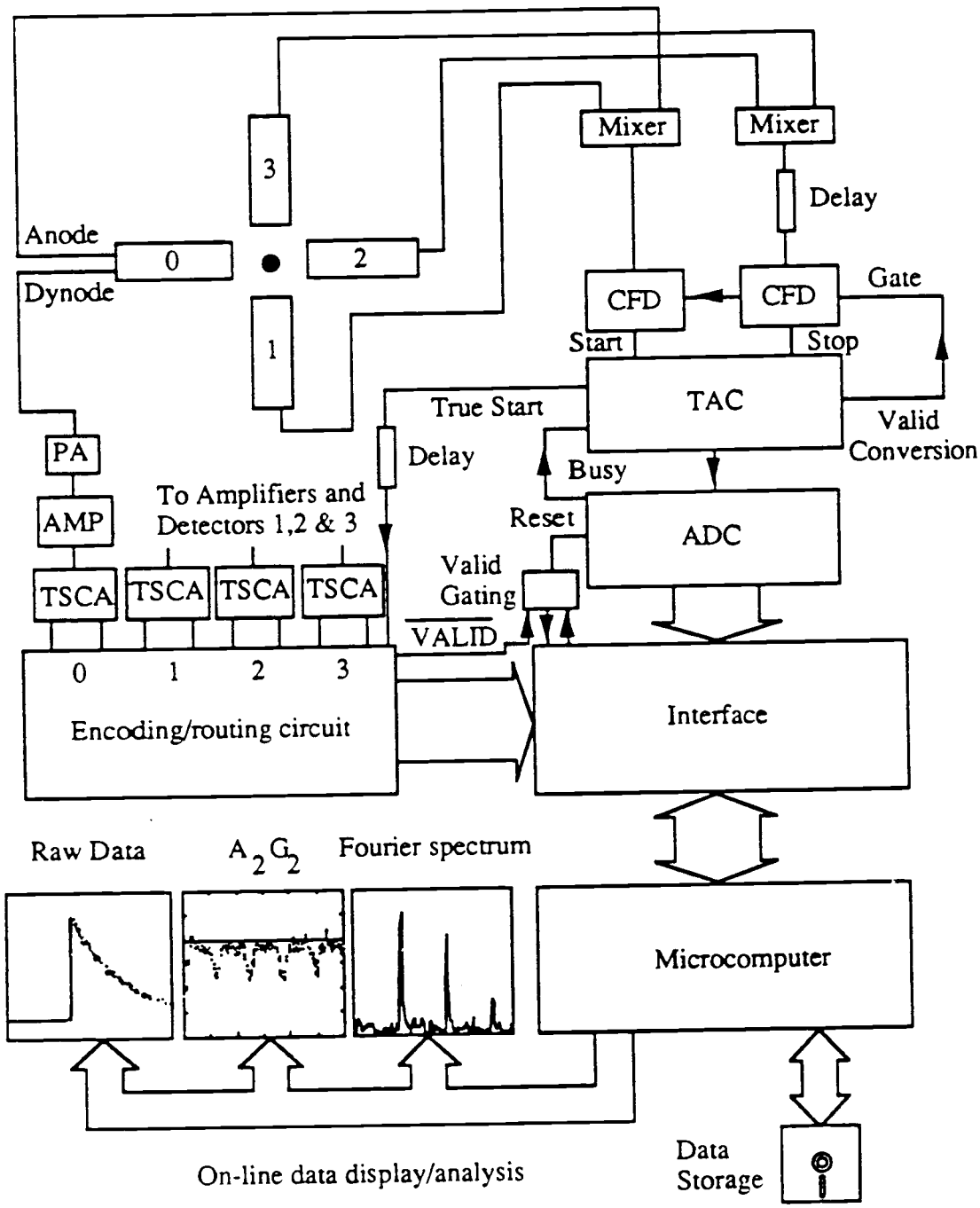

Fig. 3.3 Functional block diagram of PAC spectrometer

3.2.3 THE GAMMA RAY DETECTOR

Each of the four PAC spectrometer γ-ray detectors consists of a 1.5" X 1.5" cylindrical barium fluoride scintillator (BaF_2), which is mounted on a XP 2020Q photomultiplier. The power supplies of the four detectors are independent. An entering photon causes the generation of fluorescence light in the crystal. The intensity of the resulting fluorescent light is proportional to the energy of the incoming photon.

The travelling light wave penetrates into the photomulitiplier tube and hits the photomultiplier cathode where electrons are emitted and then accelerated and multiplied along a series of dynodes. The output signal is taken off the seventh dynode pair of the photomultiplier.

Although NaI and other alkali iodide scintillators have a good energy resolution and are widely used in time-dependent PAC, the BaF_2 crystal is superior for a good time resolution in experiments investigating microscopic properties of solids.

The fluorescence spectrum of BaF_2 shows a fast component in the ultra-violet wave length range at 220 nm which carries $\approx$ 20% of the total fluorescence light intensity and has a decay time constant of 760 ps. The slow component is found at 310 nm wave length with a decay time constant of 620 ns. On the other hand, NaI has a component at 413 nm with a decay time constant of 230 ns. The higher density and, consequently, higher absorption coefficient of BaF_2 is another advantage over NaI scintillators.

In order to increase the light output, the sides and the bevelled edges of the scintillator crystal were covered with Teflon tape. The scintillator and the photomultiplier were connected with silicone coupling fluid with an extremely low absorption coefficient in the interesting wave length range. Magnetic shielding and

aluminum layers were provided to shield the whole system from external magnetic fields and stray light.

A strong steel plate serves as a frame for the arrangement of the detectors which can be moved along tracks pointing towards the sample position while remaining perpendicular to each other.

3.2.4 COINCIDENCE ELECTRONICS

The coincidence electronics are divided into two branches: a fast branch processing the time signal and a slow branch processing the energy signal.

The fast branch consists of four constant fraction discriminator (CFD) modules (AG&G Ortec # 934), one time-to-amplitude-converter (TAC) (EG&G Ortec # 566) and one analog-to-digital-converter (ADC) (EG&G Ortec # 800). At the instant of absorption of a photon, the CFD, which is connected to the anode of the photomultiplier, gives a sharp pulse. The output signals of CFD_0 and CFD_1 are fed into the START input of the TAC. The output signals of CFD_2 and CFD_3 are connected with the STOP input of the TAC. The STOP signal is delayed by a long, co-axial cable to shift the zero for the time scale in the raw data spectrum to mid-range. This cable is inserted before the CFD_0 and CFD_1.

The analog TAC output, which is proportional to the time separation of START and STOP, is digitized by the analog-to-digital-converter (ADC). During the conversion, a BUSY signal gates the TAC off until the conversion is complete. The ADC converts the analog signal to a number between 0 and 1023. This output signal is

fed to the input of the interface and finally to the Color Computer in the case of a valid event.

Because a delay cable is used, a prompt event, i.e. simultaneous detection of γ_1 and γ_2, is recorded near midrange of the oscilloscope.

The energy signal processing is accomplished by the slow branch. The energy pulses from the seventh dynode of the photomultiplier are shaped and amplified by a preamplifier (EG&G Ortec #113) and an amplifier (Tennelec model TC 211). The output of the amplifier is a bipolar signal with amplitude proportional to the energy of the absorbed photon.

This signal is fed into the twin-single-channel-analyzer (TSCA). If the signals of γ_1 and γ_2 are within an "energy window", which is limited by the Lower Limit Threshold (LLT) and the Upper Limit Threshold (ULT), then the decay event is considered valid, the signals of γ_1 and γ_2 are sent from the output of the TSCA onto the input of the routing circuit for determination of the sequence of the two γ quanta, and the gate to the ADC output signal is opened to be fed into the memory of the CoCo.

A valid "normal" event is recorded if a TSCA of detector 0 or detector 1 shows absorption of γ_1 and detector 2 or detector 3 absorption of γ_2. A valid "reverse" event is represented by detection of γ_1 in scintillation detector 2 or detector 3 and detection of γ_2 by detector 0 or detector 1. The information about the sequence of the γ - γ cascade is the routing information.

3.2.5 ROUTING ELECTRONICS AND COMPUTER INTERFACE

The computer interface consists of a peripheral interface adapter chip (PIA). The chip is connected to the Color Computer by a bus expansion box. The routing circuit restricts the number of START and STOP pulses from the TSCA to one. In the case of one γ_1 and one γ_2 input being high, the energy event is considered valid and the Valid Gating Circuit sets the corresponding bit on the Interface chip high. The computer is interrupted and the output signal of the ADC is transmitted via the interface to the computer memory. The Valid Gating circuit reduces the dead time of the spectrometer by a factor of three and is very useful for measurements with strongly radioactive samples.

A TRUE START signal from the TAC is fed into the Routing circuit in order to correlate the processing of the time signal in the fast branch with the energy signal in the slow branch. This signal is delayed by 2 μs .

As soon as the ADC conversion is completed, the ADC generates a DATA READY pulse and releases simultaneously the digitized signal to the input of the PIA.

3.2.6 OPERATING SOFTWARE

Most parts of the spectrometer operating software are written in BASIC. The time-critical parts, however, like the interrupt service routine are written in machine language. This keeps the time period of computer interruption and therefore the dead time of the spectrometer small.

After the PIA output is read, the ADC is reset and the next interrupt can occur while the computer is still processing the data of the previous event. Registered data to be processed are temporarily stored on a stack.

The interrupt service routine examines the VALID signal and returns immediately from the interrupt if the event is invalid. In the case of a valid event, the processed ADC output signal is fed into the computer's random access memory (RAM) which is divided into 16 sectors corresponding to 16 theoretically possible detector pairs detecting γ_1 and γ_2. Each sector consists of 512 channels. The routing information identifies the memory sector while the ADC output signal designates the offset of a particular event in that sector. The channel with time-zero of each sector is in the mid-range of the TAC (channel 256). Therefore, besides the "normal" spectrum of the raw data for sectors 0/2, 0/3, 1/2 and 1/3, "reverse" spectra for sectors 2/0, 3/0, 2/1 and 3/1 can be accumulated.

Between the interruptions, the computer displays counts vs. time for each sector on the oscilloscope, determines the accidental coincidence count rates and computes true count rates. It can calculate the perturbation function and the Fourier spectrum and display them on monitors.

A typical run lasts 8 to 24 hours to accumulate two statistically independent spectra ("reverse" and "normal"). Finally, the data from the sectors of the RAM are saved on a 5.25" floppy disk for further processing and analysing.

3.2.7 SPECTROMETER CALIBRATION

To provide the detection of photons with the right energy, LLT and ULT of the energy "windows" in the window comparators have to be calibrated and in frequent,

regular intervals adjusted. This task is performed by a MCA with the sample situated in the furnace at the place of the actual measurement.

Fig. 3.4 shows the typical energy spectrum of the $^{111}In/^{111}Cd$ tracer. Three energy peaks can be seen in the spectrum: The highest energy peak is due to the 245 keV γ decay from the 5/2 to the 1/2 nuclear state of the cadmium nucleus. On the left of this peak is the 171 keV peak due to the 7/2 to 5/2 nuclear state transition.

A group of two peaks is found at very low frequencies due to X-radiation. The one with the lower energy at 23 keV is generated by the K X-ray during the ^{111}In to ^{111}Cd electron capture process. A second X-ray peak at 32 keV is caused by the photo-electric effect of Ba in BaF_2 of the scintillator. By use of the MCA, the energy windows of the TSCA are set in a way that their centers are at 171 keV for detection of γ_1 and at 245 keV for detection of γ_2.

After the calibration of the energy windows, the time has to be calibrated. This contains:

a) the adjustment of the cable lengths in the fast branch such that the time-zero channels for all memory sectors are the same

b) the determination of the time scale on the TAC

c) the determination of the time resolution of the spectrometer.

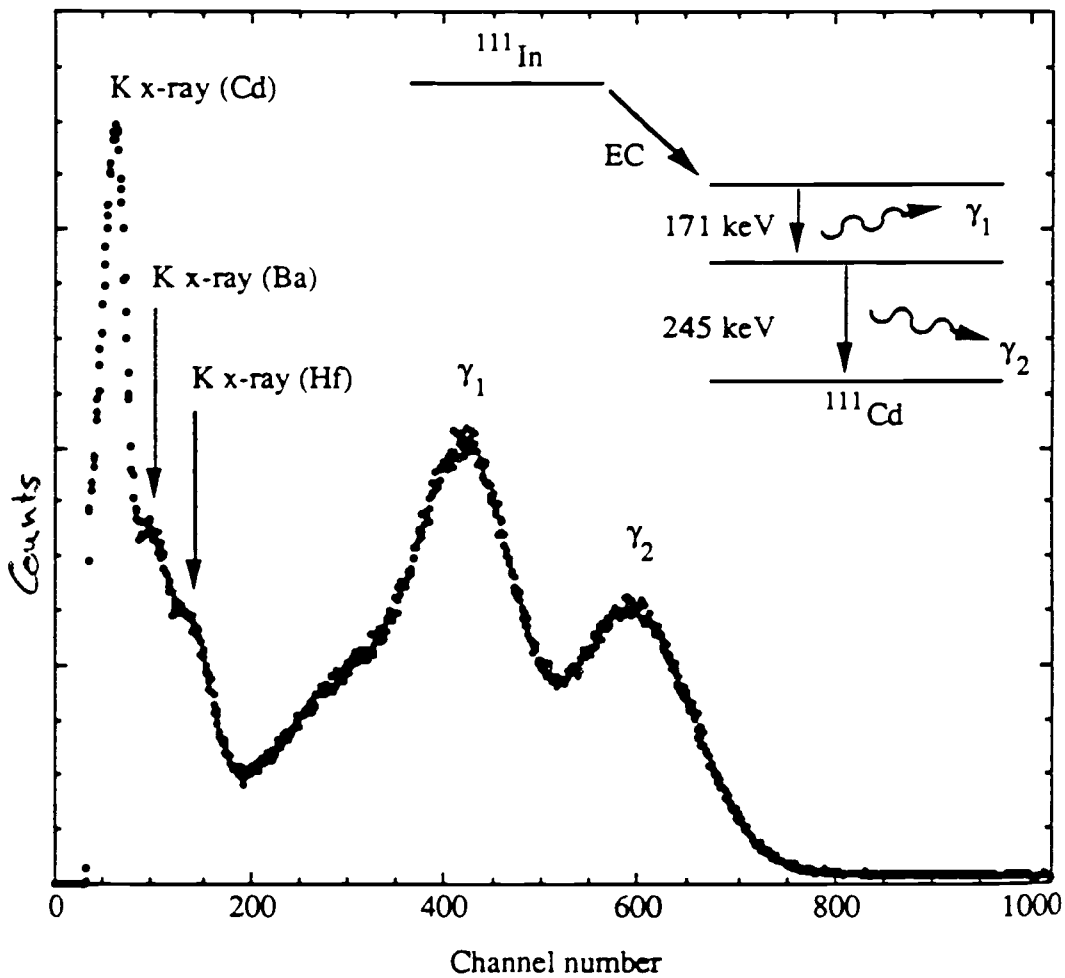

Fig 3.4 Energy spectrum of ^{111}In using a BaF_2 scintillator detector

The time-zero alignment is performed by the use of a ^{22}Na source. The β^+ transition to its daughter isotope ^{22}Ne generates two γ-rays, both with 511 keV energy, after the positron annihilates with a shell electron. These rays are emitted into opposite directions and can be detected by two opposing X-ray detectors if their emission is co-directional with the detector tube. Hence, a prompt spectrum can be accumulated in the corresponding memory sector. This spectrum normally, instead of having ideal shape, shows a Gaussian distribution of counts vs. energy due to a finite time resolution of the spectrometer. The adjustment can now be performed by variation of the decay cable lenght between mixers and CFD's.

The absolute time scale of the TAC is determined with the help of a time calibrator (EG&G Ortec # 462). START and STOP pulses separated by arbitrary time intervals are generated and connected to the input of the TAC. Now a calibration program accumulates the periodic repeating peaks and calculates the time calibration by a least squares fit. The result delivers an absolute time calibration of 1.89 ns/channel.

The instrumental resolution function can now be calculated by using the location and full width at half maximum (FWHM) of every prompt peak. The resolution function determines the finite time resolution of the system. The overall time resolution of the spectrometer was determined to be ≈ 1.9 ns.

Time-zero channel, time calibration, and instrumental resolution function are stored in the computer's memory and saved with experimental spectra to a floppy disk for reference during analysis of spectra.

3.2.8 THE SPECTROMETER'S FURNACE

Because of the special interest in the high temperature regime of the sampled material, the furnace is a crucial part of the spectrometer. It serves as the housing of the sample and is the centerpiece of the spectrometer system.

Certain requirements of the furnace design regarding the suitability for the experiment and characteristics of the sample must be considered. Hence, the horizontal dimensions should be as small as possible to allow the photomultipliers to be as close as possible to the sample.

The outer surfaces of the device should be at room temperature during the measurement, independent of the sample temperature to provide equal conditions for the photomultiplier at different temperatures.

Furthermore, in order to keep the absorption of γ-rays low, the furnace housing should consist of a thin material with a low scattering coefficient, i.e. low atomic number. Also, the material has to be chosen in a way that it sustains temperatures of up to 1100° C.

The furnace consists of an alumina furnace tube (McDanel Refractory Co. # 998), being closed at one end with an inner diameter of 3/8", an outside diameter of 1/2" and 5" long.

The heating element is graphite foil of 5/1000" thickness. Wrapped around the furnace tube, the heating element is covered with one layer of alumina thermal insulation and two layers of 1/1000" thick zirconium foil. The zirconium foil provides heat shielding and prevents the graphite foil from oxidation by attraction of effused oxygen ions at high temperatures. Current leads consist of two pieces of copper foil of 10/1000" thickness.

Mounted in the aluminum housing with internal water cooling, the heating unit is supplied by AC power. The temperature is detected by a Pt-Pt/10%Rh thermocouple, placed in the center of the furnace tube, and converted in order to serve as a temperature indicator. The thermocouple is connected to the temperature controller (Barber Colman # 522D).

The open end of the alumina furnace tube is exposed to atmospheric pressure. A vacuum provided by a mechanical vacuum pump is applied to the closed space housing the heating element to prevent the graphite foil from oxidizing. The temperature distribution is axially symmetric about the tube axis.

4. SAMPLE PROCESSING

4.1 SAMPLE PREPARATION

During this work, samples of pure, generic $YBa_2Cu_3O_{7-x}$ and ^{111}In-doped $YBa_2Cu_3O_{7-x}$ were used. All of these samples were prepared and processed in our laboratory.

Commonly, the solid state method for processing high T_c superconductors $YBa_2Cu_3O_{7-x}$ makes use of a mixture of Y_2O_3, $BaCO_3$, and CuO in powder form which is synthesized at 900° C for 24 hours and finally annealed by slow cooling.

Our laboratory, however, developed, in cooperation with Dr. James A. Sommers from Teledyne Wah Chang Albany, a different method for sample processing, starting out with a solution of nitrates.

4.1.1 SAMPLES FOR X-RAY DIFFRACTION

For the X-ray work, three sets of samples were processed and used for later measurements. One set consisted of 5 samples, each containing different doping concentrations of In as a substitute for Y. The concentrations of the doping probe were 0%, 5%, 10%, 15% and 20% of In for the first and second set and 0%, 1%, 2%, 5% and 10% of In for the third set. In the first set of samples, In was simply added to the mixture of nitrates. For the second and third set, In was actually substituted for Y, i.e. for a sample containing 5 at% In, 5 at% of Y was removed, etc.. The actual chemical compositions are then

$$(In_yY_{1-y})Ba_2Cu_3O_{7-x} \quad ,$$

where y indicates the fraction of In concentration.

The purpose of the sample processing was the even distribution of the ingredients In, Y, Ba and Cu within the bulk before the synthesis of the superconducting sample in the calcination process.

The even distribution was accomplished by

- a thorough mixing of all initial ingredients being present in the clear solution
- maintaining this homogeneity while the solution was being evaporated by heating. This was aided by constant stirring
- combustion of the homogeneity-maintaining agent, i.e. the cellulose after evaporation of the solutions.

The following procedure is concerned with pure $YBa_2Cu_3O_{7-x}$ (i.e. 0% In). For samples with higher concentrations, the procedure is exactly the same, except that the corresponding molar concentration is substituted for Y. At the end of this procedure, it was assumed that the correct ion ratio of Y, Ba, and Cu (= 1:2:3) is present in every grain of the bulk.

As opposed to the solid state method of sample preparation with its mixture of powders, the nitrate evaporation method makes use of a carefully prepared, stoichiometrically accurate mixture of the following nitrates in solution:

- $Y(NO_3)_3 \cdot 6H_2O$
- $Ba(NO_3)_2$
- $Cu(NO_3)_2 \cdot xH_2O$ (x~2.5).

The aqueous solutions of the nitrates solutions were mixed in a way that the ion ratio was 1Y : 2Ba : 3Cu. The color of the solutions was blue and the concentration

was 3.0 g / 70 ml. Every set of samples was made from the same parent solution. For the X-ray work, the typical size of the final sample was 500 mg. This corresponded to 8 ml of nitrate solution of the above molar concentration as an initial amount.

The solution was dripped carefully onto ashless analytical filter tablets or ashless analytical filter paper (Schleicher & Scheull, Pulp, model # 289) placed on a pan-shaped alumina lab casserole of 5" diameter and 3" depth (Coors model # 60062). The filter material consisted of cellulose.

After the solution was absorbed, the blue, wet pellet was crushed and the resulting paste was gently heated with continual stirring. To obtain smooth heating, an electrical hot plate was used instead of a Bunsen burner. A homogeneous heat distribution in the paste was accomplished by continual stirring and grinding with a metal sample spatula.

After 5 minutes, the water of the solution began to evaporate from the aqueous solution. After this process, the result was a dry blue powder. After 10 to 15 minutes, the color of the paste changed to turquoise and later light-green. The nitrates were lost during this process. If portions of the sample heated up to high, a green flame as a product of the oxidation of copper may occur. After 20 to 25 minutes, the carbon of the cellulose material began to char (dehydrate) and the green pieces of the filter material started turning dark-brown.

The cellulose began to burn and the color turned from dark-brown to black. This burning process normally took place without flames. The edges of the green pulp pieces started first to turn red and the glowing progressed towards the inner part of the sample. After about 30 to 35 minutes, all the carbon had burnt away and the remaining, black powder had decreased substantially in volume.

After a final grinding the grain size ranged from 10 - 50 μm and was very unifom .

4.1.2 SAMPLES FOR PAC EXPERIMENTS

As a radioactive tracer ^{111}In was used. The In isotope has a half-life of 2.83 d. The crucial part of sample preparation for PAC samples is the introduction of the radioactive probe. This was carried out by adding In isotope to the sample in the beginning of the processing.

The isotope from DuPont/New England Nuclear was diluted by ten drops of hydrochloric acid (HCl). One drop of the fresh, diluted isotope was sufficient to provide an activity of 6×10^4 counts/ minute for the PAC sample which was still active enough for a PAC measurement after a calcination process of 1.5 d. The amount of added In isotope had a concentration of 10^{-8} of the Y atoms.

After processing a series of samples, it was recently established that the age of the radioactive isotope influences the quality of the sample. As a consequence of the short half-life of 2.83 d and the rapid, exponential decrease of radioactivity, a larger amount of In isotope had to be added to obtain the same radioactivity in the sample.

This fact will later be discussed in chapter 6.2.1:Sample processing induced variations in PAC measurements. The following steps were identical to those applied for the X-ray samples, i.e. absorption in the filter material, heating the sample, oxidation of the carbon, stirring and grinding. Besides the radioactive In isotope, most of the PAC samples still contained the non-radioactive In in different concentration, i.e. the samples still had the form $(In_yY_{1-y})Ba_2Cu_3O_{7-x}$ and the extra added ^{111}In.

4.2 SYNTHESIS OF THE SAMPLE BY CALCINATION

In order to promote the chemical reaction of the oxides of Y, Ba, and Cu, the sample has to be calcined (fired) at a temperature between 940° C and 950° C. The sample is formed as the oxygen deficient pseudo-tetragonal phase of the superconductor $YBa_2Cu_3O_{7-x}$. Slow annealing which allows re-oxidation is required in order to obtain a good superconductor.

There is partial melting at 975° C. To avoid this, the calcination temperature should always be well below this mark.

For the firing process, a resistive vertical tube furnace was used which consisted of a cylindrical ceramic heating element and a supportive housing containing insulating material. The furnace tube could be rotated around an axis perpendicular to the tube axis. The heating elements were controlled by an OMEGA Temperature Controller System using a Platinum - Platinum/10% Rhodium thermocouple as a temperature indicator. The thermal output voltage of the thermocouple was read by a voltmeter and finally converted to temperature with the help of a standardized conversion table.

Different atmospheres were applied to the sample during calcination. The original idea was to provide as much oxygen as possible during this process, and especially during the cooling. It turned out, that in air atmosphere, the sample formed more readily. The air flow was accomplished by convection through the tilted tube furnace. An angle of about 15° to 20° between the tube axis and the horizontal ensured a sufficient air flow.

The bulk samples were dark-grey powders and were placed on sample holders, which were made of Coors alumina tubes of 0.5" diameter and 1" length. A third of the circular cross-section had been taken off by a diamond saw, so that the sample was exposed to the atmosphere.

The sample holders were placed in the center of the furnace next to the end of the thermocouple were the temperature gradient was assumed to vanish or at least to be small. For each In concentration a different sample holder was used to prevent contamination of the sample by sample portions with different In concentrations.

Before use, the sample holders were prefired with the corresponding sample at temperatures up to 1050° C to initiate a heavy reaction of the sample with the sample holder. Thus, it was ensured that a later sample would not react with Al_2O_3 of the sample holder.

Typical calcinations at 950° C lasted 12 to 24 hours, the cooling periods between 18 and 36 hours. The cooling rate was 40° C/hour.

At a temperature of about 400° C, the power supply of the furnace was shut off and the sample cooled at the natural cooling rate of the furnace. As a consequence, the sample was mostly in equilibrium with the atmosphere. After the sample was cooled and then removed from the furnace, the powder appeared to be sintered to a solid piece which could easily be crushed and ground with a mortar and pestle.

The samples were stored in an oxygen atmosphere before and after the experiment to prevent possible adverse effects of air moisture.

4.3 PHASES INVOLVED DURING THE SYNTHESIS OF $YBa_2Cu_3O_{7-x}$

A complete phase diagram with compatibility regions for the possible compounds evolving during the processing of $YBa_2Cu_3O_{7-x}$ is shown in figure 4.1 below.[40]

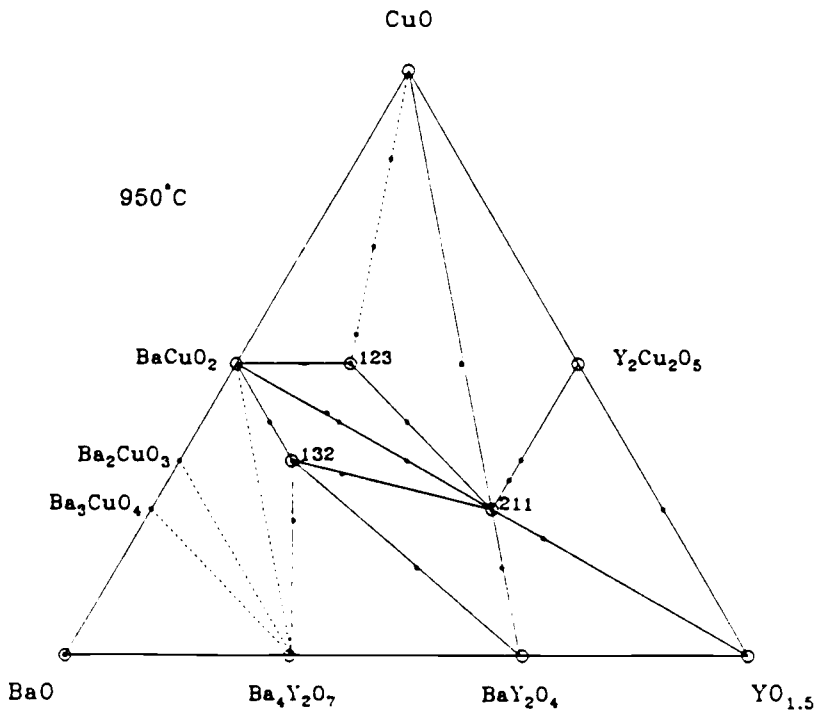

Fig. 4.1 Compatibility regions in pseudoternary Y_2O_3-BaO-CuO at 950°C; compositions used to confirm the existence of the tie lines shown are indicated by the black dots.

This phase diagram is important for the evaluation of the X-ray spectra because it gives a complete list of secondary phases which evolve either by deficiencies of the initial ions, inhomogeneities within the bulk sample or incomplete calcination. Indeed, in the progression of this work, it turned out that several of these secondary phases were detected.

5. DATA ANALYSIS AND DATA REDUCTION

5.1 ANALYSIS OF X-RAY DIFFRACTION DATA

The data intensity vs. angle of the X-ray powder diffraction measurements are stored on a 5.25" floppy disc and the entire evaluation of the data was performed on an Apple Macintosh II Computer. The data were transferred from the 5.25" floppy disc onto a 3.5" disc or the internal hard disc of the Mac by a resident program, called the "Apple file exchange".

5.1.1 Si AS STANDARD REFERENCE MATERIAL

Since the spectra of the diffractographs have calibration errors in the angle 2θ, the error is compensated with the help of the Standard Reference Material (SRM) 640b from the National Bueau of Standards in Gaithersburg, MD, that is a silicon powder mixed with the sample.

The calibration is accomplished by shifting the values for 2θ by the difference between the theoretical peak positions for the SRM 640b and the experimental position. This provides comparability of spectra from different measurements.

The crystalline powder of Si 640b has a monatomic, cubic lattice structure and the lattice parameter is a = 5.43094 Å. The grain size is extremely small (~ 5 μm) and the variation in lattice parameter and grain size is very little (less the 0.05 %). Thus, the peak positions can be exactly determined. A table of the complete set of peaks and an X-ray pattern for SRM 640b are shown below.[41]

hkl	I^{rel} Sided Drifted[5]	I^{rel} Front Loaded ≠	2θ peak
111	100	100	28.442°
220	55	64	47.303
311	30	34	56.122
400	6	8	69.130
331	11	12	76.376
422	12	16	88.030
511/333	6	8	94.953°
440	3	5	106.709
531	7	9	114.092
620	8	7	127.545
533	3	3	136.893

Table 5.1 Miller indices, diffraction angles, and relative intensities of SRM 640b

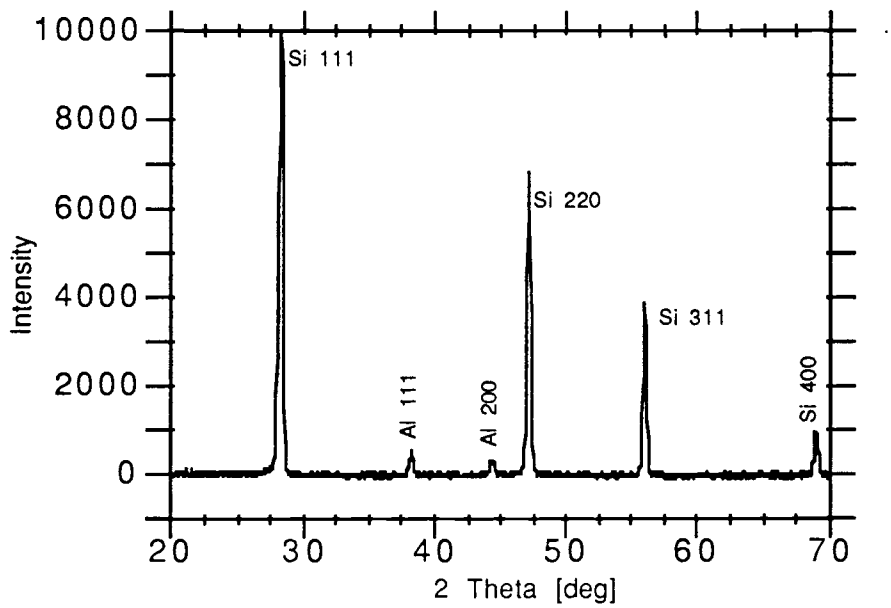

Fig. 5.1 X-ray pattern of SRM 640b Si on Aluminum sample holder

The amount of Si which was added to the sample was about 5% of the sample volume, resulting in a superposition of the diffraction patterns of $YBa_2Cu_3O_{7-x}$ with Si .

5.1.2 EVALUATION OF X-RAY DATA

After these preliminary adjustments, the actual identification of the spectrum began. The Joint Commitee of Powder Diffraction Spectra (JCPDS) publishes and updates a complete catalog of powder diffraction patterns for all existing, stable, chemical compounds. For each of the compounds a table showing Bragg spacing d, relative intensity and Miller indices is displayed on a catalog card. Other interesting features of the sample like sample preparation procedures, the type of radiation used for the diffraction, the lattice space group and color of the sample are also indicated on the card.

A list of all detectable peaks in the spectrum was made, indicating the intensity of Bragg peaks at angle 2θ. The peaks were matched with peaks from the JCPDS card and then labeled in a proper way.[42] Furthermore, all peaks not identified with the $YBa_2Cu_3O_{7-x}$ were identified as belonging to known secondary phases.

Non-physical peaks could be caused by voltage sparks of the X-ray source, reflection from mechanical impurities like dust, reflection from a possible superlattice, by a non-uniform grain size, or by the existence of secondary phases.

The interesting peaks of the major phase ($YBa_2Cu_3O_{7-x}$) could subsequently be evaluated quantitatively. Both coordinates, intensity and angle 2θ have been investigated. The intensity of a Bragg peak is proportional to the integral over the peak. The integration was performed from background level to background level and included typically 0.4° to 0.5° angular spread. For the integration, a software program was written in Lightspeed Pascal which is displayed below:

```
program peakint;

    var
        i: integer;
        x: array[1..4000] of real;
        y: array[1..4000] of real;
        z1, z2, s: real;
        f: text;
        a: string;

begin{peakint}

    writeln('This program calculates intensities by integration over peaks.');
    writeln;
    writeln('Which file do you want to use?');
    readln(a);
    filename := concat('X-ray/GW 3:a');
    open(f, a);

    for i := 1 to 5 do
        begin
            readln(f);
        end;

    for i := 1 to 4504 do
        begin
            read(f, y[i]);
            readln(f, x[i]);
        end;

    writeln('Give the lower limit of integreation:');
    readln(z1);
    writeln;

    writeln('Give the upper limit of integration:');
```

```
        readln(z2);
        writeln;


        i := 0;

        repeat
                i := i + 1;
        until x[i] = z1;

        s := 0;
        i := i - 1;

        repeat
                i := i + 1;
                s := s + y[i];
        until x[i] = z2;
        close(f);

        writeln('The integral over the intensities between the given boundaries is', s : 10
                        : 2, ' counts');

end.
```

The background for the 1-2-3 spectrum was calculated by integration over the spectrograph between $2\theta = 25°$ and $2\theta = 27°$. For these angles neither the major phase 1-2-3 nor secondary phases could be detected by Bragg peaks. The integral was devided by the number of channels (200) to obtain a value for the background /channel.

Sample volume, geometrical arrangement of the sample holder, partial volume of the SRM 640b and grain size determine the total peak intensity. In order to obtain an intensity value for Bragg peaks independend of these parameters, the integral over the peaks were normalized.

The second step of the integration method consisted mainly of the integration of the normalization peak of the 1-2-3 spectrum. The peak with Miler indices 116 was chosen because this peak was isolated from other peaks except the peak with Miller indices 213. For future reference, a peak will be indicated just by its Miller indices.

There is an angle-dependence of Bragg intensities. However, the dependence is constant for all measurements within one set of samples.

Based on a calculation of the structure factors for both of these peaks, no significant change in intensity for the 116 and the 213 peaks were expected with respect to In doping. This characteristic made the 116 peak extremely suitable as a norm peak. The integration limits were taken between 2θ values of intensity equal to the lowest intensity at the overlap of the 116 peak with the 213 peak.

Subsequently, the peaks of the major phase could be integrated from background level to background level. Again the background was subtracted. The peaks of interest were the 012, 102, 112, 003, 005, and 006 during the first stage of the work. Originally, these peaks were chosen because the theoretical calculation of the intensities showed a strong relative change with respect to the In concentration. The absolute intensity was big enough to measure a change in it.

Unfortunately, it turned out, that most of these peaks interferred either with the Si spectrum of the SRM 640b, with the aluminum spectrum of the sample holder, with secondary pases or with other peaks from the major phase. For later measurements, only the 003 peak which was the only non-interferring peak was used for evaluation.

As a final step, the peaks were normalized by the intensity of the 116 peak. The resulting relative intensities were tabled as a function of In.

5.2 REDUCTION OF PAC DATA

At the end of the PAC measurement, the data are saved on a 5.25" floppy disc and subsequently read into an IBM XT personal computer. The average background is

calculated by a software program for each sector, i.e. each pair of detectors and the data are checked with respect to a possible data overflow.

The four-spectra-ratio of the normal spectrum is defined by

$$R_n(t) = 2\frac{(C_{02}C_{13})^{1/2} - (C_{03}C_{12})^{1/2}}{(C_{02}C_{13})^{1/2} + 2(C_{03}C_{02})^{1/2}} \tag{5.1}$$

and for the reverse spectrum

$$R_r(t) = 2\frac{(C_{20}C_{31})^{1/2} - (C_{30}C_{21})^{1/2}}{(C_{20}C_{31})^{1/2} + 2(C_{30}C_{21})^{1/2}}. \tag{5.2}$$

The C_{ij} are the background corrected coincidence counts in memory sector i/j:

$$C_{ij}(\theta, t) = D_{ij} - B_{ij} = \frac{1}{\tau_N} e^{-\frac{t}{\tau_N}} e_i e_j N_0 W(\theta, t) \tag{5.3}$$

The detectors are arranged in a way that #0 and #2 include an angle of 180°, #0 and #3 90°, and so on. e_i, e_j are the detector's single efficiencies. N_0 is the decay rate for the parent isotope ^{111}In and τ_n is the lifetime of the intermediate state (τ_n = 85 ns). W(θ,t) is the angular correlation function

$$W(\theta, t) = 1 + A_2 G_2(t) P_2(\cos\theta). \tag{5.4}$$

This formula is derived from formula (2.2.9). $A_{44} \approx 0$ and A_{22} is expressed as A_2 by convention. The $A_2G_2(t)$ spectra for the normal and the reverse raw data spectra were calculated and saved.

5.2.1 DATA ANALYSIS

The fast Fourier Transform of the A2G2(t) function is important and gives information about the PAC measurement that is easy to interpret. The Fourier transform indicates the frequencies of a substitutional site and possibly information about the sites of substitution for simple crystal structures. The fast Fourier transform application multiplies the time-domain data by a time-domain window to reduce the spurious peaks in the Fourier spectrum due to the finite length of the time spectra .

A non-linear least squares fitting routine based on Marquard's algorithm was used to fit the experimentally obtained $A_2G_2(t)$ function. The finite instrumental resolution of the spectrometer was taken into account by the system time resolution function and the distribution of the EFG was taken into account by a Lorentzian distribution. Both of the above fitting functions were convoluted with the theoretical expression for the $A_2G_2(t)$ function.

A successful, physically meaningful fit is based on the right choice of the fitting parameters during the fitting procedure. The fitted function gives several other physically important parameters related to the material:

The observed effective anisotropy A_2^{eff} is the anisotropy factor A_2 reduced by a solid angle correction factor. The PAC frequencies ω_1 and ω_2 depend on the asymmetry of the EFG and the strength of the interaction between the nuclear quadrupole moment and the EFG.

The relaxation constant λ indicates the relaxation rate of the probe nuclei due to fluctuating EFG fields.

The fractional weight of the ith site of the sample f_i.

The relative distribution of the EFG, δ, gives a measure of the quality of the sample.

The asymmetry parameter η and the electric field gradient magnitude V_{zz} can be derived from the above parameters. η, which is derived from the electric field gradients, is related to the crystal symmetry of the probe environment:

$$\eta = \frac{V_{xx} - V_{yy}}{V_{zz}} \qquad (5.5).$$

For the axially symmetric case, $\eta = 0$. For lower symmetrries, $0 < \eta \leq 1$. The electric field gradient magnitude V_{zz} can be expressed as the sum of lattice part due to the contribution of the ionic cores of nearby atoms, and an electronic part which arises from the influence of covalence bonds, conduction electrons and unfilled electronic shells of the probe atom.

6. EXPERIMENTAL RESULTS

The purpose of the experiments undertaken was the quantitative investigation of physical properties of the superconductor $YBa_2Cu_3O_{7-x}$ due to the doping with In. Of special interest was the solubility limit for the dopant and the site of substitution.

Research projects and established results from other research groups indicated that the In atoms are largely dissolved in bulk and are not strongly concentrated in some minor precipitate or grain-boundary phase.

Under the assumption that all of the added amount of In substitutes uniquely at the Y, Ba, Cu(1) or Cu(2) site of the major, orthorhombic phase, it is expected that the structure factors correlated with Bragg planes containing the dopant will change continuously due to the change of the scattering factor.

Since the electron configurations of the doped cation are different from the substituted ions Y, Ba and Cu, there will be different interaction potentials within the lattice. A change in Bragg spacing d may result as a consequence.

A different ionic radius and cross section of In causes a different atomic form factor and intensities for all peaks which are generated by scattering of the X-rays at Bragg planes containing In.

Table 6.1 shows the electron configuration, the ionic radii, and the oxidation states for In, Y, Ba and Cu.[43]

	electr. conf.	ionic radius	oxid. state
^{111}In	4d10 5s2 5p1	0.81 Å	+ 3
^{89}Y	4d1 5s2	0.893 Å	+ 3
^{136}Ba	4d10 5p6	1.34 Å	+ 2
^{63}Cu (1)	3d10 4s1	0.72 Å	+ 2
^{63}Cu (2)	3d10 4s1	0.96 Å	+ 1

Table 6.1 Electron configurations, ionic radii, and oxidation states

Many speculations have been made about the substitutional site of In. None has been proven. Possible substitutional sites for the In ion are the Y, Ba, Cu(1), and the Cu(2) site. The similarity in the electronic radii and the equivalence of the oxidation states suggest a substitution at the Y site. The substitution at the Ba site is ruled out based on the consideration of valency and ionic radius.

Both, the global probe X-ray work and the local probe PAC experiments, were applied for the investigation. In addition, data and evaluations of Meissner flux exclusion experiments, taken at Ames Laboratories by Dr. Douglas Finnemore, will be presented in Chapter 6.3: Magnetic flux exclusion measurements..

6.1 X-RAY DIFFRACTION MEASUREMENTS

X-ray diffraction measurements were used to identify compounds and to investigate the Bragg spacings d and the intensities of Bragg peaks, especially as a function of the concentration of doped In.

Several samples with different amounts of In were prepared as diluted nitrate solutions ($In(NO_3)_3$, $Y(NO_3)_3$, $Ba(NO_3)_2$, $Cu(NO_3)_2$) in the way described in Chapter 4.

For each group, 5 samples with different doping levels were prepared. One group of those samples will be called a set. Overall, three sets of samples were made and investigated by different methods.

During the early stage of the work, $In(NO_3)_3$ was simply added to a mixture of Y, Ba, and Cu nitrate solutions with the cation ratio 1Y: 2Ba: 3Cu. Assuming a substitution of In in the 1-2-3 material, it is expected that the ion ratio in this mixture will be distorted.

Two later sets were prepared in a different way: The amount of $Y(NO_3)_3$ in the mixture was decreased in a way that the molar weight of added $In(NO_3)_3$ was equal to the molar weight of removed $Y(NO_3)_3$. In other words, instead of adding excess In nitrate, a mixture of In, Ba and Cu nitrate was added. The following mixing ratio was obtained: 1(In + Y) : 2Ba : 3Cu .

The second set of samples contained non-negligible amounts of secondary phases that caused difficulties for the exact evaluation of the data (see chapter 6.1.2.1). Therefore, a third set of samples was prepared, which showed a significantly higher quality with lower amounts of secondary phases.

X-ray diffractographs were taken for $YBa_2Cu_3O_{7-x}$ for different doping levels. Samples from different sets displayed different concentrations of secondary phases. Typical examples for samples with a very low and a very high concentration of these phases is shown below.

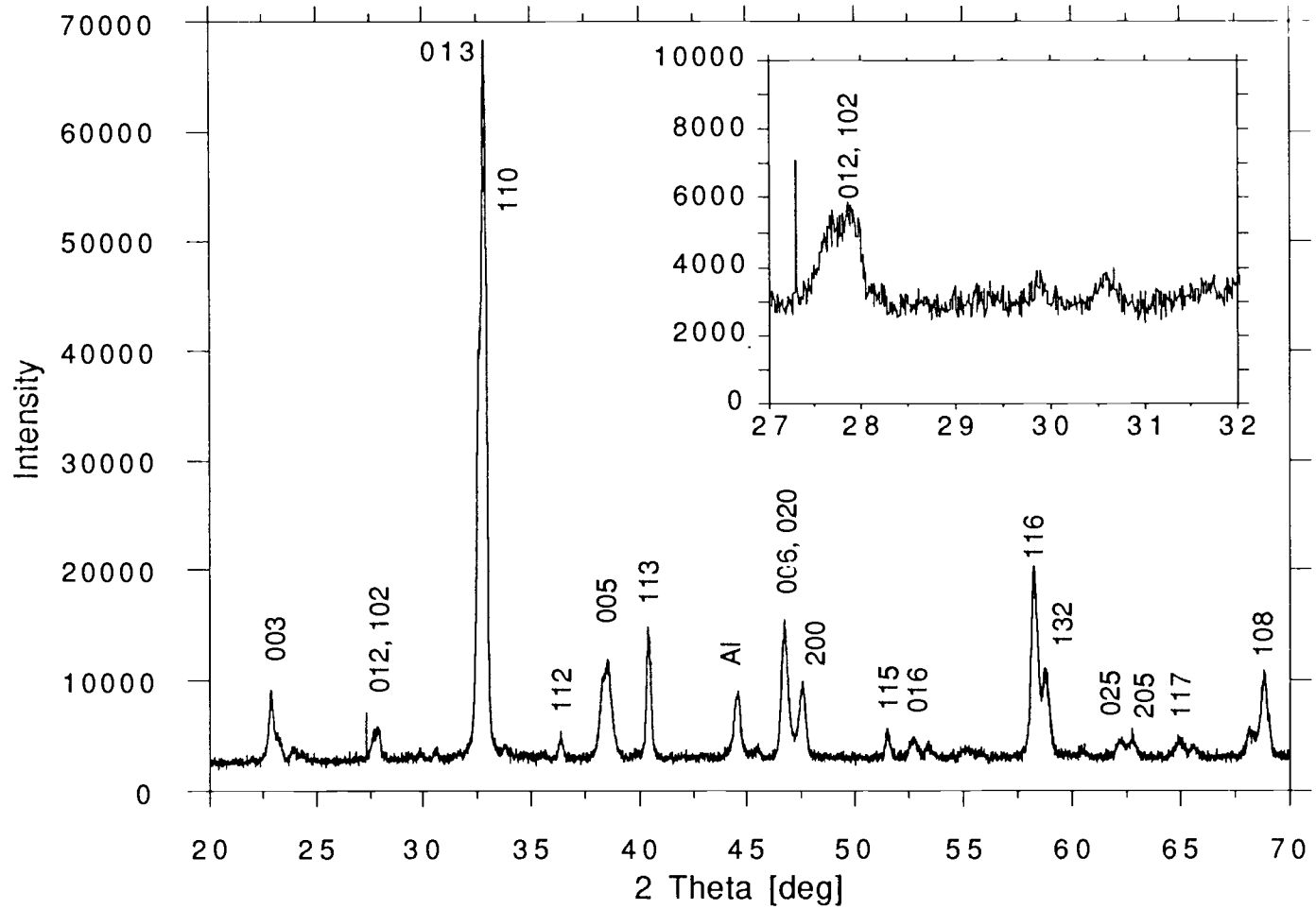

Fig. 6.1 (a) X-ray spectrograph for pure $YBa_2Cu_3O_{7-x}$ containing low concentration of secondary phases

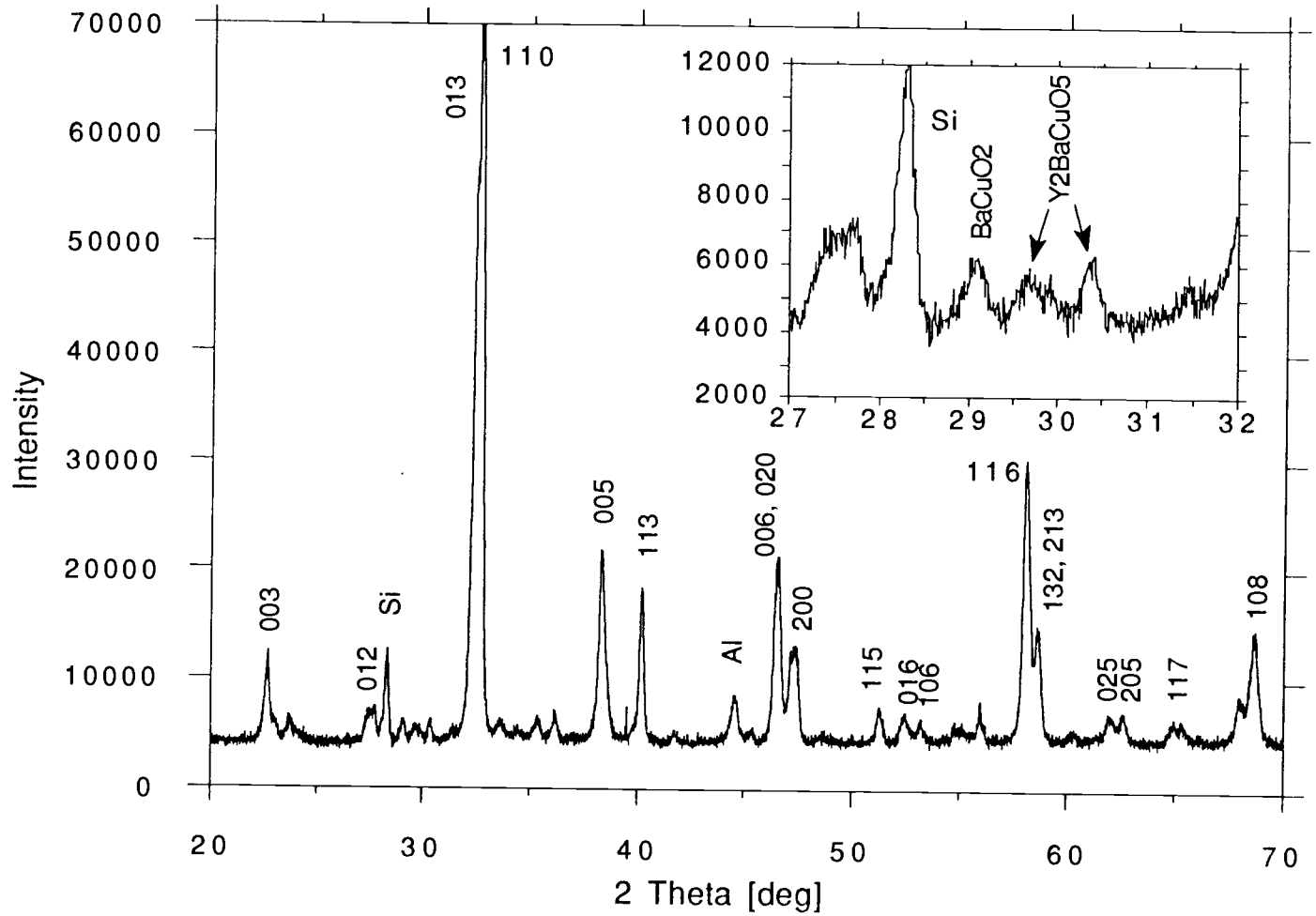

Fig. 6.1 (b) X-ray spectrograph for pure $YBa_2Cu_3O_{7-x}$ containing high concentration of secondary phases

6.1.1 CALCULATION OF THE STRUCTURE FACTORS AND INTENSITIES

Under the assumption that the added In is dissolved in the sample, it is expected that the average Bragg spacing d as well as the intensities of Bragg reflections from planes containing In change continuously with respect to the amount of added In.

The expected theoretical change of structure factors and consequently intensities for Bragg peaks correlated with the sites of substitution were calculated with the help of a software program. In this way it was possible to compare theoretically calculated data with the experimental data and to make conclusions about the solubility limit and the substitutional site.

The software program made use of a point ion model to calculate the structure factors and intensities for certain Bragg planes.

Sufficient input for the program consists of the following parameters:

- type of space group (PMMM for 1-2-3)
- lattice parameters a, b, c
- element indication of the ions involved in the lattice
- coordinates of the sites within a unit cell with respect to a defined origin
- relative occupancy of the site
- type of radiation of the simulation (transition of Cu Kα for 1-2-3)
- lower and upper limits for diffraction angle of scan.

A sequence of public-domain algorithms was used as the core of the software program to calculate the following output :

- information about the symmetry of the lattice (Bravais characteristics)
- information about the lattice group (cubic, tetragonal, orthorhombic, etc.)
- location of the symmetry center
- possible conditions limiting the reflections
- scattering factor coefficients for each ions
- Miller indices for every calculated peak where constructive interference occurs
- 2θ value for this peak
- Bragg spacing d for the peak
- intensity of the peak
- structure factor for the peak (with real, imaginary part and phase angle)
- multiplicity of the powder line
- Lorentz polarization factor.

The program calculates the structure factor taking only the change of atomic form factors due to doping into account. Usefulness and comparability of the theortically achieved data are ensured only under the following assumptions:

- the added amount of In will totally dissolve in the major phase of the sample

therefore: - there will be no secondary phase

- In will substitute at a unique site
- Bragg spacings will not change due to doping and consequently Bragg angles will remain constant.

The simulation was performed for substitutions at the Y, Ba, Cu(1) and the Cu(2) site. The lattice parameters for the calculation were taken from a reference.[44] Corresponding to the site, the original ion was partially replaced by In. This was accomplished by changing the relative occupancy for the corresponding cation site and introducing In atoms instead.

Certain Bragg planes contain the original ions and doped In ions. The structure factor for these Bragg planes are calculated by use of atomic form factors of both types of ions, because only a fraction of the cation site is substituted. A change in intensity due to doping is expected. The change for the average structure factor and intensity is continuous for angles $0 \leq \theta \leq 90°$.

To obtain comparisons with experimental data, the intensities were normalized by the 116 peak which served as a norm for the experimental data.

Peaks of reasonable intensity which were at least 10 % of the highest intensity and had a significant intensity change were selected as potentially comparable with experimental results. Those peaks were 002, 003, 012, 102, 112, 005, 113 and 115.

The following four tables for possible substitutions show integrated intensities of the 003, 112 and 113 peaks as a function of In concentration.

% In \ hkl	003	112	113
0 %	82.5	45.5	278.2
5 %	83.8	43.8	279.8
10 %	85.2	42.1	281.4
15 %	86.6	40.4	283.0
20 %	88.0	38.8	284.6

(a)

% In \ hkl	003	112	113
0 %	82.5	45.5	278.2
5 %	81.8	45.2	277.4
10 %	81.2	44.8	276.7
15 %	80.5	44.4	276.0
20 %	79.9	44.0	275.2

(b)

% In \ hkl	003	112	113
0 %	82.5	45.5	278.2
5 %	81.8	45.2	277.4
10 %	81.2	44.8	276.7
15 %	80.5	44.4	276.0
20 %	79.9	44.0	275.2

(c)

Tables 6.2 (a) - (c) Calculated intensities for 003, 112, and 113 peaks as a function of In concentrations for simulated substitution at the Y (a), Ba (b), and Cu(1) (c) site

% In \ hkl	003	112	113
0 %	82.5	45.8	278.2
5 %	78.5	43.7	269.8
10 %	74.7	41.5	261.6
15 %	71.1	39.4	253.7
20 %	67.6	37.3	245.9

(d)

Table 6.2 (d) Calculated intensities for 003, 112, and 113 peaks as a function of In concentrations for simulated substitution at the Cu(2) site

Most of the above peaks, however, interferred with other peaks. The only peak which showed a reasonable intensity, changed strongly enough in intensity, and did not interfere with other peaks was the 003 peak.

Results of the simulation indicate only for the substitution at the Y site a positive change, i.e. increasing intensity (+0.9 % of intensity between pure sample and 3% doping level). Substitutions at the Ba site (-0.48 %), the Cu(1) site (-2.94 %), and the Cu(2) site (-2.72 %) show a decreasing intensity as a function of In concentration.

6.1.2 EXPERIMENTAL RESULTS OF X-RAY DIFFRACTION MEASUREMENTS

Three attempts to determine the solubility limit and the substitutional site were performed using different methods of evaluation.

1) The first method was exclusively concerned with the change of the Bragg spacing d on the concentration of In. Early results of this work are shown in figure 6.2: Bragg peak shift as a function of In concentration.

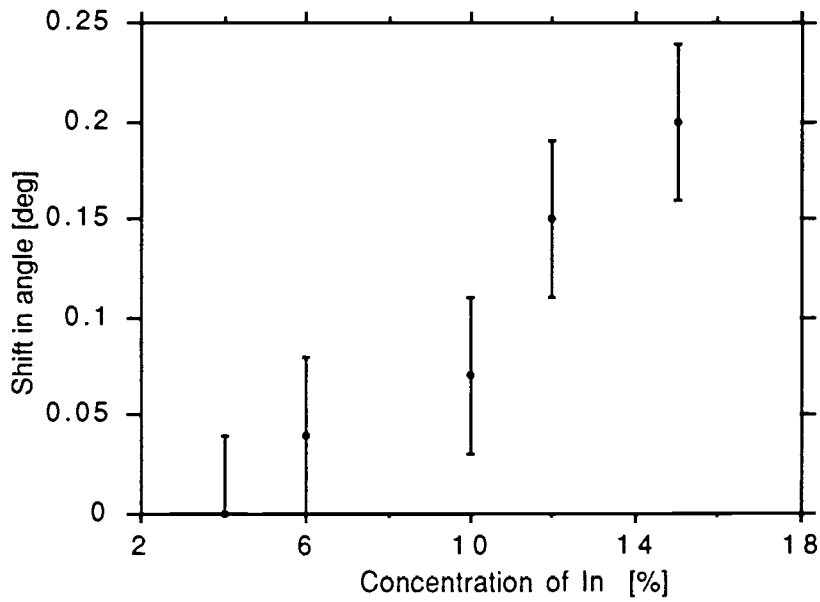

Fig. 6.2 Experimental Bragg Peak shift as a function of In concentration

This method was abandoned because changes in 2θ were reproducible but did not exceed the error bars.

2) The second method investigated the Bragg peak intensities. The intensity values were obtained from the top of the peaks. This technique of evaluation was applied to data from X-ray diffractographs made from the first and second sets.

A finite distribution in angle 2θ of Gaussian form occurs for a Bragg peak. The full width at half maximum of the Gaussian is independent of the peak intensity.

Therefore, the physical Bragg intensity, which is the integral over the peak, is not proportional to the absolute peak top value.

3) The third evaluation technique investigated the integral over the peak and its dependence on Indium concentration. This technique was applied to all three sets of samples.

6.1.2.1 MAJOR PHASE $YBa_2Cu_3O_{7-X}$

As a result of this technique, the following tables below display the normalized, integrated intensity values of the 003 peak for different doping levels.

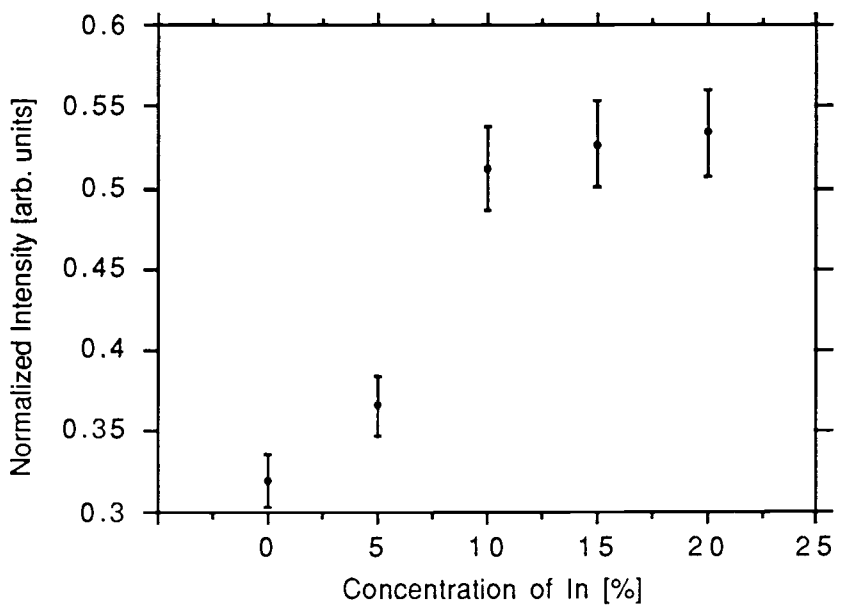

(a)

Fig. 6.3 (a) Experimental relative intensities of 003 with respect to In concentration: set #1

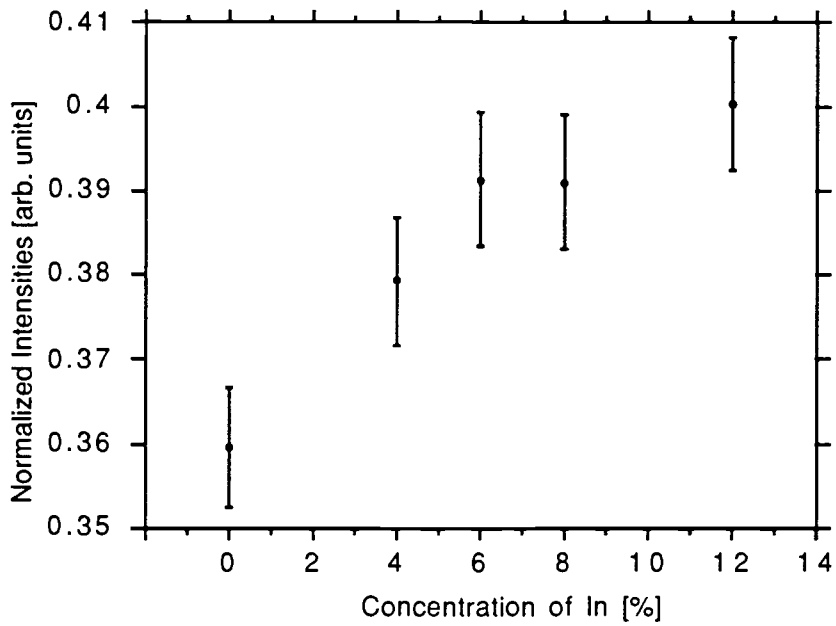

(b)

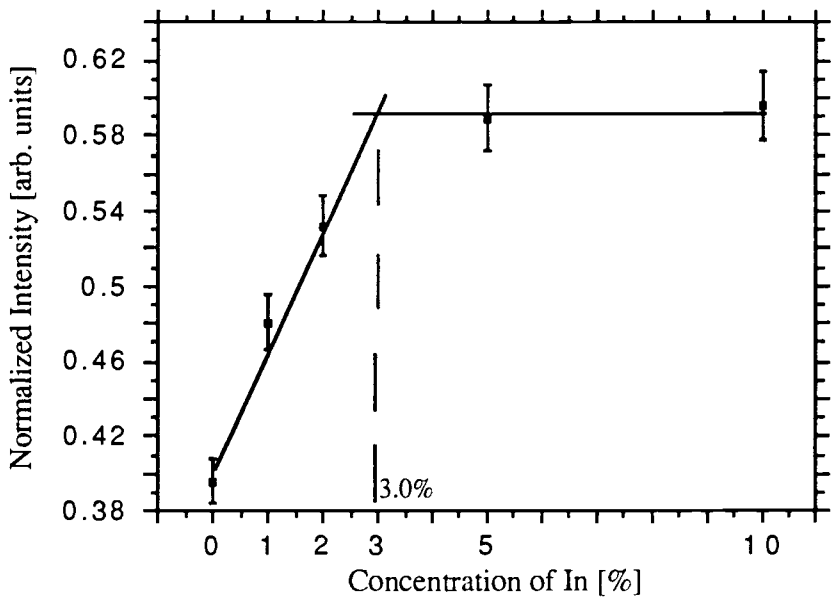

(c)

Fig. 6.3 (b), (c) Experimental relative intensities of 003 with respect to In concentration: set #2 (b) and set #3 (c)

The number of measured values is 5 for each set. Therefore, it would be rather difficult to determine a solubility limit from these data exactly. The time between measurements of different samples was 3 months. The Philips Diffractometer is calibrated at frequent intervals and no recalibration was done between measurements of one set. This explains the different intensities for different measurements.

The graph for set #1prepared with added $In(NO_3)_3$ shows increasing values of relative intensities for the 003 peak up to 6 % In. For samples containing more than 6 %, the relative intensities are constant within uncertainty limits.

Measurements from sample set #1 should only serve as an indicator for a solubility limit, because of principal distortions of the cation ratios for higher In concentrations due to preparation .

The graph for set #2 shows relative intensities of 003 increasing up to 10 %. Samples with higher concentration have the same relative intensity.

This set of measurements displayed even for the pure $YBa_2Cu_3O_{7-x}$, containing no In, a very high concentration of secondary phases (see Fig. 6.1(b)). Possible reasons for this are an initial distortion of the mixing ratio within the nitrate mixture, an incomplete reaction of the ions involved in the superconducting material or a strong inhomogeneity of the bulk sample during the X-ray measurement.

All samples of this set were prepared from the same parent solution of $YBa_2Cu_3O_{7-x}$, which means that they contain the same concentration of secondary phases. The high concentration of secondary phases provided a non-negligible number of sites for possible substitution of the In cations. This explains a rather high In saturation of 10 %.

The graph for sample set #3 displays an increase in relative intensity for samples with In concentration less than 3.0 %. Higher concentrations do not change the intensity ratio within uncertainty limits. The initial concentration of secondary phases is extremely low (see Fig. 6.1(a)). Also for higher concentrations of In, the concentration of secondary phases remains low.

The data of this measurement are therefore the most credible ones and results from the evaluation of those data were used for conclusions about the solubility limit.

6.1.2.2 SECONDARY PHASES

Besides the major phase $YBa_2Cu_3O_{7-x}$[45], a variety of secondary phases were detected during this work. These phases were $BaCuO_2$, CuO, Y_2BaCuO_5.[46,47,48] For In-saturated samples $In_1Ba_2Cu_3O_x$ was detected. For sample set #2 $Ba_2Cu_3O_x$ was detected in traces.

Table 6.3 shows physically interesting features of the secondary phases

	conc. [%]	lattice	maj.peak
BaCu2	2.5	cubic	29.2 deg
CuO	2	monoclinic	35.6 deg
Y2BaCuO5	2.5	orthorh.	29.8 deg
InBa2Cu3Ox	0-20	?	30.6 deg

Table 6.3 Typical concentration, lattice type, and major peaks (2θ) of secondary phases

Y_2BaCuO_5 has a green color, $BaCuO_2$ and CuO are black like the major 1-2-3 phase.

$In_1Ba_2Cu_3Ox$ was detected above the solubility limit in the major phase. It is a recently discovered compound with unknown lattice structure. Preliminary work by Dr. Sommers including single-crystal growth and X-ray investigations has been done. At the time of writing of this thesis, however, no published and established reference, including the JCPDS catalog, could be found.

The X-ray pattern below displays $InBa_2Cu_3O_x$ as the strongest secondary phase in the bulk.

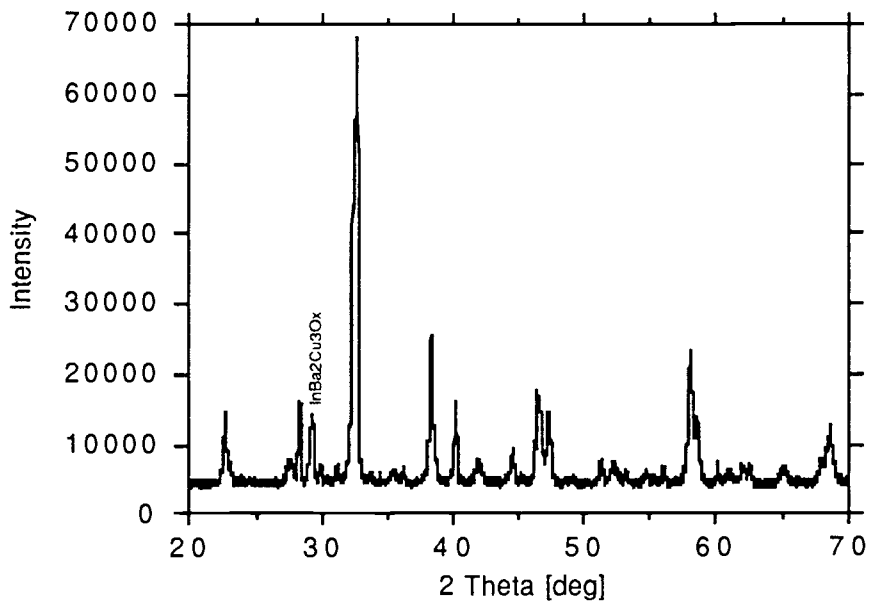

Fig. 6.4 X-ray pattern of $YBa_2Cu_3O_{7-x}$ containing 20% In

In the four graphs below X-ray spectra of $BaCuO_2$, CuO, Y_2BaCuO_5, and $InBa_2Cu_3O_x$ are shown. The samples were prepared and measured by me.

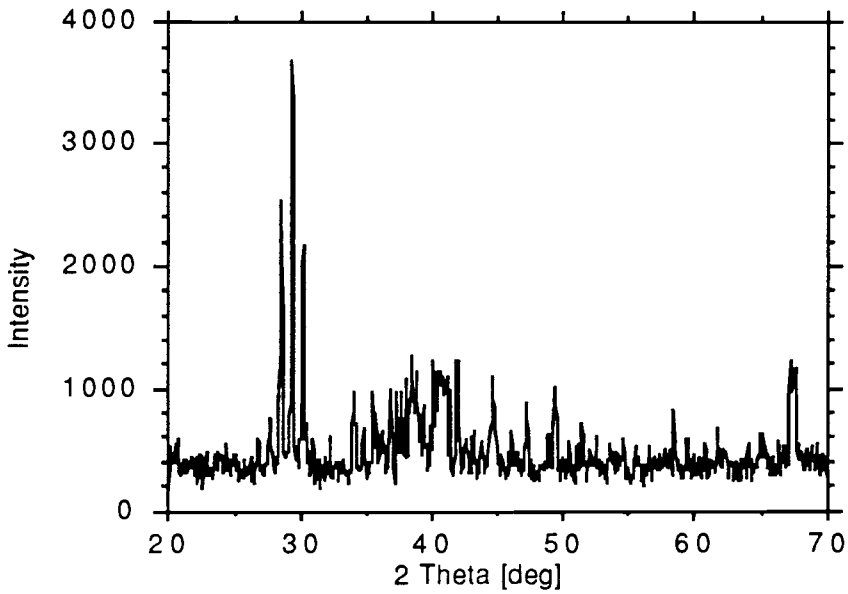

(a) $BaCuO_2$

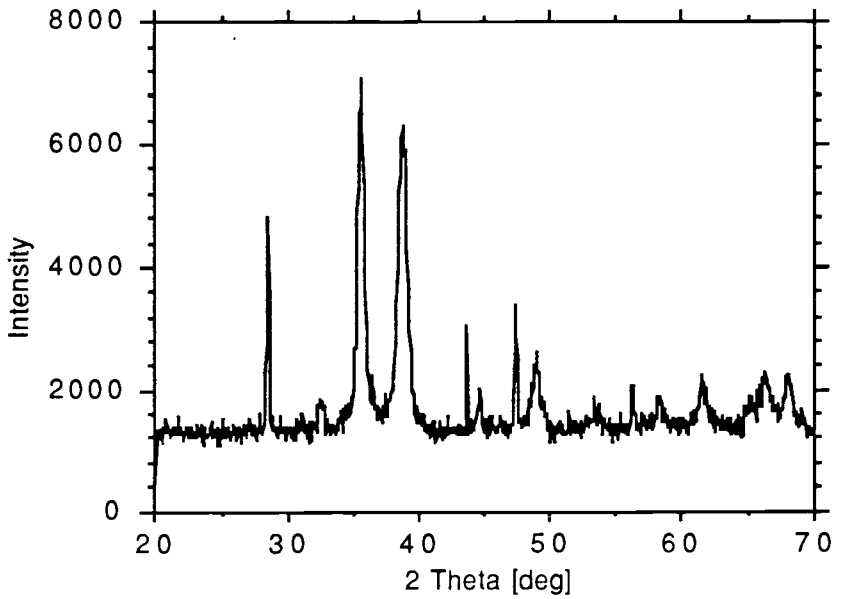

(b) CuO

Fig.6.5 (a), (b) X-ray pattern for $BaCuO_2$ (a) and CuO (b)

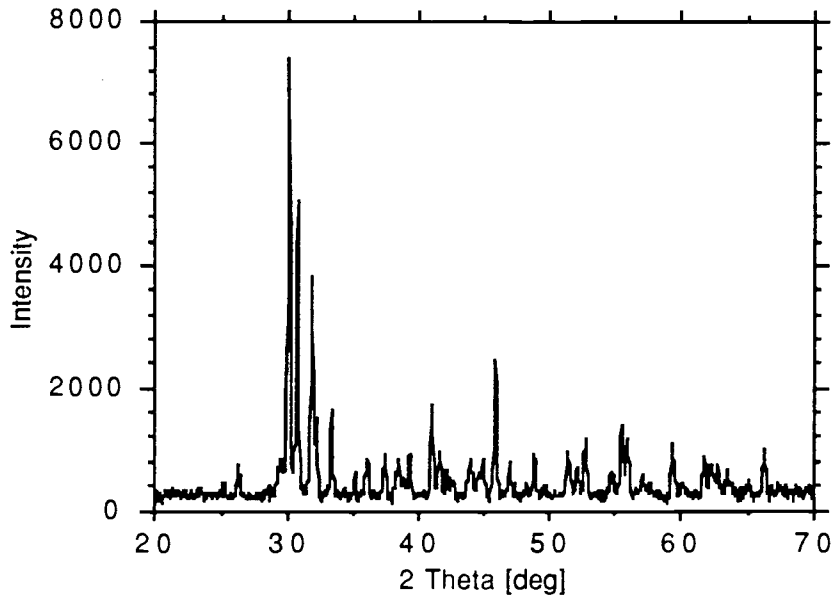

(c) 211

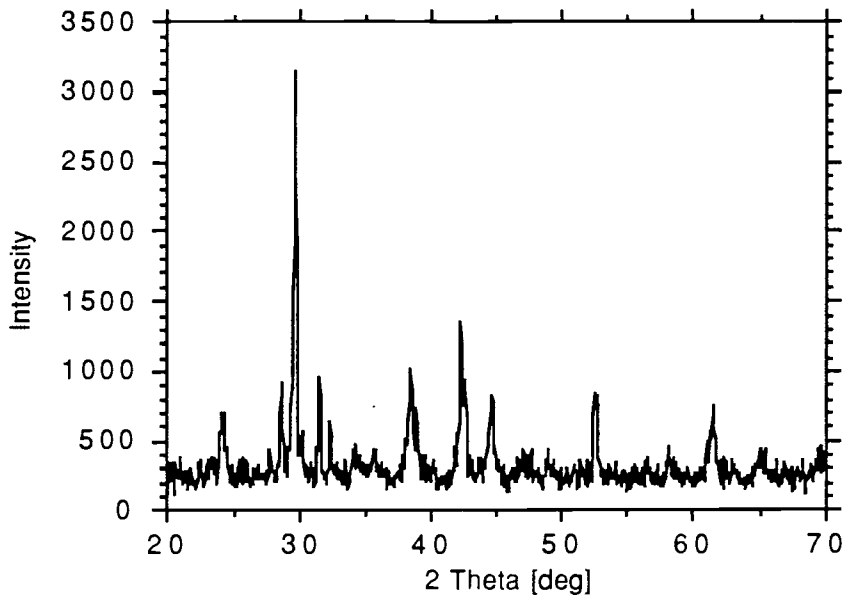

(d) In123

Fig.6.5 (c), (d) X-ray pattern for Y_2BaCuO_5 (c) and $InBa_2Cu_3O_x$ (d)

$InBa_2Cu_3O_x$ is the most interesting secondary phase. It has three major peaks at 30.6°, 41.8°, and 61.2°. The strongest peak at 30.6° interferes with the major peak of $BaCuO_2$. The peak interference, however, was approached by either one of the integration methods which will be described below.

The graph below shows the major peaks of $BaCuO_2$ at 29.9° and $InBa_2Cu_3O_x$ at 30.6° .

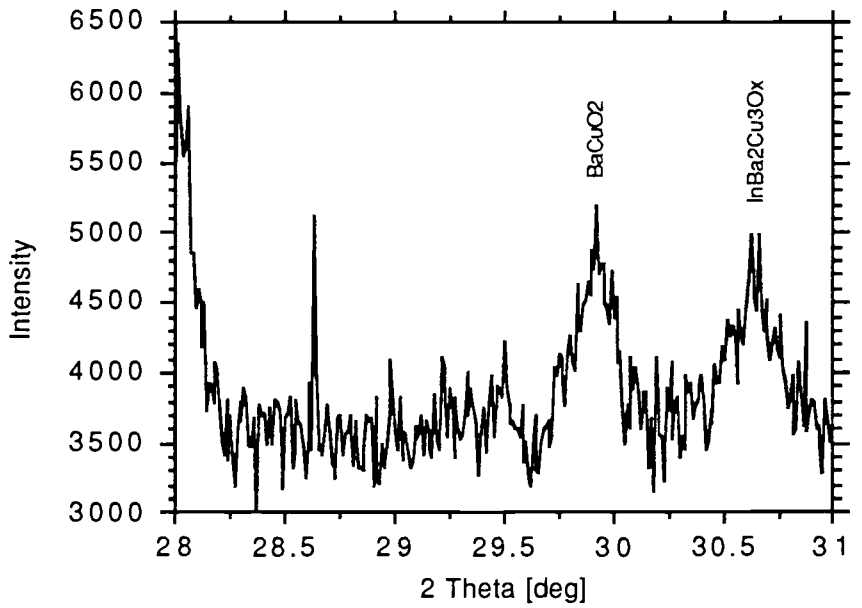

Fig. 6.6 Major peak of $InBa_2Cu_3O_x$ at $2\theta = 30.6°$

$BaCuO_2$ has three strong peaks between 28° and 29° and a double peak at 67.9°. Y_2BaCuO_5 shows three major peaks between 29° and 32° and CuO has its two strongest peaks at 35.5° and 39°.

The following factors cause the generation and detection of secondary phases:

- Even in extremely carefully prepared, calcinated and measured samples, a finite concentration of secondary phases was present, because the mixing ratio of the nitrate solutions was never perfect and the excess Y, Ba or Cu ions precipitated out.
- Inhomogeneous distributions of the ions in the bulk sample during calcination causes incomplete reactions and excess secondary oxides
- Since X-ray diffraction is a surface-sensitive experiment, the surface layer (≤ 50 μm) contributes mainly to the detection of the phases. Inhomogeneous distributions of secondary phases in the bulk sample during the measurement can cause the surface distribution of the sample to be different from the bulk distribution. The results for those measurements will show a wrong concentration of secondary phases.

Problems arising from the existence of secondary phases in the sample are:

- the interference of spectra from secondary and major phases
- a distortion of the atom ratio of Y, Ba and Cu ions and in general excess of one or two of those
- a possible substitution of In in the secondary phase
- chemical reactions of the major phase 1-2-3 with secondary phases.

The problem of line separation was solved in general in the following two ways:

1) For the case of two overlapping peaks with comparable intensity, the integral over one of those peaks can be calculated by integrating over the superposed graph from background level for 2θ up to the intensity minimum between the two original peaks (see graph below). Since the intensities for both peaks are equal, the intensity which is missed by the shortening of the integration is equal to the intensity gained by the contribution of the second overlapping peak.

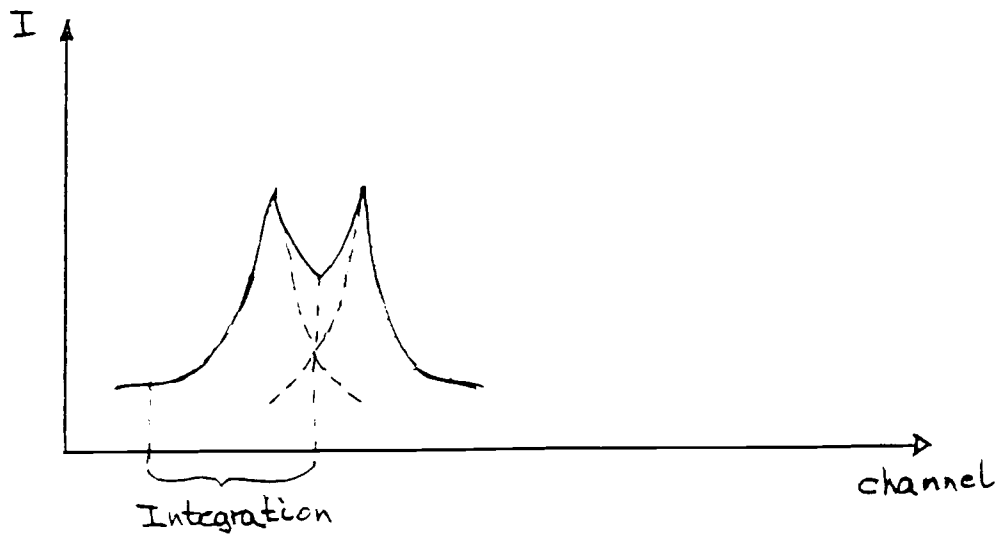

Fig. 6.7 Two overlapping peaks with same intensity

2) For peaks with unequal intensities, the intensity of one peak can be obtained by integrating over the graph from background level to the peak top. The result has to be doubled in order to get the intensity of the peak. The assumption is, that in the half of the peak which is integrated, the interference with the second peak is small.

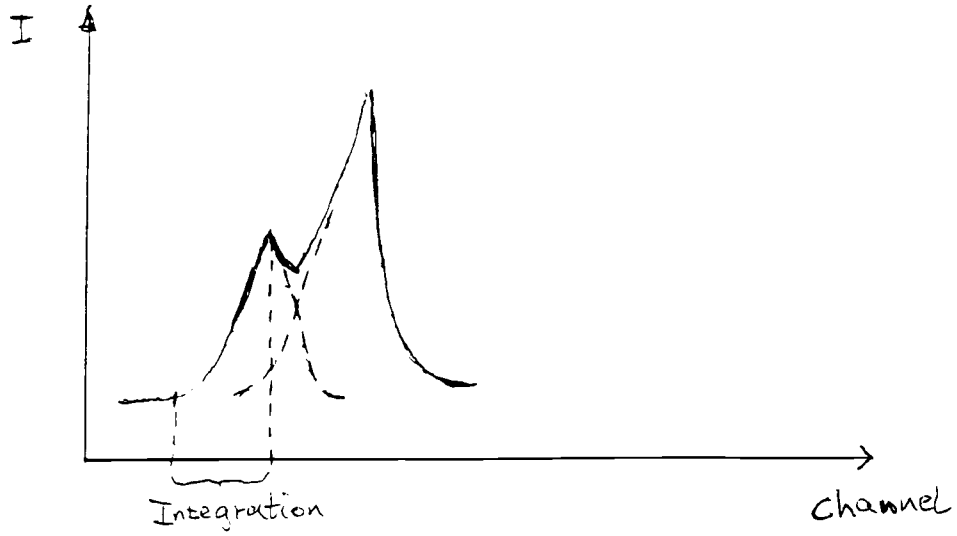

Fig. 6.8 Two overlapping peaks with different intensity

On the other hand, the existence of secondary phases and the possibility of the quantitative evaluation of their data can be used to gain information of the compound's substitutional properties. $InBa_2Cu_3O_x$ was used during the investigation of the solubility limit, because it precipitates out only in samples containing In concentrations higher than the solubility limit.

The other secondary phases $BaCuO_2$, CuO and Y_2BaCuO_5 had a constant relative intensity behavior with respect to In concentration. The intensity of two peaks in the secondary spectrum of Y_2BaCuO_5 are shown below.

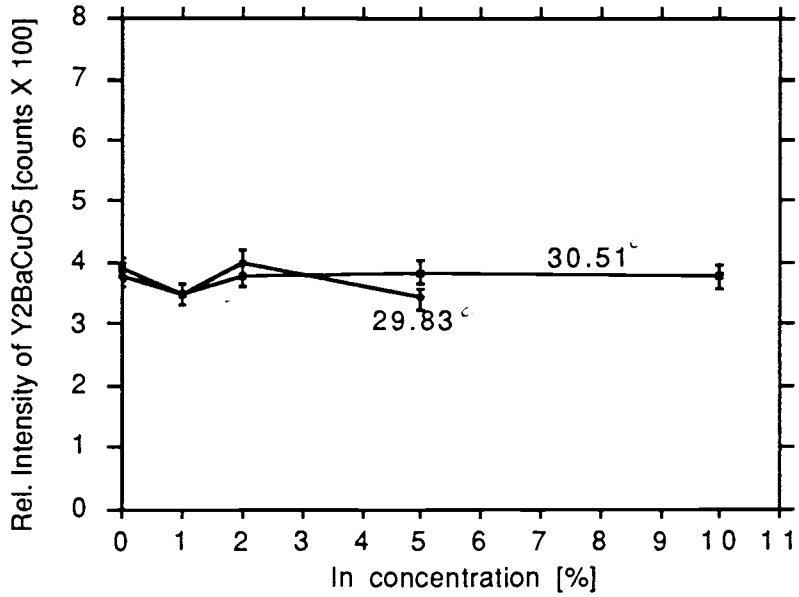

Fig. 6.9 Relative intensity of Y_2BaCuO_5 in the sample

The following three graphs display the relative, integrated intensities of $InBa_2Cu_3O_X$ at 30.6° and 41.8°.

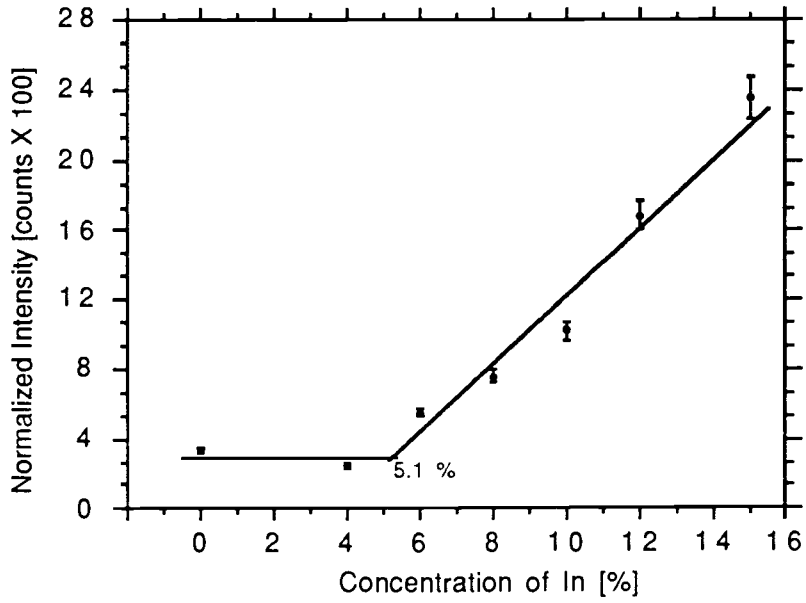

(a)

Fig. 6.10 (a) Relative intensity of strongest peak in the $InBa_2Cu_3O_X$ X-ray pattern for set #1

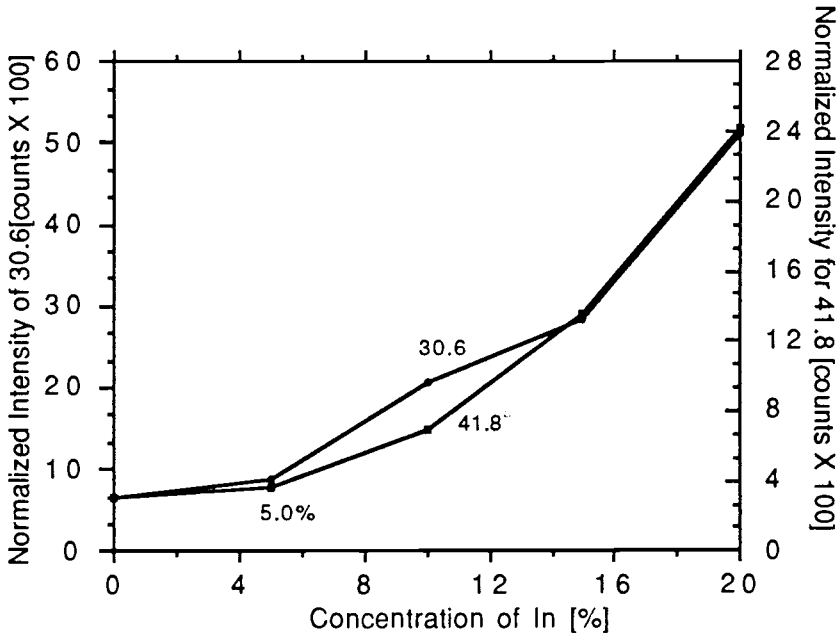

(b)

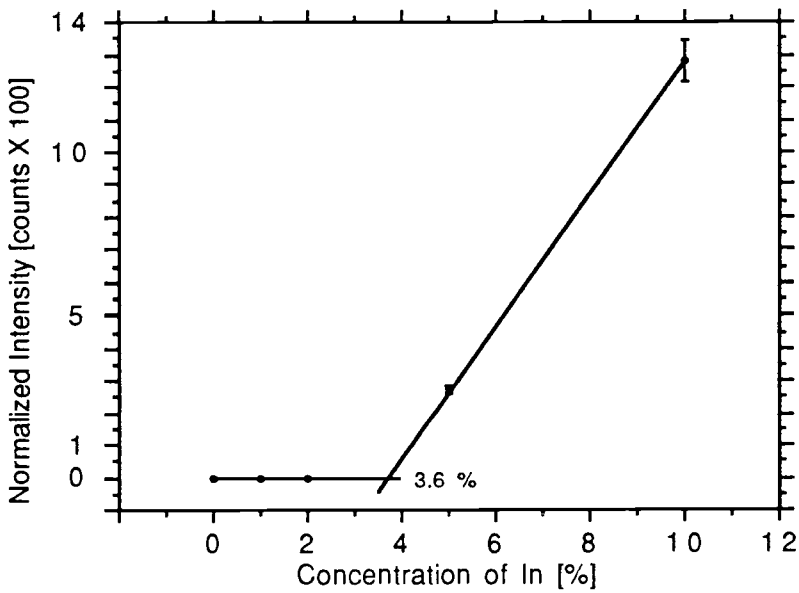

(c)

Fig. 6.10 (b), (c) Relative intensity of strongest peak in the $InBa_2Cu_3O_X$ X-ray pattern for set #2 (b) and #3 (c)

The graph for sample set #1 shows a significant increase of relative intensities for a In concentration higher than 5.1%. The intensity dependence on In concentration is rather complicated because of the distorted stoichiometry of the mixing ratio of the sample. The peak at 41.8° could not be well investigated because good measurements for this peak at concentrations 10, 12 and 15% could not be evaluated exactly. These intensities show a strong increase of intensity.

The intensity ratios for sample set #2 show a monotonic, linear increase in intensity for samples containing In above 5%. The two graphs with the peaks at 30.6° and 41.8° could be matched well.

For sample set #3 the intensity remaines constant for In concentration below 3.6% (by interpolation). The two samples with higher In concentration indicate a monotonic increase of intensity.

The intensities of all peaks for the CuO, $BaCuO_2$, and Y_2BaCuO_5 are either below the detection limit or show a constant intensity with respect to the In concentration.

6.1.3 COMPARISON OF THEORETICAL AND EXPERIMENTAL DATA

The teoretically predicted shift in relative intensity of the 003 peak in the 1-2-3 spectrum for Y-site substitution is much smaller than the experimental results. The theoretical difference in intensity between the 0% and the 3% In level of the peak is 0.9% of the total intensity. For the experiment, the intensity shift for the same peak is 30% .

6.2 PAC MEASUREMENTS

PAC experiments are far more sensitive to slight changes in and distortions of the lattice of the 1-2-3 compound than X-ray spectroscopy. In the case of very carefully prepared samples, PAC measurements can be a useful tool to investigate small variations of lattice parameters or structure factors.

A crucial factor influencing the sample quality is the sample processing. Slight variations from a careful sample preparation can result in large changes of PAC data. Those changes need not necessarily be detected by the global probe X-ray measurement.

The PAC Fourier transform of $YBa_2Cu_3O_{7-x}$ consists of a group of three major peaks at 55, 100 and 155 Mrad/sec. The three superimposed frequencies ω_1, ω_2 and ω_3 correspond to three energy differences of the sublevels of the intermediate state in the presence of an electric field gradient.

For sample set #3, a complete sequence of measurements was performed. The graphs for the samples containing 0%, 1%, 2%, and 5% In are shown below.

Fig. 6.11 shows $A_2G_2(t)$ spectra and the Fast Fourier Transform (FFT) of the data for pure $YBa_2Cu_3O_{7-x}$ at various temperatures. Figs. 6.12 to 6.14 show $A_2G_2(t)$ functions and the Fourier transform of the $A_2G_2(t)$ data for measurements with samples at different In concentrations as a function of temperature. Fig. 6.15 shows the PAC frequencies ω_1 and ω_2 dependent on temperature and Fig. 6.16 the asymmetry parameter η as a function of temperature.

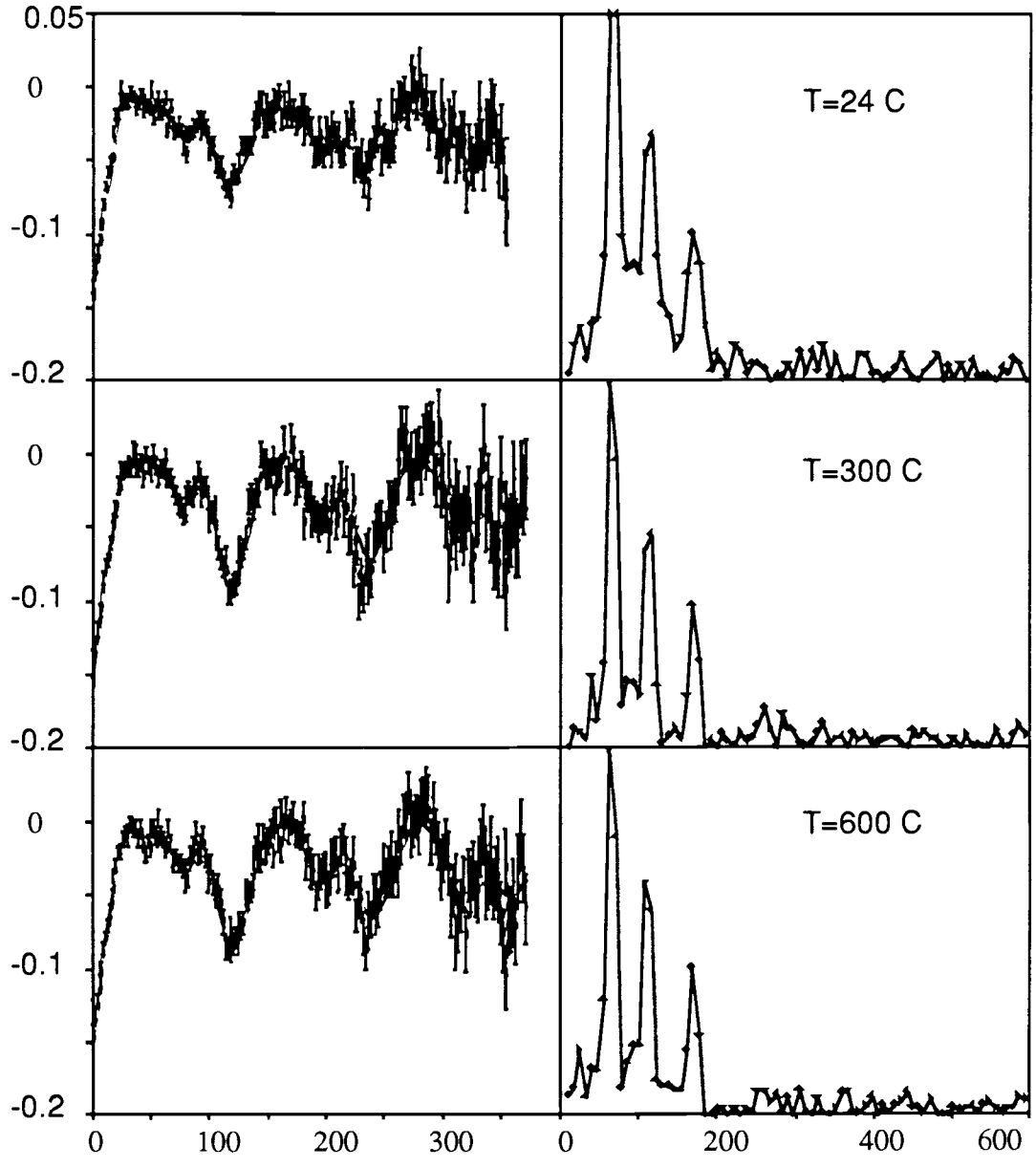

Fig. 6.11 $A_2G_2(t)$ spectra and FFT for pure $YBa_2Cu_3O_{7-x}$ at various temperatures

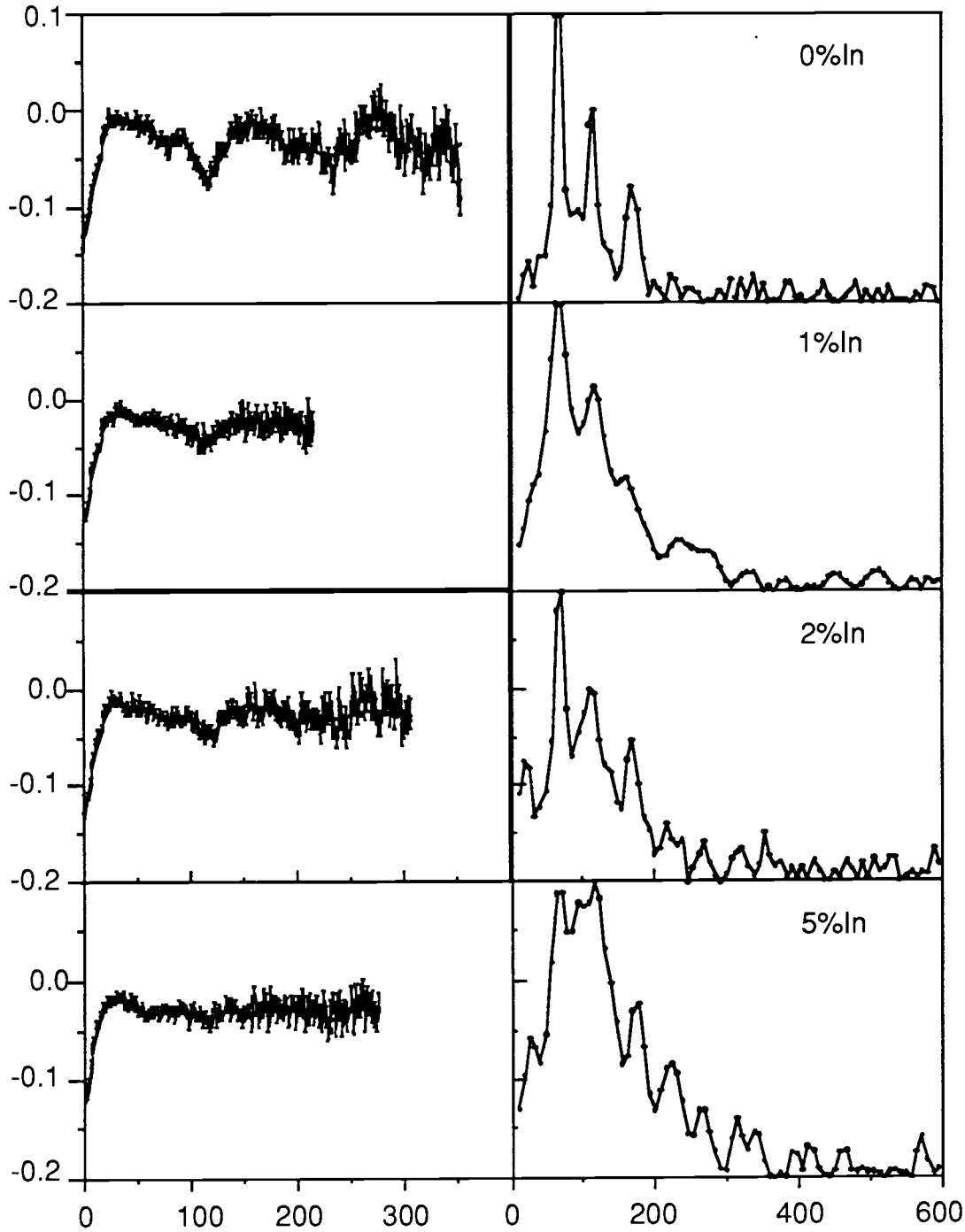

Fig. 6.12 $A_2G_2(t)$ spectra and their FFT for samples with various In concentrations at room temperature

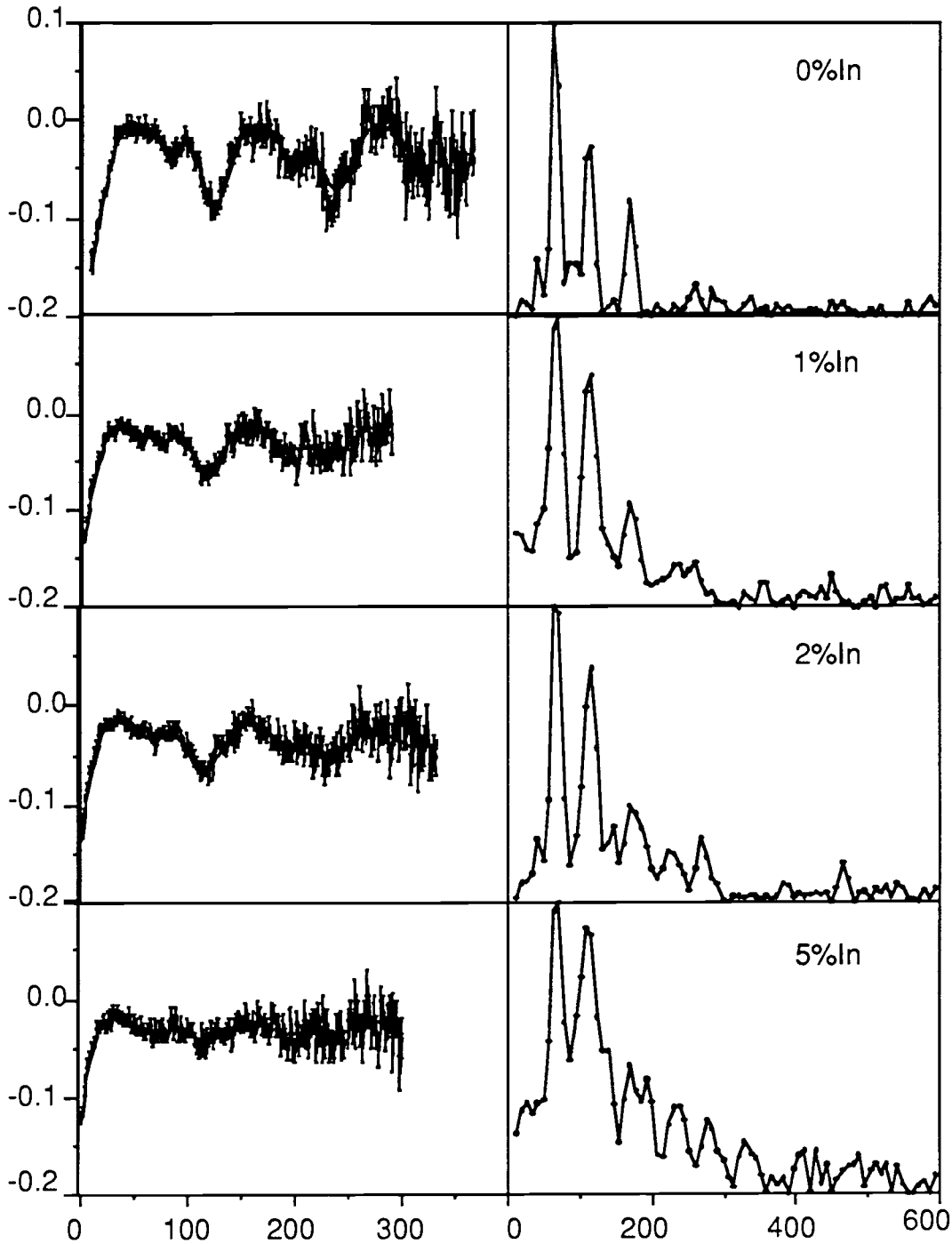

Fig. 6.13 $A_2G_2(t)$ spectra and FFT for samples with various In concentrations at 300° C

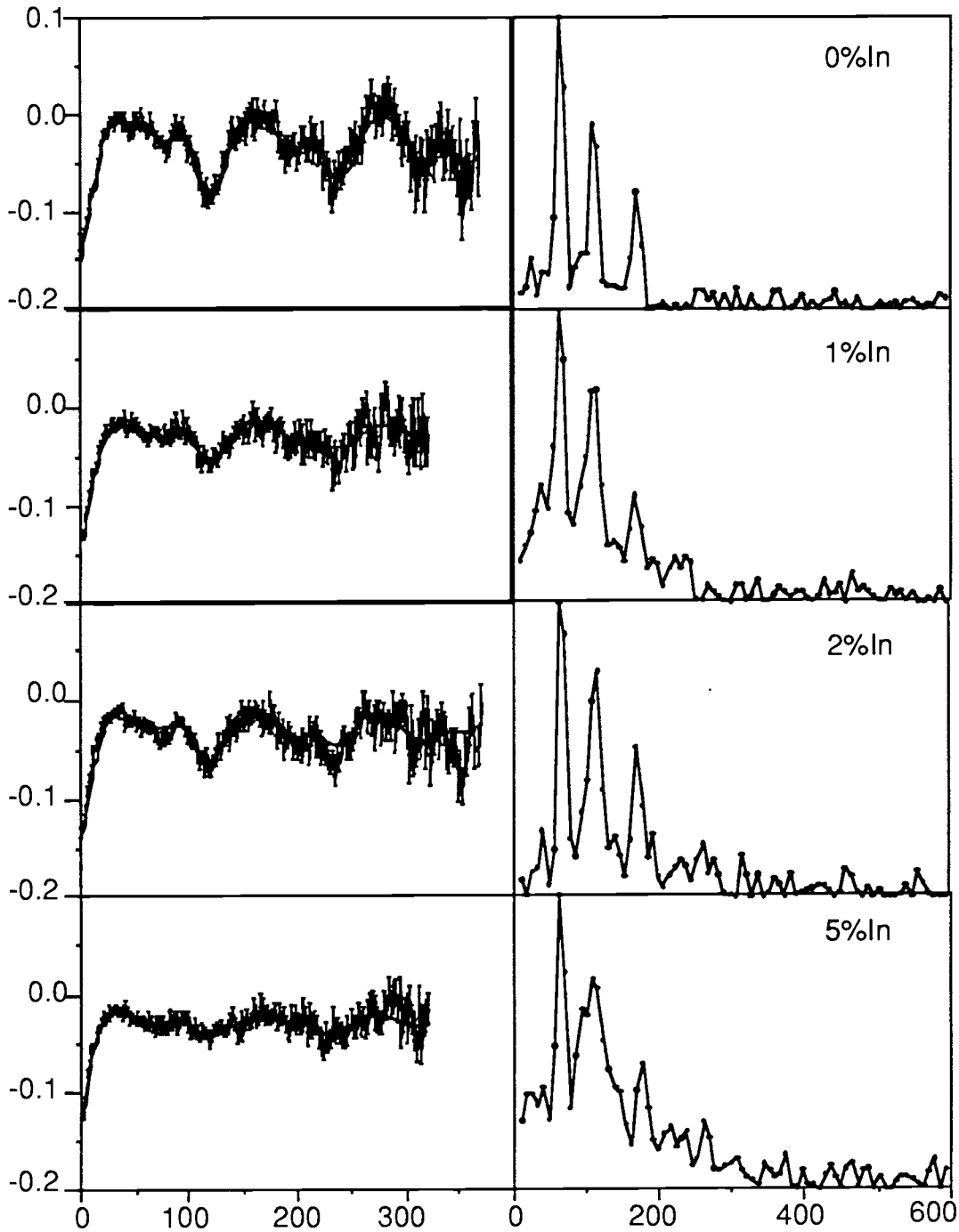

Fig. 6.14 $A_2G_2(t)$ spectra and FFT for samples with various In concentrations at 600° C

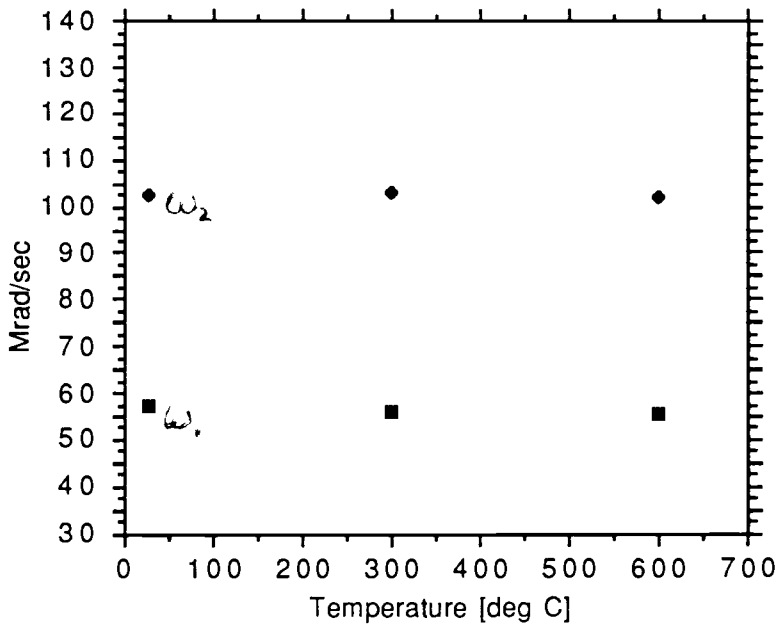

(a)

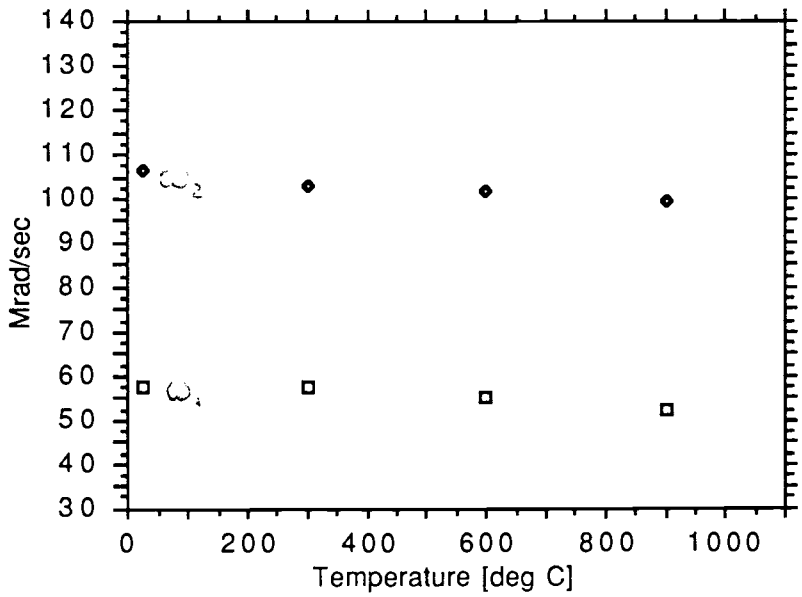

(b)

Fig. 6.15 (a), (b) ω_1, ω_2 for samples at various temperatures: 0% In (a) and 1% In (b)

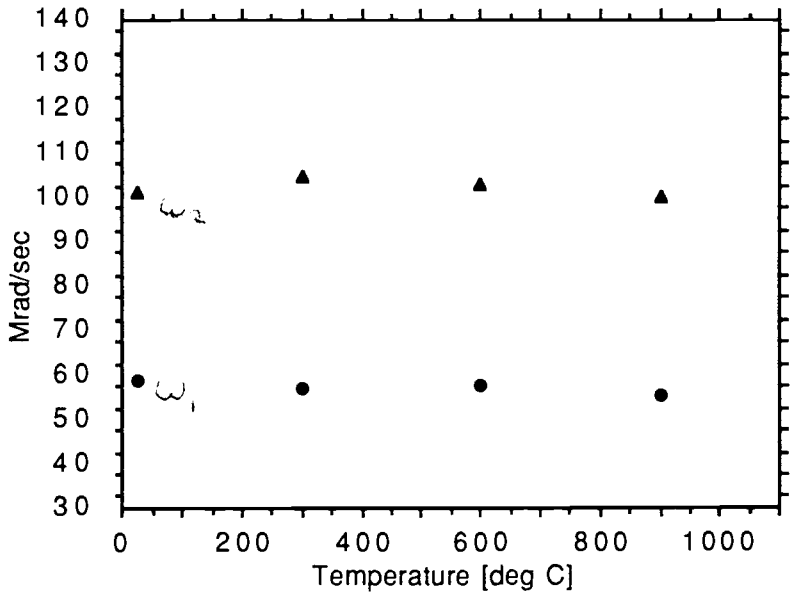

(c)

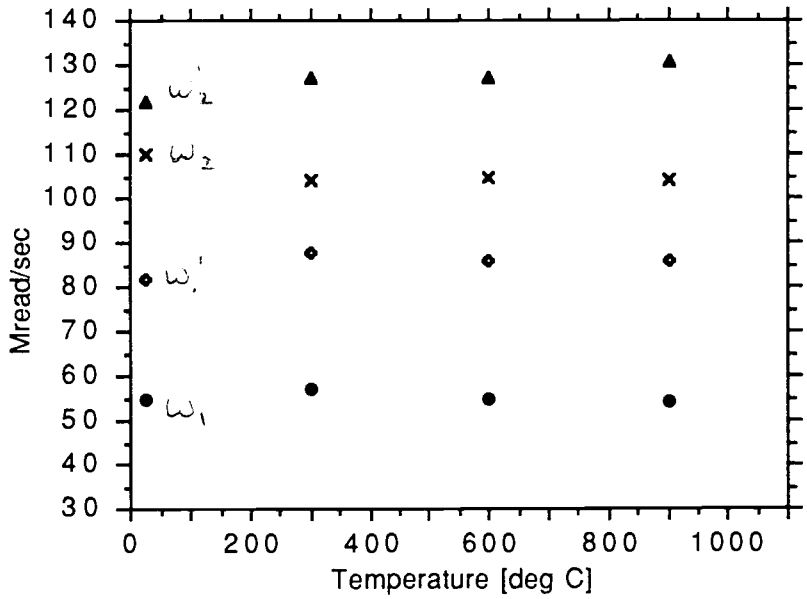

(d)

Fig. 6.15 (c), (d) ω_1, ω_2 for samples at various temperatures:2% In(c) and 5% In(d)

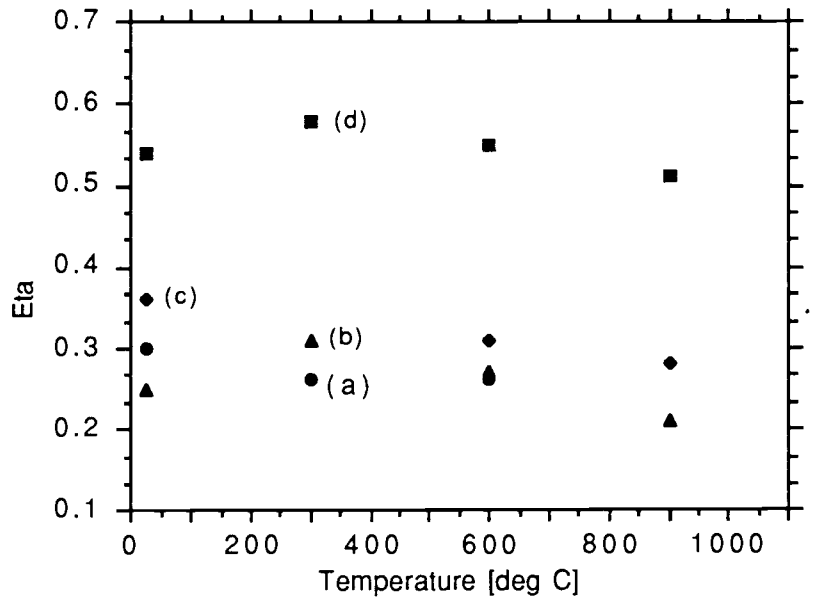

Fig. 6.16 $\eta(t)$ as a function of temperature for samples with 0% In (a), 1% In (b), 2% In (c), 5% In (d)

The samples with concentrations ≤2% In show the predominant "low frequency phase" or A-site phase, with peaks at 55, 100 and 155 Mrad/sec in the fast Fourier transform. The concentration of secondary phases is in all cases negligibly small. These sites include peaks at 30 and 110 Mrad/sec.

For the 5% In sample a secondary site with a distinct pattern at $\omega_1 = 82$ and $\omega_2 = 122$ Mrad/sec is detected, corresponding probably to a site in $InBa_2Cu_3O_X$.

6.2.1 SAMPLE PROCESSING INDUCED VARIATIONS IN PAC MEASUREMENTS

A total of 16 PAC samples were prepared during this work. The sample quality and the generation of the phases depended strongly on the way of sample preparation.

If the calcination temperature is below 800° C, a pseudo-cubic phase of $YBa_2Cu_3O_{7-x}$ is generated with lattice parameters a=b, c=3a.

Often, a secondary phase in a major amount was generated, called the "Mystery phase" or high frequency (HF) phase. The spectrum consists of a solitary peak at 240 Mrad/sec. The X-ray pattern of this phase will be called X-phase.

Fig. 6.17 shows the $A_2G_2(t)$ spectrum and its FFT for a PAC measurement at 950° C. The X-ray pattern in Fig. 6.18 consists of a superposition of the known spectrum of 1-2-3 and the X-phase. The major peaks of the X-phase are indicated.

Origin and the chemical composition of this X-phase are unknown and could not be established during this work. It is, however, assumed, that the generation of this phase is caused by an oxygen deficiency during calcination and during measurements at elevated temperatures (950°C).

Many parameters connected with the sample processing influence the quality of the sample. Among them are the following:

- Temperature of calcination
- rate of cooling
- partial oxygen pressure of the atmosphere inside the furnace during calcination
- age of the ^{111}In isotope.

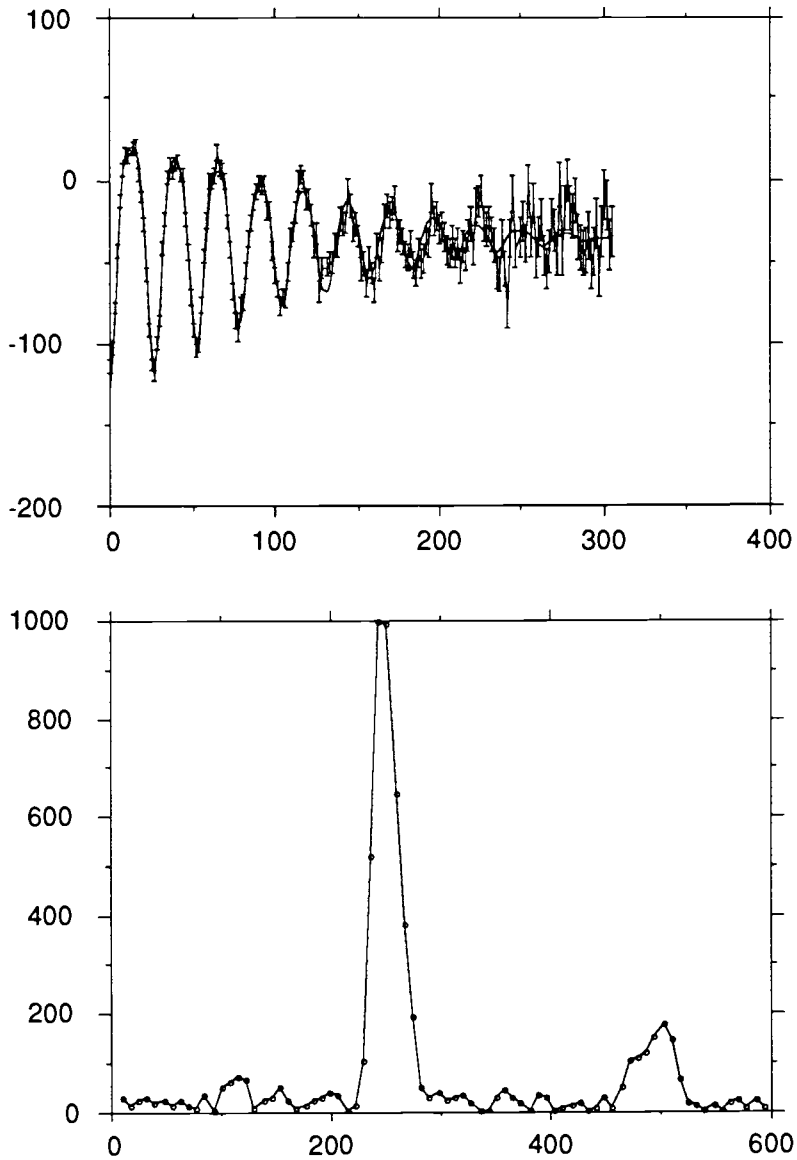

Fig. 6.17 A2G2(t) and FFT for HF phase

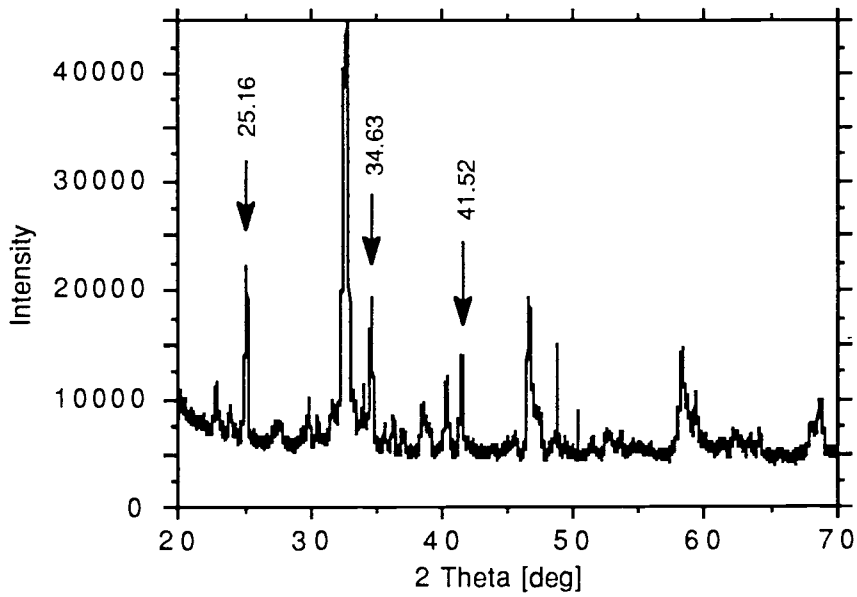

Fig. 6.18 X-ray pattern for X-phase

An especially slow cooling rate of 40° C/h provided the necessary scenario to accumulate a high oxygen concentration in the sample. The oxygen concentration in the sample is proportional to the oxygen concentration in the atmosphere of the furnace.

The isotope is diluted with HCl solution, and its half-life is 2.83 d. The age of the In isotope determined the sample quality, because the excess HCl undergoes a reaction with ions in the lattice and precipitates out as a secondary compound.

In order to obtain the same absolute radioactivity, after several days a much higher amount of diluted In had to be added. This results in a higher concentration of Cl^- anions in the sample. If the ratio Cl^- ions/$(NO3)^-$ ions exceeds a value of 50, the chloride ions possibly react in a detectable manner with Y^{-3} to YOCl and with Cu^{-2} to CuCl. This might cause a contribution to the HF phase, or the HF phase might be either one of the above phases.

This hypothesis is supported by the fact that PAC samples made with older In isotope show more HF phase than samples made of "fresh" isotope.

6.3 MAGNETIC FLUX EXCLUSION MEASUREMENTS

The purpose of these experiments was the determination of the critical temperature T_c which is a good indicator for the quality of the sample.

Every superconductor has the tendency to expell an applied magnetic field in the superconducting state (Meissner effect). The expulsion sets in at the state transition to superconductivity. For superconductors of type I or hard super-conductors, the expulsion sets in abruptly, for type II superconductors the magnetic flux is expelled gradually below the transition temperature. The new group of high temperature superconductors is refered to as superconductors of type III and displays very similar features for the flux exclusion as type II superconductors.

The critical temperature is defined by the typically sharp onset of magnetic flux exclusion by the superconducting sample being exposed to an external magnetic field. The measurement of the penetrated magnetic field versus temperature gives a good indication of this fact.

The graph for the 0% sample shows two measurements for applied magnetic fields of 50 G and 100 G. A very sharp decrease in magnetic flux penetration at 92.7 K. The flux expulsion is very strong and the curve has no structure. This indicates a high sample quality.

A complete sequence of measurements for sample set #2 has been performed and the data graphs are shown below.

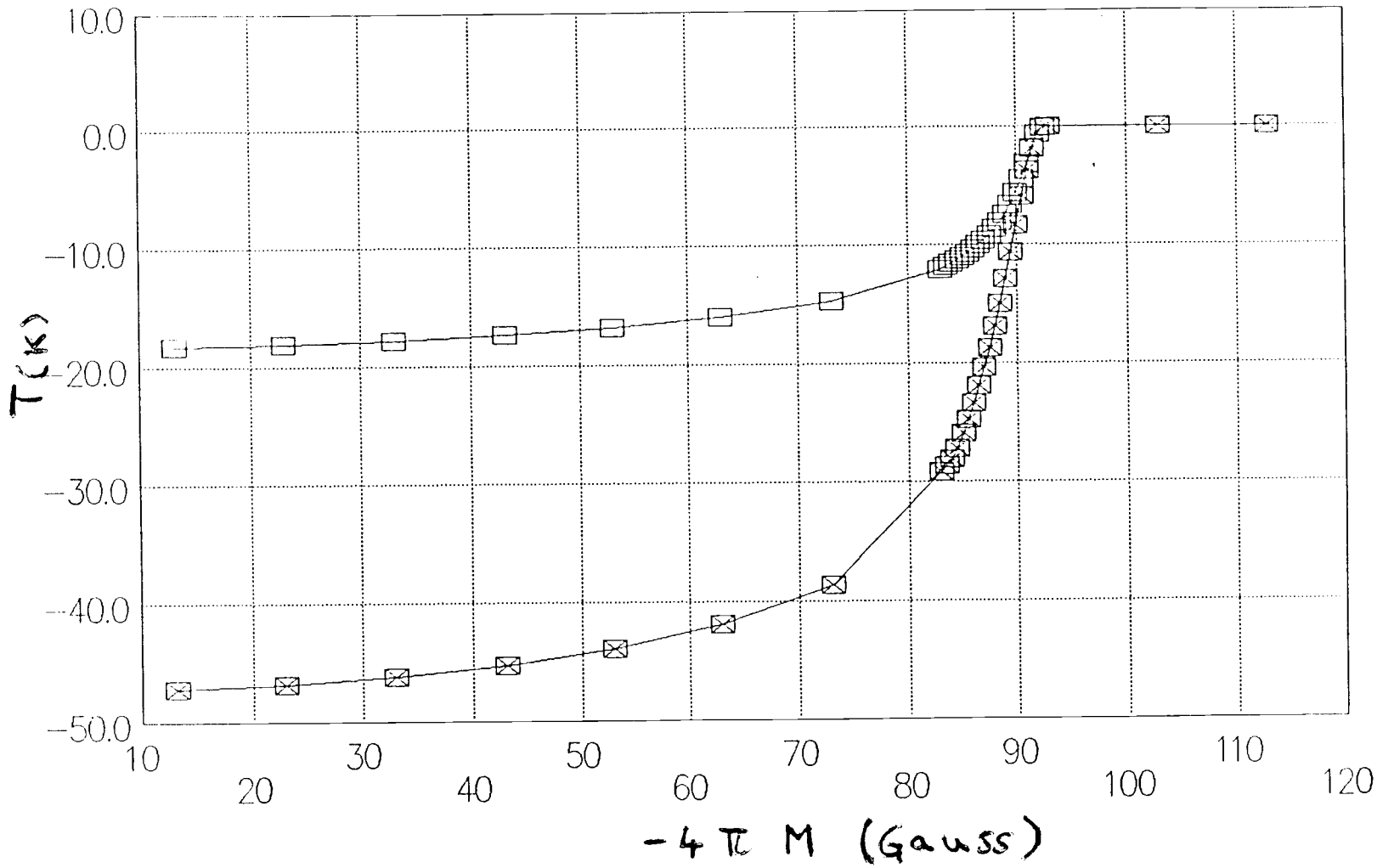

Fig. 6.19 Magnetic flux penetration as a function of temperature

As expected, the critical temperature varies with In concentration. The following graph indicates the dependence of T_c on In concentration.

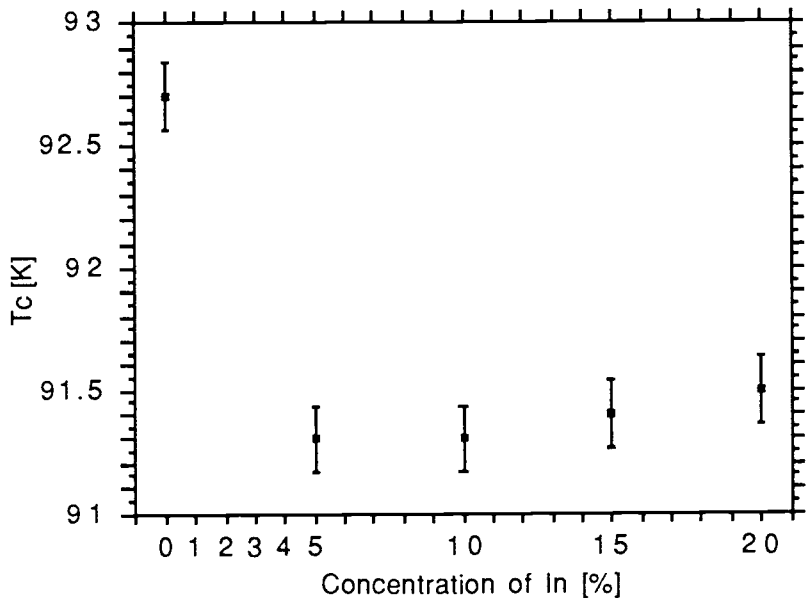

Fig. 6.20 T_c versus In concentration

T_c drops from 92.7 K for the 0% sample to 91.3 K for the 5% sample and remains constant for concentrations above 5% In within the experimental margins of error. This fact gives some ground for conclusions about the solubility limit and the substitutional site in the lattice and will be discussed in Chapter 7 : Discussions and Conclusions.

The graph below displays the expelled magnetic flux over concentration of In.

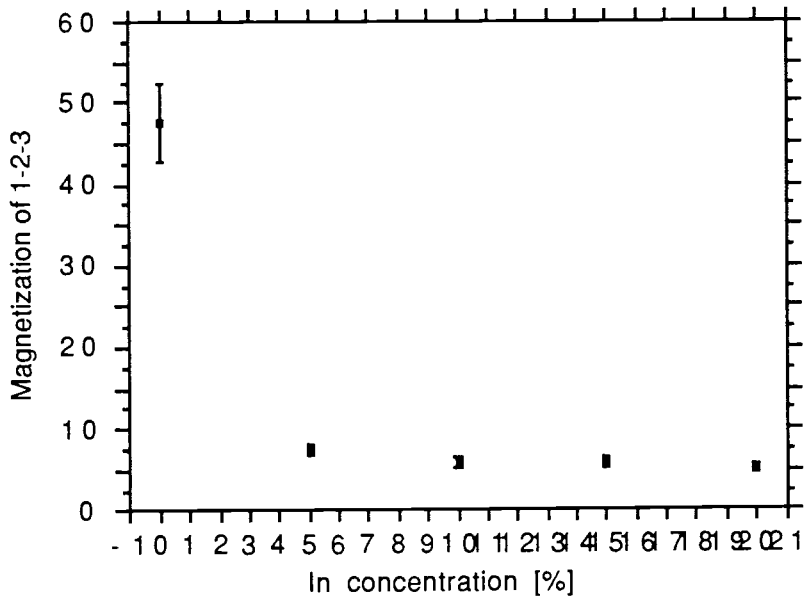

Fig. 6.21 Expelled magnetic flux versus In concentration

The graph shows a decrease of the magnetic flux as a function of In concentration between the pure and the 5% Sample. The magnetic flux remains constant within error margins for higher In concentrations.

7. DISCUSSIONS AND CONCLUSIONS

7.1 X-RAY DIFFRACTION

The grounds for conclusions about the site of substitution and the solubility limit are based on quantitative evaluations of the diffraction data by integration over the peak intensities. All sample sets were used for analysis.

7.1.1 SOLUBILITY LIMIT

Since the amount of the secondary phases $BaCuO_2$, CuO, and Y_2BaCuO_5 are constant and small for all In concentrations within a sample set, all excess In precipitates out in the form of $InBa_2Cu_3O_x$. All conclusions about the solubility limit of In are based on evaluations of intensities of the 003 peak from the major phase spectrum and from the major peak at 30.6° of the $InBa_2Cu_3O_x$ spectrum.

The monotonic feature of the 003 intensity implies that In is soluble in the major phase of the sample. The three sets of measurements were consistent within experimental error and the data points from all these sets were used for the determination of the solubility limit. The number of data points below and above the solubility limit is sufficient to make an accurate evaluation of the solubility limit by interpolation.

The intensity data for the 003 peak indicate a solubility limit of 3.0% for In (see Fig. 7.1). The intensity of this peak does not exceed this limit for higher concentrations of In.

Fig. 7.2 shows the $InBa_2Cu_3O_X$ intensities. The saturation with In in this graph takes place for samples containing 2.95%. The estimated error for the solubility limit is ± 0.4 %.

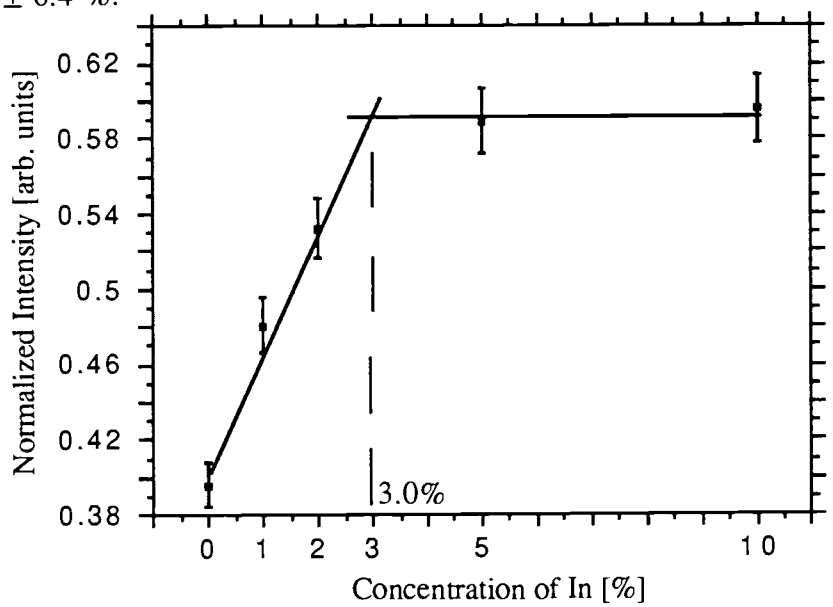

Fig. 7.1 Normalized Intensity of 003 vs. Indium concentration

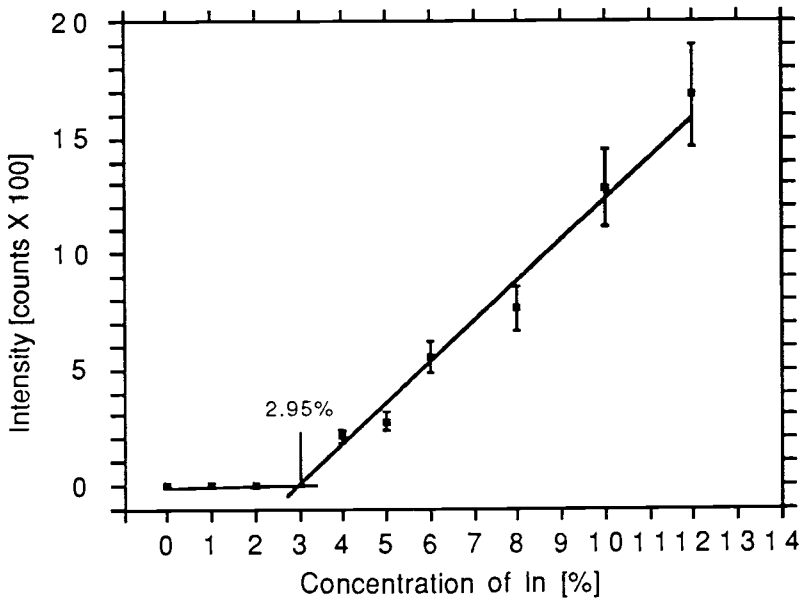

Fig. 7.2 Relative intensity of $InBa_2Cu_3O_X$ as a function of In concentration

7.1.2 SITE OF SUBSTITUTION

All samples were prepared under the assumption that In substitutes at the Y site of the unit cell because Y was removed for the added In. If no secondary phases had been detected for samples with concentrations of In below the solubility limit, it would have been proven that In substitutes at the Y site. A constant fraction of secondary phases which was detected in the sample and had an intensity near the detection limit, does not invalidate the above concept about the solution of the In.

The theoretically calculated intensities for Y substitution in the X-ray diffraction pattern for the 003 peak changes 0.9 % between samples containing 0% and 3% In. For other substitution sites, the intensity change is $\leq 3\%$ relative to Y. The experimental intensities change by 30% between the same In doping levels. The difference by a factor of 33 does not allow any quantitative comparisons between simulation and experiment . Therefore, no conclusions about the site of substitution for In can be drawn from the X-ray results.

In order to make those measurements, the sample is placed in a shallow depression of the aluminum sample holder and is pressed gently into this to obtain a smooth surface and uniplanarity with the surrounding aluminum of the sample holder. It is possible that the sample morphology of the In containing samples causes the c-axis of the unit cell to be oriented preferentially perpendicular to the surface of the sample holder. The alignment of the unit cells may be proportional to the In concentration. The orientation of unit cells within the bulk would not be distributed isotropically and reflections at Bragg planes perpendicular to the c-axis of the cell are preferred, i.e. the intensity of Bragg peaks with Miller indices 00X will increase in the X-ray diffraction pattern.

7.2 PAC SPECTROSCOPY

PAC measurements on the latest set of samples (#3) show one major site present in the sample corresponding to a unique substitution of In in the lattice of the superconductor. Only minor amounts of other sites can be detected for samples with 0%, 1%, and 2% In. PAC spectra at 5% In show a secondary site in a fraction of 25% with frequencies $\omega_1 = 82$ and $\omega_2 = 122$ Mrad/sec. This pattern probably corresponds to a site in $InBa_2Cu_3O_X$. Therefore, the solubility of 3%, established by X-ray work, is supported.

The asymmetry parameter η, which is a measure of the symmetry of the EFG distribution, was calculated by Plank et al.[49] and Kamal et al.[50] for different sites using a point charge model. In Plank's calculation, the parameter has a value of 0.24 for the Y site substitution, 0.48 for Barium, 0.32 for Cu(1), and 0.13 for the Cu(2) site substitution. The measured value is 0.26 for the major site and suggests a substitution at the Y site because of consistency with calculations.

7.3 MAGNETIC FLUX EXCLUSION

The critical temperature of the pure $YBa_2Cu_3O_{7-x}$ sample was measured by flux exclusion experiments and is $T_c = 92.7$ K. This value is equal to the literature value and indicates together with the strong flux exclusion and the sharp onset of flux exclusion a very high sample quality. The critical temperature for the sample containing 5% In is $T_c = 91.3$ K. The value for T_c remains constant within the error of the measurement for samples with 10%, 15% and 20% In. The magnetic flux penetrating the sample also decreases significantly between the pure sample and the sample containing 5% In. The

two latter results correspond with the hypothesis of a solubility limit at 3.0%. The critical temperature decreases probably with the grain size of the powder.

The relative change in critical temperature has a value of 1.5%. This small change in T_c indicates again a substitution of In at the Y site rather than at other sites. A substitution at the Cu(1) or Cu(2) site would be expected to cause a much larger change in T_c, because the Cu sites are involved in the conduction of the supercurrent .

7.4 CONCLUSIONS

The solubility limt of In in $YBa_2Cu_3O_{7-x}$ was established to be (3.0 ± 0.4) at% relative to Y. This task was performed by quantitative investigation of the integrated intensities of the 003 peak of the $YBa_2Cu_3O_{7-x}$ and the strongest peak of $InBa_2Cu_3O_x$ in the X-ray spectrograph. These patterns are a superposition of those two phases and a constant amount of minor, unimportant, other secondary phases.

Several approaches were undertaken to determine the substitution site of In in the lattice of the superconductor. The following arguments indicate a substitution of the In at the Y site:

- the amount of $BaCuO_2$, CuO, and Y_2BaCuO_5 is constant for samples with respect to In concentration within one sample set and therefore In must substitute in the major phase
- the only minor change (1.5%) of the critical temperature in the magnetic flux exclusion measurements
- only minor amounts of secondary substitution sites of In in the PAC measurements.

Bibliography

1. Anil Khurana in Physics Today, April 1987, p. 18
2. J.G. Bednorz and K.A. Müller, Z. Phys. B **64**, 189 (1986)
3. C.W. Chu et al., "Evidence for Superconductivity above 40K in the La-Ba-Cu-O compound system", Phys. Rev. Lett. **58**, 405 (1987)
4. M.K. Wu et al., "Superconductivity at 93K in a new mixed phase Y-Ba-Cu-O compound system at ambient temperatures", Phys. Rev. Lett. **58**, 908 (1987)
5. J.M. Tarascon et al., B **35**, 5347 (1987)
6. S.R. Ovshinski et al., "Superconductivity at 155K", L **58**, 2579 (1987)
7. Institut für Festkörperforschung, in Vorlesungsmanuskripte des 19. IFF Ferienkurses: Supraleitung und verwandte Quantenphänomene, Aachen, 1988
8. H. Rietschel, Phys. Blätter **43**, 357 (1987)
9. J.D. Jorgensen, Jpn. J. Phys. **26** Sup. 26-3, 2017 (1987)
10. R.M. Flemming et al., Phys. Rev. B **35**, 7191 (1987)
11. D.C. Johnston et al., Phys. Rev. B **36**, 4007 (1987)
12. T. Kajitain et al., Jpn. J. Appl. Phys. **26**, L1144 (1987)
13. A. Renault et al., J. de Phys. **48**, 1407 (1987)
14. J.D. Jorgensen et al., Phys. Rev B **36**, 3608 (1987)
15. A. Santoro et al., Mat. Res. Bull. **22**, 1007 (1987)
16. P. Bordet et al., Nature **327**, 687 (1987)
17. C.C. Torardi et al., Solid State Commun. **64**, 497 (1987)
18. H. Ehrenreich and D. Turnbull: Solid State Physics, Academic press, San Diego 1989
19. I.K. Schuller et al., Solid State Commun. **63**, 385 (1987)
20. R.M. Hazen et al., Phys. Rev. B **35**, 7238, (1987)
21. J.A. Gardner et al., Phys. Rev. B **38**, 11317 (1988)

22. G. Roth, and G. Heger, KfK Nachrichten (1987)

23. G. Van Tendeloo et al., Solid State Commun. **63**, 389 (1987)

24. Y. Syono et al., Jpn. J. Appl. Phys. **26**, L498 (1987)

25. R. Beyers et al., Appl. Phys. Lett. **50**, 1918 (1987)

26. E.D. Specht et al., Phys. Rev. B **37**, 7426 (1988)

27. P. Singh et al., Phys. Rev. B **39**, 2308 (1989)

28. P.H. Hor et al., Phys. Rev. Lett. **58**, 1891 (1987)

29. E.E. Alp et al., Phys. Rev. B **36**, 8910 (1987)

30. G. Wortmann et al., Solid State Commun. **65**, 1057 (1987)

31. R.J. Cava et al., Phys. Rev. Lett. **58**, 1676 (1987)

32. M.K. Wu et al., Phys. Rev. Lett. **58**, 908 (1987)

33. C. Kittel: Introduction to Solid State Physics, Wiley Interscience, New York, 1953

34. N.W. Ashcroft, N.D. Mermin: Solid State Physics, Saunders College, Philadelphia, 1976

35. C. Cohen-Tannoudji, B. Diu, F. Laloë: Quantum Mechanics, Wiley Interscience, New York, 1977

36. H. Jaeger, Ph.D. Thesis, Oregon State University (1987), unpublished.

37. H.S. Su, Ph.D. Thesis, Oregon State University (1989), unpublished.

38. U. Bäverstam et al., Nucl. Phys. A **186**, 500 (1972)

39. A.G. Biblioni et al., Phys. Rev. B **32**, 2392

40. C.G. Frase et al., J. Am. Ceram. Soc. **70**, C-204-C-205 (1987)

41. NBS Certificate: Standard Reference Material 640b, Silicon Powder $2\theta/d$ spacing Standard for X-ray diffraction (1987)

42. W. Wong-Ng et al., NBS, Standard X-ray diffraction powder patterns of Sixteen Ceramic phases (1987)

43. Handbook of Chemistry and Physics, Weast 68th edition, 1987-1988, CRC Press

44. A. William et al., Phys. Rev. B **37**, 7960 (1988)

45. Powder Diffraction File cards # 38-1433 and 38-1433a ($Ba_2Cu_3YO_7$) , International Center for Diffraction Data, Swarthmore (1988)

46. Powder Diffraction File cards # 38-1402 and 38-1402a ($BaCuO_2$), International Center for Diffraction Data, Swarthmore (1988)

47. Powder Diffraction File card# 5-0661 (CuO), International Center for Diffraction Data, Swarthmore (1953)

48. Powder Diffraction File cards # 38-1434 and 38-1434a ($BaCuY_2O_5$), International Center for Diffraction Data, Swarthmore (1988)

49. H. Plank et al., Phys. Lett. A **133**, 451 (1988)

50. R. Kamal et al., Phys. Rev. B **37**, 5928 (1988)